

eman ta zabal zazu



Universidad
del País Vasco

Euskal Herriko
Unibertsitatea

Shortcuts to adiabaticity and heat transport in trapped ions

Miguel Ángel Simón Martínez

Supervisors:

Prof. Juan Gonzalo Muga Francisco

Prof. Maria Luisa Pons Barba

Departamento de Química-Física

Facultad de Ciencia y Tecnología

Universidad del País Vasco/Euskal Herriko Unibertsitatea
(UPV/EHU)

Leioa, Febrero 2021

“Insert deep/meaningful/clever quote by someone who you admire or hate”

Someone who you admire or hate

Acknowledgements

Do not forget about the people that has been by your side and supported you.

*Esta Tesis ha sido financiada a través de una beca predoctoral concedida por el
Gobierno Vasco/Eusko Jaurlaritza*

Contents

Acknowledgements	v
List of Figures	ix
List of publications	xv
Introduction	1
1 Asymmetric scattering with NH Potential	3
1.1 Introduction	4
1.2 Generalized symmetries	6
1.3 Designing potentials for asymmetric devices	10
1.4 Extending the scattering asymmetry to a broad incident-momentum domain	13
1.5 Discussion	14
2 Local rectification of heat flux	17
2.1 Introduction	18
2.2 Homogeneous one-dimensional chain	19
2.3 Impurity-based thermal rectifier	23
2.4 Discussion	24
3 Chain of Ions	29
3.1 Introduction	30
3.2 Physical System	32
3.3 Calculation of the stationary heat currents	34
3.3.1 Algebraic, small-oscillations approach to calculate the steady state	36
3.4 Numerical Results	38
3.4.1 Evolution to steady state	39
3.4.2 Rectification in frequency graded chains	40
3.4.3 Same bath temperatures, different bath couplings	41
3.4.4 Dependence with ion number	41
3.4.5 Graded versus segmented	42
3.5 Summary and discussion	42

4	Rectification in a toy model	51
4.1	Introduction	52
4.2	Physical Model	53
4.3	Covariance matrix in the steady state	55
4.4	Solutions	57
4.5	Relation of the Model to a trapped ion set-up	59
4.5.1	Collective trap	59
4.5.2	Individual on-site traps	60
4.5.3	Optical molasses and Langevin baths	61
4.6	Looking for rectification	62
4.6.1	Parametric exploration	64
4.6.2	Spectral match/mismatch approach to rectification	66
4.7	Conclusions	69
4.8	acknowledgements	70
.1	Full set of steady-state equations for the components of $\mathbb{C}^{s.s}$	71
.2	Complete expressions for the Spectral Density Matrix	71
	Conclusions	73
	A Interaction versus asymmetry for adiabatic following	77
	Bibliography	79

List of Figures

- 1.1 (Color online) Devices with asymmetric scattering (limited to scattering coefficients being 0 or 1). The dashed and continuous lines represent respectively zero or one for the moduli of the scattering amplitudes; the bended lines are for reflection amplitudes, and the straight lines for transmission: (a) One-way mirror (\mathcal{TR}/\mathcal{A}); (b) One-way barrier (\mathcal{T}/\mathcal{R}); (c) One-Way T-filter (\mathcal{T}/\mathcal{A}); (d) Mirror & 1-way transmitter (\mathcal{TR}/\mathcal{R}); (e) One-way R-filter (\mathcal{R}/\mathcal{A}); (f) Transparent, one-way reflector (\mathcal{TR}/\mathcal{T}). The letter codes summarize the effect of left and right incidence, separated by a slash “/”. \mathcal{T} or \mathcal{R} on one side of the slash indicate a unit transmission or reflection coefficient for incidence from that side, whereas the absence of one or the other letter corresponds to zero coefficients. An \mathcal{A} denotes “full absorption”, i.e., both moduli of reflection and transmission amplitudes are zero for incidence from one side. For example, \mathcal{TR}/\mathcal{A} means unit modulus transmission and reflection from the left and total absorption from the right. 5
- 1.2 (Color online) One-way T-filter (\mathcal{T}/\mathcal{A} , $|T^l| = 1, T^r = R^l = R^r = 0$) with potential $V(x, y) = |V(x, y)|e^{i\phi(x, y)}$ set for $k_0 = 1/d$. (a) Absolute value $|V(x, y)|$; (b) Argument $\phi(x, y)$; (c) Transmission and reflection coefficients: $|R^l|^2$ (black, solid line), $|T^l|^2$ (green, solid line), $|R^r|^2$ (blue, tick, dashed line), $|T^r|^2$ (red, dotted line). $V_0 = \hbar^2/(2md^3)$ 11
- 1.3 (Color online) Transparent 1-way reflector with a local PT potential: (a) Approximation of the potential (1.8), real part (green solid line), imaginary part (blue dashed line). (b,c) Transmission and reflection coefficients versus momentum kd ; left incidence: $|R^l|^2$ (black, solid line), $|T^l|^2$ (green, solid line); right incidence: $|R^r|^2$ (blue, tick, dashed line), $|T^r|^2$ (red, dotted line, coincides with green, solid line). $\epsilon/d = 10^{-4}$. (b) $\alpha = 1.0\hbar^2/(4\pi m)$ (c) $\alpha = 1.225\hbar^2/(4\pi m)$ (the black, solid line coincides here mostly with the red, dotted and green, solid lines). 12

- 2.1 (Color online) (a) On-site potentials: harmonic potential centered at the equilibrium position of each atom (dashed blue line) as a function of the displacement from this position $x_i = y_i - y_{i0}$ in a -units, and the on-site potential for the impurity, $i = N/2 + 1$ (N even, red solid line). (b) Interaction potentials as a function of the distance between nearest neighbors: Morse potential (blue dashed line) valid for all atoms except for $i = N/2 + 1$, N even, where the modified potential (red solid line) is used. The harmonic approximation of the Morse potential is also depicted (eq. (2.5), black dots, only used for fig. 5, below). Parameters: $D = 0.5$, $g = 1$, $\gamma = 45$, $d = 100$ and $b = 105$, used throughout the paper. 21
- 2.2 (Color online) Symmetric temperature profiles for a homogeneous chain, without impurity. For $T_h = T_L$, $T_c = T_R$ (red solid dots) the (absolute value of) the heat flux is $J_{L \rightarrow R}$, equal to $J_{R \rightarrow L}$ for the reverse configuration of the bath temperatures, $T_h = T_R$, $T_c = T_L$ (black empty squares). Parameters as in fig. 1. 21
- 2.3 (Color online) Temperature profile along the homogeneous chain for different number of atoms: 100 (dotted black line), 125 (dashed blue line) and 150 (solid red line). The atom sites have been rescaled with the total number of atoms. The time averages have been carried over a time interval of $\approx 2 \times 10^6$ after a transient of $\approx 1 \times 10^5$. In the inset (a), the product JN vs. N demonstrates that for long chains JN is independent of N . In (b) the linear dependence of J with ΔT for a fixed number of atoms, $N = 100$, is shown. Parameters as in fig. 1. 23
- 2.4 (Color online) Temperature profile for the chain of $N = 20$ atoms, with an impurity in the $N/2 + 1$ position, with $T_L = T_h$ and $T_R = T_c$ (circles) and with the thermostat baths switched (squares). Parameters as in fig. 1. (a) $T_c = 0.15$, $T_h = 0.2$. $J_{L \rightarrow R} = 0.00769$ vs $J_{R \rightarrow L} = 0.00581$, with gives a rectification $R = 31\%$; (b) $T_c = 0.025$, $T_h = 0.325$. $J_{L \rightarrow R} = 0.0499$ vs $J_{R \rightarrow L} = 0.0140$, with $R = 256\%$ 25
- 2.5 (Color online) Rectification factor R as a function of the temperature difference between ends of the chain of atoms, ΔT . We have changed both T_h and T_c according to $T_c = 0.15 - (\Delta T - 0.05)/2$ and $T_h = 0.2 + (\Delta T - 0.05)/2$, with $N = 20$, keeping the rest of parameters as in fig. 2.1. Interatomic potentials: Morse potential, eq. (2.4) (black line with circles, see the temperature profiles of extreme points in fig. 4); harmonic potential, eq. (2.5) (red line with squares). 25
- 2.6 (Color online) Temperature profile for a harmonic interacting chain of $N = 20$ atoms, with an impurity in the $N/2 + 1$ position, with $T_L = T_h$ and $T_R = T_c$ (circles) and with the thermostat baths switched (squares), for (a) $\Delta T = 0.05$ and (b) $\Delta T = 0.3$. The corresponding rectification factors are (a) $R = 18\%$ and (b) $R = 85\%$. Parameters regarding the impurity are the same as in fig. 1. 27

- 3.1 Schematic representation of the frequency-graded chain of trapped ions proposed as a thermal rectifier. The left and right ends of the chain are in contact with optical molasses at temperatures T_L and T_R (green and grey boxes respectively). Each ion is in an individual trap. The (angular) frequencies of the traps increase homogeneously from left to right, starting from ω_1 and ending at $\omega_1 + \Delta\omega$. The ions interact through the Coulomb force, which is long range, and therefore all the ions interact among them, even distant neighbors. By default we use 15 ions. 30
- 3.2 (a) Temperatures of the ions in the stationary state for a graded chain with the parameters described in section 3.4.1. The temperature profiles found with the algebraic method (Eq. (3.17)) are indistinguishable from the ones found solving the Langevin equation (Eq. (3.3)). Empty triangles (squares) correspond to $T_L = T_H$ ($T_L = T_C$) and $T_R = T_C$ ($T_R = T_H$). (b) Heat currents as a function of time for $T_L = T_H$ and $T_R = T_C$, see Eq. (3.9): $J_L(t)$ (solid green line) from the left reservoir into the chain; $J_R(t)$ (dotted grey line) from the right reservoir into the chain (negative except at very short times); $J_L(t) + J_R(t)$ (dotted-dashed black line), which must go to zero in the steady state. The three lines tend to stationary values marked by horizontal lines. Parameters: $\omega_1 = 2\pi \times 50$ kHz, $a = 50 \mu\text{m}$, $\delta_H = -0.02 \Gamma$, and $\delta_C = -0.1 \Gamma$, which gives temperatures $T_H \approx 12$ mK and $T_C \approx 3$ mK. $\Delta\omega = 0.5\omega_1$. In all figures $\Gamma = 2\pi \times 41.3$ MHz. 44
- 3.3 Graded chain of $N = 15$ $^{24}\text{Mg}^+$ ions. (a) Stationary fluxes for different frequency increments: J_{\rightarrow} (for $T_L = T_H$ and $T_R = T_C$, dashed line); J_{\leftarrow} (for $T_L = T_C$ and $T_R = T_H$, solid line) (b) Rectification factor. Parameters: $\omega_1 = 2\pi \times 1$ MHz, $l = 5.25 \mu\text{m}$, $a = 4.76l$ ($25 \mu\text{m}$), $\delta_H = -0.02 \Gamma$, and $\delta_C = -0.1 \Gamma$ 45
- 3.4 Rectification factor in a graded chain of $N = 15$ $^{24}\text{Mg}^+$ ions for different trap distances and frequency increment. The dashed lines are for $R = 0$ and delimit the regions $J_{\rightarrow} > J_{\leftarrow}$ and $J_{\rightarrow} < J_{\leftarrow}$. The parameters are $\omega_1 = 2\pi \times 1$ MHz, $l = 5.25 \mu\text{m}$, $\delta_H = -0.02 \Gamma$, and $\delta_C = -0.1 \Gamma$ 46
- 3.5 (a) Friction coefficient defined in Eq. (3.4). (b) Bath temperature defined in Eq. (3.5). (c) Rectification as a function of the temperature difference between the hot and cold baths $T_H - T_C$ for δ_H below (dashed black line) and above (solid blue line) the Doppler limit, and $\delta_C = \delta_D$ (Doppler limit). Parameters: $\omega_1 = 2\pi \times 1$ MHz, $\Delta\omega = 0.15\omega_1$, $l = 5.25 \mu\text{m}$, $a = 4.76l$ 47
- 3.6 Rectification factor for different bath temperature differences ΔT as the number of ions is increased. The detuning of the cold bath laser is set to the Doppler limit $\delta_C = -\Gamma/2$. $\omega_1 = 2\pi \times 1$ MHz, $\Delta\omega = 0.15\omega_1$, $l = 5.25 \mu\text{m}$, $a = 4.76l$ 48

3.7	Comparison of graded and segmented chains with $N = 15$ $^{24}\text{Mg}^+$ ions. (a) Maximum of J_{\rightarrow} and J_{\leftarrow} for the graded and segmented chain for different frequency increments. (b) Rectification factor: graded chain (dashed lines); segmented chain (solid lines). Parameters: $\omega_1 = 2\pi \times 1$ MHz, $l = 5.25 \mu\text{m}$, $a = 4.76 l$, $\delta_H = -0.02 \Gamma$, and $\delta_C = -0.1 \Gamma$	49
3.8	Thermal conductivity through the chain for $T_L > T_R$ (empty squares), and $T_L < T_R$ (filled triangles). $\omega_1 = 2\pi \times 1$ MHz, $\Delta\omega = 0.15 \omega_1$, $l = 5.25 \mu\text{m}$, $a = 4.76 l$, $\delta_H = -0.02 \Gamma$ and $\delta_C = -0.1 \Gamma$	50
4.1	Diagram of the model described in Section 4.2. Two ions coupled to each other through a spring constant k . Each ion is harmonically trapped and connected to a bath characterized by its temperature T_i and its friction coefficient γ_i	53
4.2	Rectification, R , in the $k_L k_R$ plane for $k = 1.17 \times \text{fN/m}$, $\gamma_L = 6.75 \times 10^{-22}$ kg/s, and $\gamma_R = 4.64 \gamma_L$	63
4.3	Rectification factor, R , given by Eq. (4.32).	66
4.4	Rectification for different values of $c = m_2/m_1 = \gamma_R/\gamma_L$ when the maximum condition in the $k_L k_R$ plane is satisfied (Eq. (4.31)). . . .	67
4.5	Spectral densities of the velocities of the ions (r_3 and r_4) corresponding to different values of c in Fig. 4.4: (a), (b) for $c = 1$ and (c), (d) for $c = 10$. Solid, black lines correspond to the left ion velocity spectral density $\mathbb{S}_{3,3}(\omega)$ and dashed, blue lines correspond to the right ion velocity spectral density $\mathbb{S}_{4,4}(\omega)$. (a) and (b) correspond to $R = 0$: the overlap between the phonon bands is the same in the forward and reversed configurations. (c) and (d) correspond to $R \approx 0.8$: in the forward configuration (c) the phonons match better than in the reversed configuration (d).	68

dedicatory here

List of publications

I) The results of this Thesis are based on the following articles

Published Articles

1. M. Pons, Y. Y. Cui, A. Ruschhaupt, **M. A. Simón** and J. G. Muga
Local rectification of heat flux
[EPL **119**, 64001 \(2017\).](#)
2. A. Ruschhaupt, T. Dowdall, **M. A. Simón** and J. G. Muga
Asymmetric scattering by non-Hermitian potentials
[EPL **120**, 20001 \(2017\).](#)
3. **M. A. Simón**, A. Buendía and J. G. Muga
Symmetries and Invariants for Non-Hermitian Hamiltonians
[Mathematics **6**, 111 \(2018\).](#)
4. **M. A. Simón**, A. Buendía, A. Kiely, A. Mostafazadeh and J. G. Muga
S-matrix pole symmetries for non-Hermitian scattering Hamiltonians
[Phys. Rev. A **99**, 052110 \(2019\).](#)
5. **M. A. Simón**, S. Martínez-Garaot, M. Pons and J. G. Muga
Asymmetric heat transport in ion crystals
[Phys. Rev. E **100**, 032109 \(2019\).](#)
6. A. Alaña, S. Martínez-Garaot, **M. A. Simón** and J. G. Muga
Symmetries of $(N \times N)$ non-Hermitian Hamiltonian matrices
[J. Phys. A: Math. Theor. **53**, 135304 \(2020\).](#)

Preprints

1. A. Ruschhaupt, A. Kiely, **M. A. Simón** and J. G. Muga
Quantum-optical implementation of non-Hermitian potentials for asymmetric scattering
[arXiv:2008.01702 \[quant-ph\]](#) (2020)
(Accepted for publication in Phys. Rev. A)
2. **M. A. Simón**, A. Alaña, M. Pons, A. Ruiz-García and J. G. Muga
Heat rectification with a minimal model of two harmonic oscillators
[arXiv:2010.10432 \[cond-mat.stat-mech\]](#) (2020)

II) Other articles produced during the Thesis period

Published Articles not included in this Thesis

1. M. Palmero, **M. A. Simón** and D. Poletti
Towards Generation of Cat States in Trapped Ions Set-Ups via FAQUAD Protocols and Dynamical Decoupling
[Entropy](#) **21**, 1207 (2019)
2. **M. A. Simón**, M. Palmero, S. Martínez-Garaot and J. G. Muga
Trapped-ion Fock-state preparation by potential deformation
[Phys. Rev. Research](#) **2**, 023372 (2020)

Introduction

Todo fuego que se precie empieza con una pequeña chispa.

Chapter 1

Asymmetric scattering with NH Potential

The scattering of quantum particles by non-hermitian (generally nonlocal) potentials in one dimension may result in asymmetric transmission and/or reflection from left and right incidence. After extending the concept of symmetry for non-hermitian potentials, eight generalized symmetries based on the discrete Klein's four-group (formed by parity, time reversal, their product, and unity) are found. Together with generalized unitarity relations they determine selection rules for the possible and/or forbidden scattering asymmetries. Six basic device types are identified when the scattering coefficients (squared moduli of scattering amplitudes) adopt zero/one values, and transmission and/or reflection are asymmetric. They can pictorially be described as a one-way mirror, a one-way barrier (a Maxwell pressure demon), one-way (transmission or reflection) filters, a mirror with unidirectional transmission, and a transparent, one-way reflector. We design potentials for these devices and also demonstrate that the behavior of the scattering coefficients can be extended to a broad range of incident momenta.

1.1 Introduction

The current interest to develop new quantum technologies is boosting applied and fundamental research on quantum phenomena and on systems with potential applications in logic circuits, metrology, communications or sensors. Robust basic devices performing elementary operations are needed to perform complex tasks when combined in a circuit.

In this paper we investigate the properties of potentials with asymmetric transmission or reflection for a quantum, spinless particle of mass m satisfying a one-dimensional (1D) Schrödinger equation. If we restrict the analysis to transmission and reflection coefficients (squared moduli of the scattering complex amplitudes) being either zero or one, a useful simplification for quantum logic operations, there are six types of asymmetric devices, see fig. 1.1. These devices cannot be constructed with Hermitian potentials. In fact for all device types with transmission asymmetries, which are four of the six possible devices, the potentials have to be also nonlocal. Therefore, nonlocal potentials play a major role in this paper. They appear naturally when applying partitioning techniques under similar conditions to the ones leading to non-hermitian potentials, namely, as effective interactions for a subsystem or component of the full wave-function, even if the interactions for the large system are hermitian and local [1].

Symmetries can be used, similarly to their standard application in atomic physics to determine selection rules for allowed/forbidden transitions, to predict whether a certain potential may or may not lead to asymmetric scattering. The concept of symmetry, however, must be generalized when dealing with non-hermitian potentials.

The theory in this paper is worked out for particles and the Schrödinger equation but it is clearly of relevance for optical devices due to the much exploited analogies and connections between Maxwell's equations and the Schrödinger equation, which were used, e.g., to propose the realization of PT-symmetric potentials in optics [2].

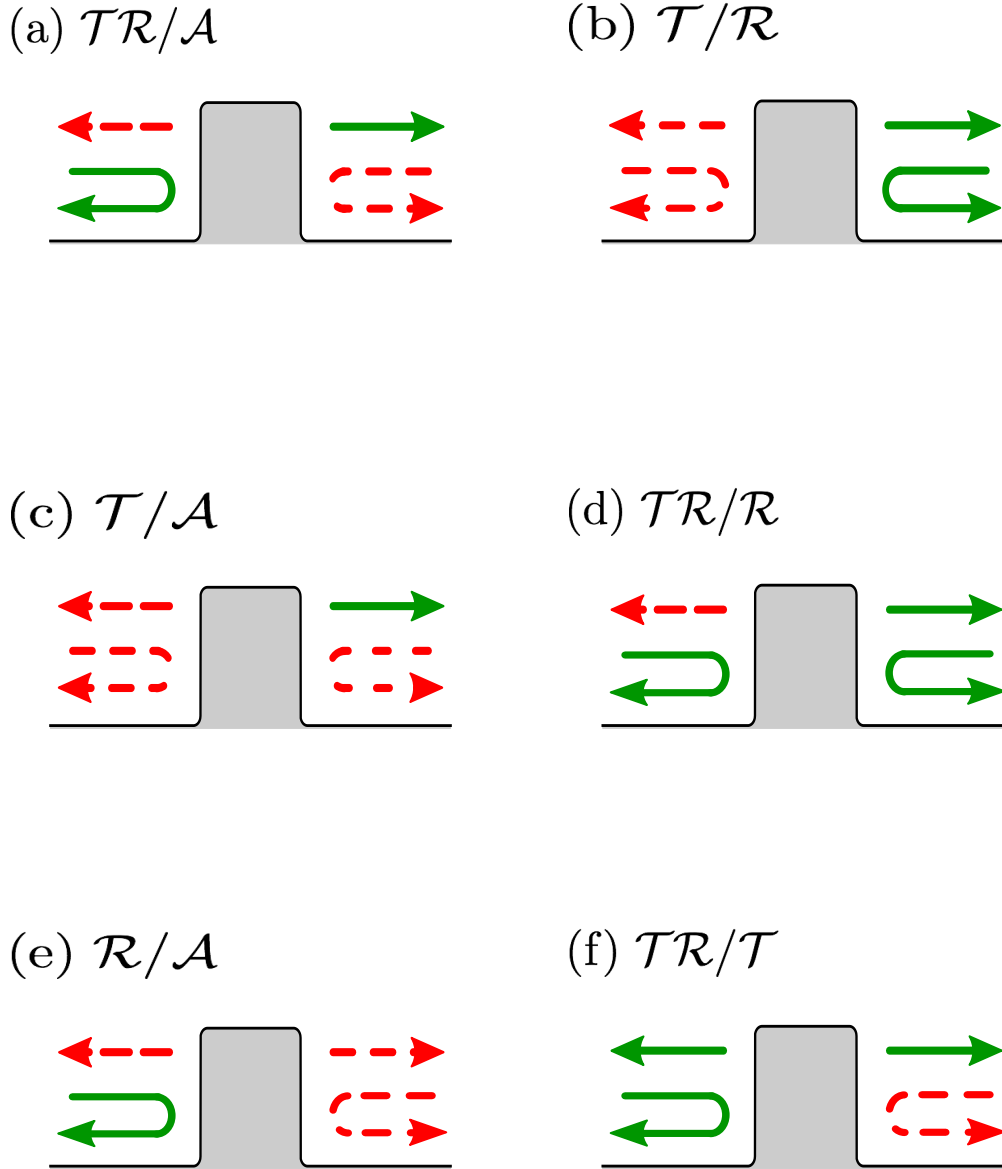


FIGURE 1.1: (Color online) Devices with asymmetric scattering (limited to scattering coefficients being 0 or 1). The dashed and continuous lines represent respectively zero or one for the moduli of the scattering amplitudes; the bended lines are for reflection amplitudes, and the straight lines for transmission: (a) One-way mirror (\mathcal{TR}/\mathcal{A}); (b) One-way barrier (\mathcal{T}/\mathcal{R}); (c) One-Way T-filter (\mathcal{T}/\mathcal{A}); (d) Mirror & 1-way transmitter (\mathcal{TR}/\mathcal{R}); (e) One-way R-filter (\mathcal{R}/\mathcal{A}); (f) Transparent, one-way reflector (\mathcal{TR}/\mathcal{T}). The letter codes summarize the effect of left and right incidence, separated by a slash “/”. \mathcal{T} or \mathcal{R} on one side of the slash indicate a unit transmission or reflection coefficient for incidence from that side, whereas the absence of one or the other letter corresponds to zero coefficients. An \mathcal{A} denotes “full absorption”, i.e., both moduli of reflection and transmission amplitudes are zero for incidence from one side. For example, \mathcal{TR}/\mathcal{A} means unit modulus transmission and reflection from the left and total absorption from the right.

TABLE 1.1: Symmetries of the potential classified in terms of the commutativity or pseudo-hermiticity of H with the elements of Klein's 4-group $\{1, \Pi, \theta, \Pi\theta\}$ (second column). The first column sets a simplifying roman-number code for each symmetry. The relations among potential matrix elements are given in coordinate and momentum representations in the third and fourth columns. The fifth column gives the relations they imply in the matrix elements of S and/or \hat{S} matrices (S is for scattering by H and \hat{S} for scattering by H^\dagger). From them the next four columns set the relations implied on scattering amplitudes. Together with generalized unitarity relations (1.3) they also imply relations for the moduli (tenth column), and phases (not shown). The last two columns indicate the possibility to achieve perfect asymmetric transmission or reflection: “ P ” means possible (but not necessary), “No” means impossible. In some cases “ P ” is accompanied by a condition that must be satisfied.

Code	Symmetry	$\langle x V y\rangle =$	$\langle p V p'\rangle =$	$\langle p S p'\rangle =$	$T^l =$	$T^r =$	$R^l =$	$R^r =$	from eq. (1.3)	$ T^l =1$ $ T^r =0$	
I	$1H = H1$	$\langle x V y\rangle$	$\langle p V p'\rangle$	$\langle p S p'\rangle$	T^l	T^r	R^l	R^r			P
II	$1H = H^\dagger 1$	$\langle y V x\rangle^*$	$\langle p' V p\rangle^*$	$\langle p \hat{S} p'\rangle$	\hat{T}^l	\hat{T}^r	\hat{R}^l	\hat{R}^r	$ T^l = T^r , R^l = R^r $	No	
III	$\Pi H = H\Pi$	$\langle -x V -y\rangle$	$\langle -p V -p'\rangle$	$\langle -p S -p'\rangle$	T^r	T^l	R^r	R^l	$ T^l = T^r , R^l = R^r $	No	
IV	$\Pi H = H^\dagger \Pi$	$\langle -y V -x\rangle^*$	$\langle -p' V -p\rangle^*$	$\langle -p \hat{S} -p'\rangle$	\hat{T}^r	\hat{T}^l	\hat{R}^r	\hat{R}^l		$P, R^r R^{l*} = 1$	P
V	$\Theta H = H\Theta$	$\langle x V y\rangle^*$	$\langle -p V -p'\rangle^*$	$\langle -p' \hat{S} -p\rangle$	\hat{T}^r	\hat{T}^l	\hat{R}^l	\hat{R}^r	$ R^l = R^r $	$P, R^{r,l} = 1$	
VI	$\Theta H = H^\dagger \Theta$	$\langle y V x\rangle$	$\langle -p' V -p\rangle$	$\langle -p' S -p\rangle$	T^r	T^l	R^l	R^r	$ T^l = T^r $	No	
VII	$\Theta \Pi H = H\Theta \Pi$	$\langle -x V -y\rangle^*$	$\langle p V p'\rangle^*$	$\langle p' \hat{S} p\rangle$	\hat{T}^l	\hat{T}^r	\hat{R}^r	\hat{R}^l	$ T^l = T^r $	No	P
VIII	$\Theta \Pi H = H^\dagger \Theta \Pi$	$\langle -y V -x\rangle$	$\langle p' V p\rangle$	$\langle p' S p\rangle$	T^l	T^r	R^r	R^l	$ R^l = R^r $	P	

1.2 Generalized symmetries

The detailed technical and formal background for the following can be found in a previous review on 1D scattering by complex potentials [1], a companion to this article for those readers willing to reproduce the calculations in detail. The Supplemental Material (Sec. I) provides also a minimal kit of scattering theory formulae that may be read first to set basic concepts and notation. The notation is essentially as in [1], but it proves convenient to use for the potential matrix (or kernel function) in coordinate representation two different forms, namely $\langle x|V|y\rangle = V(x, y)$. “Local” potentials are those for which $V(x, y) = V(x)\delta(x - y)$.

For hermitian Hamiltonians, symmetries are represented by the commutation of a symmetry operator with the Hamiltonian. In scattering theory, symmetry plays an important role as it implies relations among the S-matrix elements beyond those implied by its unitarity, see e.g. [3] and, for scattering in one dimension, Sec. 2.6 in [1].

Symmetries are also useful for non-hermitian Hamiltonians, but the mathematical and conceptual framework must be generalized. We consider that a unitary or antiunitary operator A represents a symmetry of H if it satisfies at least one of

these relations,

$$AH = HA, \quad (1.1)$$

$$AH = H^\dagger A. \quad (1.2)$$

For a right eigenstate of H , $|\psi\rangle$, with eigenvalue E , eq. (1.1) implies that $A|\psi\rangle$ is also a right eigenstate of H , with the same eigenvalue if A is unitary, and with the complex conjugate eigenvalue E^* if A is antiunitary. Equation (1.2) implies that $A|\psi\rangle$ is a right eigenstate of H^\dagger with eigenvalue E for A unitary or E^* for A antiunitary, or a left eigenstate of H with eigenvalue E^* for A unitary, or E for A antiunitary. For real-energy scattering eigenfunctions in the continuum, the ones we are interested in here, $E^* = E$. When eq. (1.2) holds we say that H is A -pseudohermitian [4]. Parity-pseudohermiticity has played an important role as being equivalent to space-time reflection (PT) symmetry for *local* potentials [4, 5]. A large set of these equivalences will be discussed below. A relation of the form (1.2) has been also used with differential operators to get real spectra beyond PT-symmetry for local potentials [6, 7].

Here we consider A to be a member of the Klein 4-group $K_4 = \{1, \Pi, \Theta, \Pi\Theta\}$ formed by unity, the parity operator Π , the antiunitary time-reversal operator Θ , and their product $\Pi\Theta$. This is a discrete, abelian group. We also assume that the Hamiltonian is of the form $H = H_0 + V$, with H_0 , the kinetic energy operator of the particle, being hermitian and satisfying $[H_0, A] = 0$ for all members of the group, whereas the potential V may be non-local in position representation. The motivation to use Klein's group is that the eight relations implied by eqs. (1.1) and (1.2) generate all possible symmetries of a non-local potential due to the identity, complex conjugation, transposition, and sign inversion, both in coordinate or momentum representation, see table 1.1, where each symmetry has been labeled by a roman number. Interesting enough, in this classification hermiticity (symmetry II in table 1.1) may be regarded as 1-pseudohermiticity.

Examples on how to find the relations in the fifth column of table 1.1 of S - and \hat{S} -matrix elements (for scattering by H and H^\dagger respectively) are provided in ref. [1], where the symmetry types III, VI, and VII were worked out. Similar manipulations, making use of the action of unitary or antiunitary operators of Klein's group on Möller operators, help to complete the table.

TABLE 1.2: Equivalences among symmetries for the potential elements. Given the symmetry of the upper row, the table provides the equivalent symmetries. For example, if II is satisfied, then III=IV holds. In words, if the potential is hermitian, parity symmetry amounts to parity pseudohermiticity. In terms of the matrix elements of the potential, if $\langle x|V|y\rangle = \langle y|V|x\rangle^*$ and also $\langle x|V|y\rangle = \langle -x|V|-y\rangle$, $\forall(x,y)$, then $\langle x|V|y\rangle = \langle -y|V|-x\rangle^*$ holds as well. One may proceed similarly for all other relations. The commutation with the identity (I) is excluded as this symmetry is satisfied by all potentials.

II	III	IV	V	VI	VII	VIII
III=IV	II=IV	II=III	II=VI	II=V	II=VIII	II=VII
V=VI	V=VII	V=VIII	III=VII	III=VIII	III=V	III=VI
VII=VIII	VI=VIII	VI=VII	IV=VIII	IV=VII	IV=VI	IV=V

From the fifth column in table 1, equivalences among the amplitudes for left and right incidence for scattering by H , $(T^{l,r}, R^{l,r})$ or H^\dagger $(\hat{T}^{l,r}, \hat{R}^{l,r})$, are deduced, see the Supplemental Material and the four columns for $T^{l,r}$, and $R^{l,r}$ in table 1.1. Together with the generalized unitarity relations $\hat{S}^\dagger S = S \hat{S}^\dagger = 1$, which in terms of amplitudes take the form [1]

$$\begin{aligned}
\hat{T}^l T^{l*} + \hat{R}^l R^{l*} &= 1, \\
\hat{T}^r T^{r*} + \hat{R}^r R^{r*} &= 1, \\
\hat{T}^{l*} R^r + T^r \hat{R}^{l*} &= 0, \\
T^l \hat{R}^{r*} + \hat{T}^{r*} R^l &= 0,
\end{aligned} \tag{1.3}$$

these equivalences between the amplitudes imply further consequences on the amplitudes' moduli (tenth column of table 1.1) and phases (not shown). The final two columns use the previous results to determine if perfect asymmetry is possible for transmission or reflection. This makes evident that hermiticity (II) and parity (III) preclude, independently, any asymmetry in the scattering coefficients; PT-symmetry (VII) or Θ -pseudohermiticity (VI) forbid transmission asymmetry (all local potentials satisfy automatically symmetry VI), whereas time-reversal symmetry (i.e., a real potential in coordinate space) (V) or PT-pseudohermiticity (VIII) forbid reflection asymmetry. A caveat is that asymmetric effects forbidden by a certain symmetry in the linear (Schrödinger) regime considered in this paper might not be forbidden in a non-linear regime [8], which goes beyond our present scope.

The occurrence of one particular symmetry in the potential (conventionally “first symmetry”) does not exclude a second symmetry to be satisfied as well.

TABLE 1.3: Device types for transmission and/or reflection asymmetry, restricted to 1 or 0 moduli for the scattering amplitudes. The fifth column indicates the symmetries in table 1.1 that forbid the device. Figures S2, S3, S5 and S6 can be found in the supplemental material to this paper.

Device type	Left incidence	Right incidence	Code	Forbidden by
One-way mirror	transmits and reflects	absorbs	\mathcal{TR}/\mathcal{A}	II, III, IV, V, VI, VII, VIII
One-way barrier	transmits	reflects	\mathcal{T}/\mathcal{R}	II, III, IV, V, VI, VII, VIII
One-way T-filter	transmits	absorbs	\mathcal{T}/\mathcal{A}	II, III, IV, V, VI, VII
Mirror&1-way transmitter	transmits and reflects	reflects	\mathcal{TR}/\mathcal{R}	II, III, VI, VII
One-way R-filter	reflects	absorbs	\mathcal{R}/\mathcal{A}	II, III, IV, V, VII, VIII
Transparent 1-way reflector	transmits and reflects	transmits	\mathcal{TR}/\mathcal{T}	II, III, V, VIII

TABLE 1.4: Device types allowed for a given symmetry.

Symmetry	Allowed devices
I	All types
II	None
III	None
IV	$\mathcal{TR}/\mathcal{R}, \mathcal{TR}/\mathcal{T}$
V	\mathcal{TR}/\mathcal{R}
VI	$\mathcal{R}/\mathcal{A}, \mathcal{TR}/\mathcal{T}$
VII	\mathcal{TR}/\mathcal{T}
VIII	$\mathcal{T}/\mathcal{A}, \mathcal{TR}/\mathcal{R}$

When a double symmetry holds, excluding the identity, the “first” symmetry implies the equivalence of the second symmetry with a third symmetry. We have already mentioned that II-pseudohermiticity (IV) is equivalent to PT -symmetry (VII) for local potentials. Being local is just one particular way to satisfy symmetry VI, namely Θ -pseudohermiticity. The reader may verify with the aid of the third column for $\langle x|V|y\rangle$ in table 1.1, that indeed, if symmetry VI is satisfied (first symmetry), symmetry IV has the same effect as symmetry VII. They become equivalent. Other well known example is that for a local potential (symmetry VI is satisfied), a real potential in coordinate space is necessarily hermitian, so symmetries V and II become equivalent. These examples are just particular cases of the full set of equivalences given in table 1.2.

Combining the information of the last two-columns in table 1.1 with the additional condition that all scattering coefficients be 0 or 1 we elaborate table 1.3, which provides the symmetries that do not allow the implementation of the devices in fig. 1.1. The complementary table 1.4 gives instead the symmetries that allow, but do not necessarily imply, a given device type. The device denominations in fig. 1.1 or table 1.3 are intended as short and meaningful, and do not necessarily coincide with some extended terminology, in part because the range of possibilities

is broader here than those customarily considered, and because we use a 1 or 0 condition for the moduli. For example, a device with reflection asymmetry and with $T^r = T^l = 1$ would in our case be a particular “transparent, one-way reflector”, as full transmission occurs from both sides. This effect has however become popularized as “unidirectional invisibility” [10, 11]. A debate on terminology is not our main concern here, and the use of a code system as the one proposed will be instrumental in avoiding misunderstandings.

1.3 Designing potentials for asymmetric devices

We will show how to design non-local potentials leading to the asymmetric devices. For simplicity we look for non-local potentials $V(x, y)$ with local support that vanish for $|x| > d$ and $|y| > d$.

Inverse scattering proceeds similarly to [12], by imposing an ansatz for the wavefunctions and the potential in the stationary Schrödinger equation

$$\frac{\hbar^2 k^2}{2m} \psi(x) = -\frac{\hbar^2}{2m} \frac{d^2}{dx^2} \psi(x) + \int_{-d}^d dy V(x, y) \psi(y). \quad (1.4)$$

The free parameters are fixed making use of the boundary conditions. The form of the wavefunction incident from the left is $\psi_l(x) = e^{ikx} + R^l e^{-ikx}$ for $x < -d$ and $\psi_l(x) = T^l e^{ikx}$ for $x > d$, where $k = p/\hbar$. The wavefunction incident from the right is instead $\psi_r(x) = e^{-ikx} T^r$ for $x < -d$ and $\psi_r(x) = e^{-ikx} + R^r e^{ikx}$ for $x > d$.

Our strategy is to assume polynomial forms for the two wavefunctions in the interval $|x| < d$, $\psi_l(x) = \sum_{j=0}^5 c_{l,j} x^j$ and $\psi_r(x) = \sum_{j=0}^5 c_{r,j} x^j$, and also a polynomial ansatz of finite degree for the potential $V(x, y) = \sum_i \sum_j v_{ij} x^i y^j$. Inserting these ansatzes in eq. (1.4) and from the conditions that $\psi_{l,r}$ and their derivatives must be continuous, all coefficients $c_{l,j}$, $c_{r,j}$ and v_{ij} can be determined. Symmetry properties of the potential can also be imposed via additional conditions on the potential coefficients v_{ij} . For example we may use this method to obtain a one-way T-filter (\mathcal{T}/\mathcal{A}) device (third device in table 1.3) with a nonlocal PT-pseudohermitian potential (symmetry VIII of table 1.1) for a chosen wavevector $k = k_0$. The absolute value and argument of the resulting potential $V(x, y)$ are shown in figs. 1.2(a) and 1.2(b) together with its scattering coefficients as function of the incident wave vector, fig. 1.2(c). As can be seen in fig. 1.2(c) the imposed

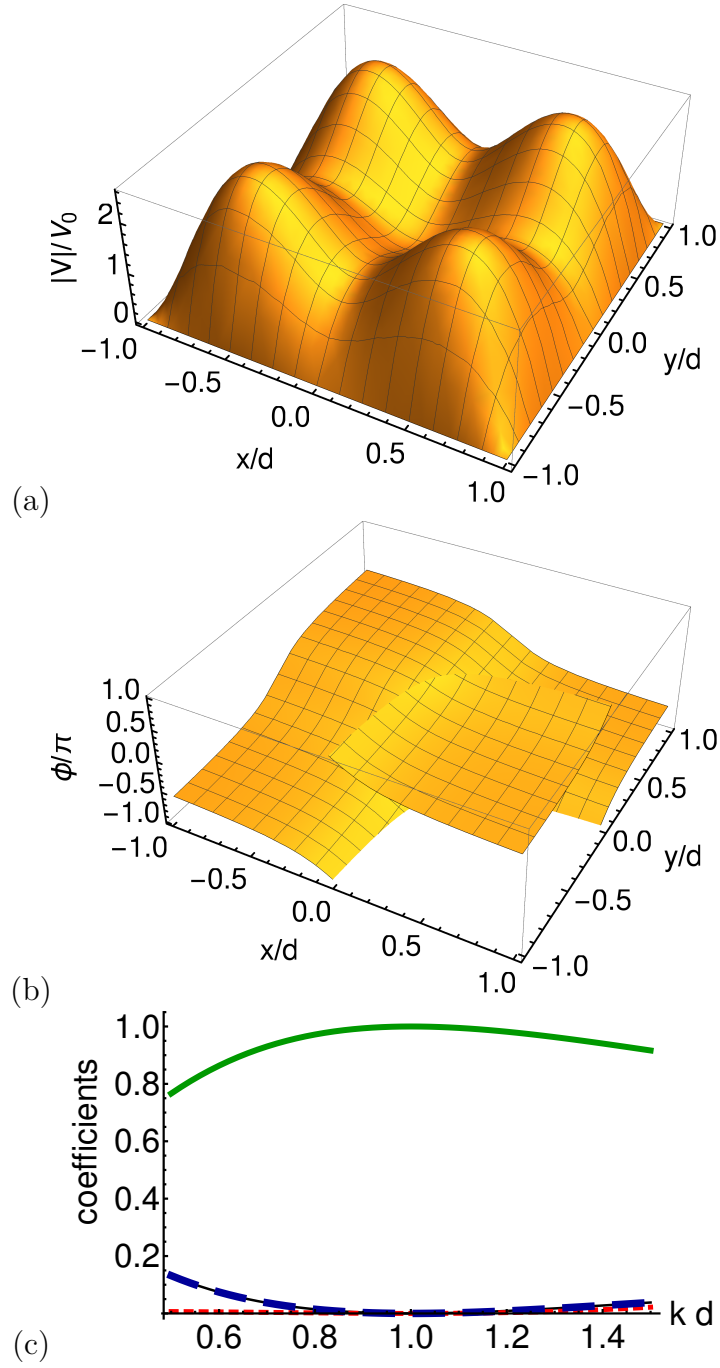


FIGURE 1.2: (Color online) One-way T-filter (\mathcal{T}/\mathcal{A} , $|T^l| = 1, T^r = R^l = R^r = 0$) with potential $V(x, y) = |V(x, y)|e^{i\phi(x, y)}$ set for $k_0 = 1/d$. (a) Absolute value $|V(x, y)|$; (b) Argument $\phi(x, y)$; (c) Transmission and reflection coefficients: $|R^l|^2$ (black, solid line), $|T^l|^2$ (green, solid line), $|R^r|^2$ (blue, tick, dashed line), $|T^r|^2$ (red, dotted line). $V_0 = \hbar^2/(2md^3)$.

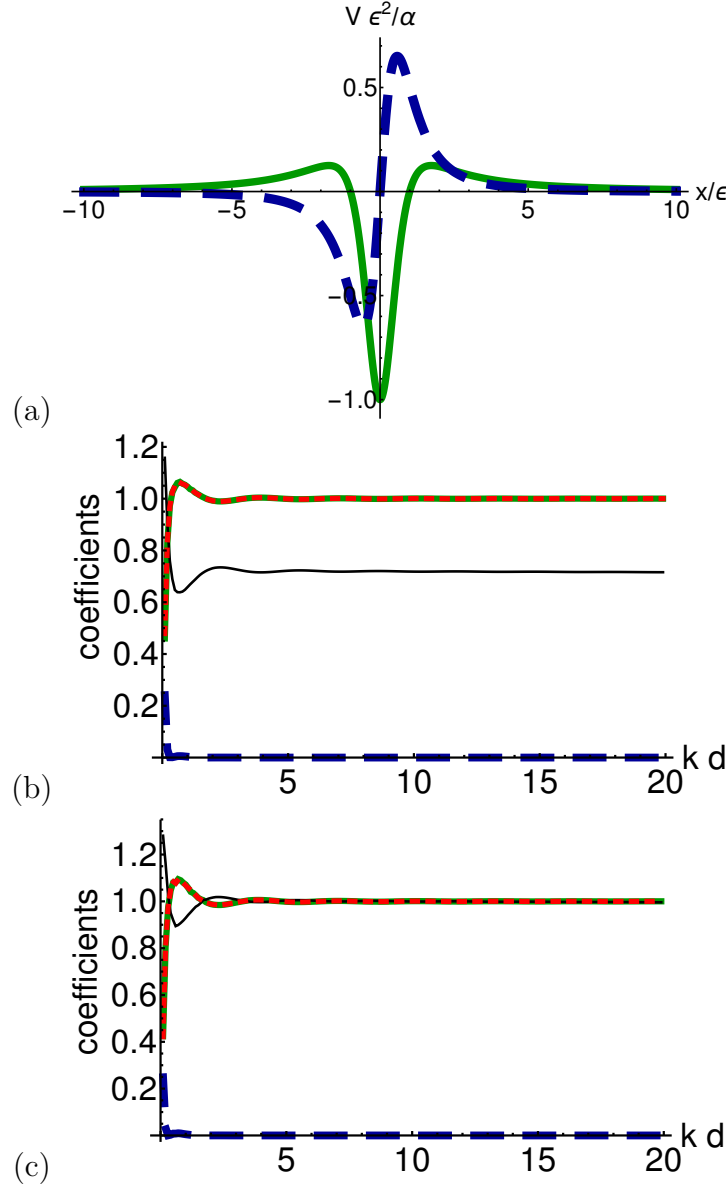


FIGURE 1.3: (Color online) Transparent 1-way reflector with a local PT potential: (a) Approximation of the potential (1.8), real part (green solid line), imaginary part (blue dashed line). (b,c) Transmission and reflection coefficients versus momentum kd ; left incidence: $|R^l|^2$ (black, solid line), $|T^l|^2$ (green, solid line); right incidence: $|R^r|^2$ (blue, tick, dashed line), $|T^r|^2$ (red, dotted line, coincides with green, solid line). $\epsilon/d = 10^{-4}$. (b) $\alpha = 1.0\hbar^2/(4\pi m)$ (c) $\alpha = 1.225\hbar^2/(4\pi m)$ (the black, solid line coincides here mostly with the red, dotted and green, solid lines).

scattering coefficients are fulfilled exactly for the chosen wavevector. They are also satisfied approximately in a neighborhood of k_0 . In the Supplemental Material, Sec. II, we give further details about the construction of this potential and we work out other asymmetric devices of fig. 1.1.

1.4 Extending the scattering asymmetry to a broad incident-momentum domain

The inversion technique just described may be generalized to extend the range of incident momenta for which the potential works by imposing additional conditions and increasing correspondingly the number of parameters in the wavefunction ansatz, for example we may impose that the derivatives of the amplitudes, in one or more orders, vanish at k_0 , or 0/1 values for the coefficients not only at k_0 but at a series of grid points k_1, k_2, \dots, k_N , as in [1, 12–14].

Here we put forward instead a method that provides a very broad working-window domain. While we make formally use of the Born approximation, the exact numerical computations demonstrate the robustness and accuracy of the approach to achieve that objective by making use of an adjustable parameter in the potential. The very special role of the Born approximation in inverse problems has been discussed and demonstrated in [15–17]. Specifically we study a transparent one-way reflector \mathcal{TR}/\mathcal{T} . Our aim is now to find a local PT-symmetric potential such that asymmetric reflection results, $T^l = T^r = 1, R^r = 0, |R^l| = 1$ for a broad range of incident momenta. A similar goal was pursued in [18] making use of a supersymmetric transformation, without imposing $|R^l| = 1$.

In the Born approximation and for a local potential $V(x)$, the reflection amplitudes take the simple form

$$R^l = -\frac{2\pi im}{p} \langle -p|V|p \rangle, \quad R^r = -\frac{2\pi im}{p} \langle p|V|-p \rangle. \quad (1.5)$$

Defining the Fourier transform

$$\tilde{V}(k) = \frac{1}{\sqrt{2\pi}} \int_{-\infty}^{\infty} dx V(x) e^{-ikx} \quad (1.6)$$

we get for $k = p/\hbar > 0$:

$$R^l = -\frac{\sqrt{2\pi}im}{k\hbar^2}\tilde{V}(-2k), \quad R^r = -\frac{\sqrt{2\pi}im}{k\hbar^2}\tilde{V}(2k). \quad (1.7)$$

Assuming that the potential is local and PT-symmetrical, we calculate the transition coefficient from them using generalized unitarity as $|T|^2 = 1 - R^{r*}R^l$.

To build a \mathcal{TR}/\mathcal{T} device we demand: $\tilde{V}(k) = \sqrt{2\pi}\alpha k$ ($k < 0$) and $\tilde{V}(k) = 0$ ($k \geq 0$). By inverse Fourier transformation, this implies

$$\begin{aligned} V(x) &= -\alpha \frac{\partial}{\partial x} \lim_{\epsilon \rightarrow 0} \frac{1}{x - i\epsilon} = \alpha \lim_{\epsilon \rightarrow 0} \frac{1}{(x - i\epsilon)^2} \\ &= \alpha \lim_{\epsilon \rightarrow 0} \left[\frac{x^2 - \epsilon^2}{(x^2 + \epsilon^2)^2} + i \frac{2x\epsilon}{(x^2 + \epsilon^2)^2} \right], \end{aligned} \quad (1.8)$$

which is indeed a local, PT-symmetric potential for α real. α is directly related to the reflection coefficient, within the Born approximation, $R^l = 4\pi im\alpha/\hbar^2$. As the Born approximation may differ from exact results we shall keep α as an adjustable parameter in the following.

In a possible physical implementation, the potential in eq. (1.8) will be approximated by keeping a small finite $\epsilon > 0$, see fig. 1.3(a). Then, its Fourier transform is $\tilde{V}(k) = \sqrt{2\pi}\alpha k e^{\epsilon k}$ ($k < 0$) and $\tilde{V}(k) = 0$ ($k \geq 0$). In figs. 1.3(b) and (c), the resulting coefficients for $\epsilon/d = 10^{-4}$ and two different values of α are shown. These figures have been calculated by numerically solving the Schrödinger equation exactly. Remarkably, the Born approximation contains all the information required to build the required potential shape up to a global factor. Such a prominent role of the Born approximation in inverse problems has been noted in different applications [15–17]. For a range of α , the potential gives $|R^r| \approx 0$, a nearly constant $|R^l|^2$, and $|T^r| = |T^l| \approx 1$ in a broad k -domain, see fig. 1.3(b). Adjusting the value of α , fig. 1.3(c), sets $|R^l| \approx 1$ as desired.

1.5 Discussion

Scattering asymmetries are necessary to develop technologically relevant devices such as one-way mirrors, filters and barriers, invisibility cloaks, diodes, or Maxwell demons. So far much effort has been devoted to build and apply local PT-symmetric potentials but the possible scattering asymmetries with them are

quite limited. We find that six device types with asymmetric scattering are possible when imposing 0 or 1 scattering coefficients. PT-symmetry can only realize one of them, but this symmetry is just one among eight possible symmetries of complex non-local potentials. The eight symmetries arise from the discovery that Klein's four-group $\{1, \Pi, \Theta, \Theta\Pi\}$, combined with two possible relations among the Hamiltonian, its adjoint, and the symmetry operators of the group, eqs. (1) and (2), produce all possible equalities among potential matrix elements after complex conjugation, coordinate inversion, the identity, and transposition. In other words, to have all possible such equalities, the conventional definition of a symmetry A in terms of its commutation with the Hamiltonian H is not enough, and A -pseudohermiticity must be considered as well on the same footing. Extending the concept of what a symmetry is for complex, non-local potentials is a fundamental, far-reaching step of this work. This group theoretical analysis and classification is not only esthetically pleasing, but also of practical importance, as it reveals the underlying structure and span of the possibilities available in principle to manipulate the asymmetrical response of a potential for a structureless particle.

We provide potentials for the different asymmetric devices including an example that works in a broad domain of incident momenta. Although the present theory is for the scattering of quantum particles, the analogies between quantum physics and optics suggest to extend the concepts and results for optical asymmetric devices.

Interesting questions left for future work are the inclusion of other mechanisms for transmission and reflection asymmetries (for example nonlinearities [8, 19], and time dependent potentials [20, 21]), or a full discussion of the phases of the scattering amplitudes in addition to the moduli emphasized here. In this paper the properties of the scattering amplitudes have been worked out assuming that the operator A in the symmetry relations in eqs. (1.1) and (1.2) is a unitary/antiunitary operator in Klein's group. We may generalize the study to include more general operators, possibly including differential operators, as was done in [22] for phase transitions of optical potentials, or the operator that swaps internal states or waveguides [23, 24].

We shall also examine in a complementary paper the physical realization of complex nonlocal effective potentials. In a quantum optics scenario, simple examples were provided in [25] based on applying the partitioning technique [26, 27]

to the scattering of a particle with internal structure. The experimental realization of all new symmetries and devices may be challenging, e.g. to engineer the nonlocality in optics, but there is much to gain. We may expect progress similar to the successful evolution from theory to actual devices in the sequence from the first mathematical models of PT-symmetric potentials [28], to the proposal of an optical realization [2], and to the actual experiments [29], even if considerable time lapses were needed between the three steps.

Chapter 2

Local rectification of heat flux

We present a chain-of-atoms model where heat is rectified, with different fluxes from the hot to the cold baths located at the chain boundaries when the temperature bias is reversed. The chain is homogeneous except for boundary effects and a local modification of the interactions at one site, the “impurity”. The rectification mechanism is due here to the localized impurity, the only asymmetrical element of the structure, apart from the externally imposed temperature bias, and does not rely on putting in contact different materials or other known mechanisms such as grading or long-range interactions. The effect survives if all interaction forces are linear except the ones for the impurity.

2.1 Introduction

In spite of much work on thermal rectification after the first model proposal in 2002 [30] (for a broad perspective on heat rectification see [31, 32]), the manipulation of phononic heat fluxes is still far from being completely controlled as no efficient and feasible thermal diodes have been found [33, 34]. The thermal rectifier, a device where the heat current changes when the temperature bias of the thermal baths at the boundaries is reversed, is one of the key tools needed to manipulate heat currents and build thermal circuits. A wealth of research is underway to meet the challenge posed by a “near standstill” of the field [33, 34], combined with the prospects of widespread and impactful practical applications. Together with experimental progress, at this stage work exploring new models is important to test possibilities that may become feasible as control capabilities improve [31]. In this paper we propose, motivated by previous work on “atom diodes” [35, 36], a rectifying scheme based on the effect of a local defect, or impurity, in an otherwise homogeneous system.

To date, there have been several proposals of systems that could be used to rectify heat flows at the nanoscale. A common scheme is based on coupling two or more different homogeneous segments, modelled with chains of atoms with non-linear interactions (which in this context means non-linear forces, i.e., anharmonic potentials) [30, 37–40] or with a temperature and position dependent conductivity assuming expressions for the heat current [39, 41]. Basic ingredients for thermal rectification have been considered to be the asymmetry in the system and non-linear interactions [32, 40, 42], which lead to a temperature dependence of the phonon bands, or power spectral densities, of the weakly coupled [38] segments. These bands match or mismatch at the interfaces, depending of the sign of the temperature bias, leading, respectively, to heat flow or insulating conditions. In fact, alternative mechanisms due to band mixing appear for stronger coupling or long chains [38], and Pereira [34], based on minimalist models, has recently reformulated the conditions leading to rectification as the combination of asymmetry plus the existence of some feature of the system that depends on the temperature (nonlinearity is certainly a possible cause of such dependence). Other systems proposed are graded materials, such as a chain with an uneven distribution of mass [33, 42, 43], and long-range interactions have been shown to be able to amplify the rectification and avoid or mitigate the decay of the effect with system size [33, 44]. Also, recent models and experiments use asymmetrical homogeneous or

inhomogeneous nanostructures and, in particular, graphene [45, 46]. Finally, we mention for completeness theoretical works that consider the use of a quantum system [31], such as a three-level system, with each level coupled to a thermal bath [47], or a double well with different frequencies to implement the asymmetry [48].

The model proposed in this paper is a one-dimensional chain of atoms where all, except one of them, are trapped in on-site harmonic potentials and interact with their nearest neighbours by Morse potentials (or also by harmonic potentials in a simplified version). Unlike most chain models, the structural asymmetry is, except for the boundaries, only in the impurity, which is subjected to a different on-site potential and interaction with one of its neighbors. The chain is connected to thermal baths at different temperatures at the boundaries. Let us clarify our terminology: The structural asymmetry we have in mind amounts, to different interaction potentials of one or several atoms in the chain (other than the boundary atoms) with neighbors on the right and on the left, and/or asymmetric onsite potentials. In this regard chains with Morse interatomic potentials per se are not considered structurally asymmetric here as long as their parameters are the same on both sides of a given atom, even if a single Morse potential is obviously asymmetric with respect to its minimum [49].

First, we shall describe the homogeneous 1D chain, without the impurity, and show its heat conduction behavior. Then we modify the potentials for one of the atoms and demonstrate the rectification effect.

2.2 Homogeneous one-dimensional chain

We start with a homogeneous 1D chain with N atoms coupled at both extremes to heat baths, at different temperatures T_h and T_c for “hot” and “cold” respectively. The baths are modeled with a Nosé-Hoover method as described in [50]. Atoms 1 and N represent the first and the N -th atom in the chain, from left to right, that will be in contact with the baths. All the atoms are subjected to on-site potentials and to nearest-neighbor interactions, and their equilibrium positions y_{i0} are assumed to be equally spaced by a distance a . $x_i = y_i - y_{i0}$, $i = 1, \dots, N$, represent the displacements from the equilibrium positions of the corresponding atoms with positions y_i .

The classical Hamiltonian of the atom chain can be written in a general form as

$$H = \sum_{i=1}^N H_i, \quad (2.1)$$

with

$$\begin{aligned} H_1 &= \frac{p_1^2}{2m} + U_1(x_1) + V_L, \\ H_i &= \frac{p_i^2}{2m} + U_i(x_i) + V_i(x_{i-1}, x_i) \quad i = 2, \dots, N-1, \\ H_N &= \frac{p_N^2}{2m} + U_N(x_N) + V_N(x_{N-1}, x_N) + V_R, \end{aligned} \quad (2.2)$$

where the p_i are the momenta, $U_i(x_i)$ is the on-site potential for the i th atom, and $V_i(x_{i-1}, x_i)$ represents the atom-atom interaction potential. V_R and V_L are the interactions coupling the boundary atoms to the Nosé-Hoover thermostats, see [50].

There are a large number of 1D models that obey this general Hamiltonian. Using different potentials for the trapping and interactions we would get different conductivity behaviors. We choose a simple form of the Hamiltonian in which each atom is subjected to a harmonic on-site potential and a Morse interaction potential between nearest neighbors (see fig. 2.1, dashed lines),

$$U_i(x_i) = \frac{1}{2}m\omega^2 x_i^2, \quad (2.3)$$

$$V_i(x_{i-1}, x_i) = D \{e^{-\alpha[x_i - x_{i-1}]} - 1\}^2, \quad (2.4)$$

where ω is the trapping angular frequency, and D and α are time independent parameters of the Morse potential. A “minimalist version” of the model where V becomes the harmonic limit of eq. (2.4), dotted line in fig. 1, will also be considered in the final discussion,

$$V_i(x_{i-1}, x_i) = k(x_i - x_{i-1})^2/2, \quad k = 2D\alpha^2. \quad (2.5)$$

For convenience, dimensionless units are used and the mass of all particles is set to unity.

We start by studying the homogeneous configuration with no impurity and potentials (2.3) and (2.4), solving numerically the dynamical equations for the Hamiltonian (2.1) with a Runge-Kutta-Fehlberg algorithm. We have chosen a

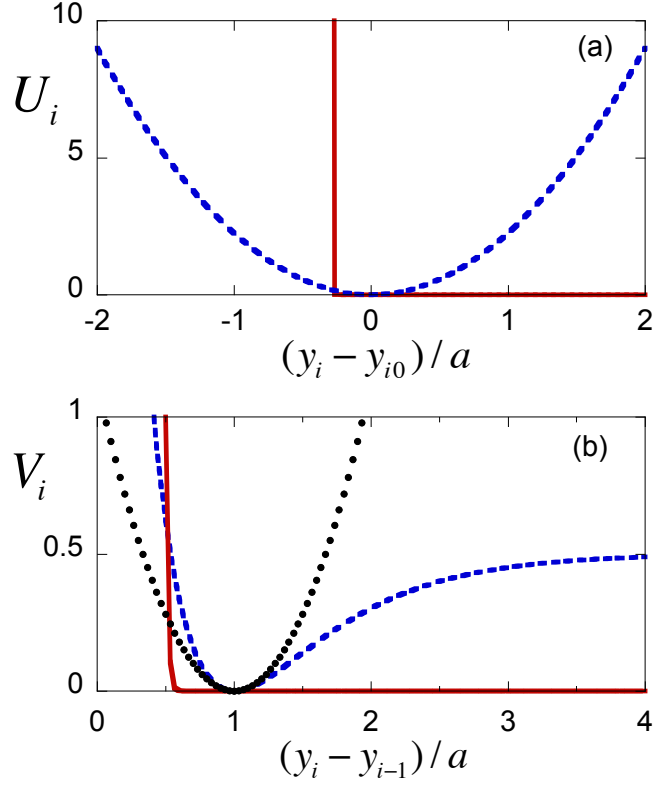


FIGURE 2.1: (Color online) (a) On-site potentials: harmonic potential centered at the equilibrium position of each atom (dashed blue line) as a function of the displacement from this position $x_i = y_i - y_{i0}$ in a -units, and the on-site potential for the impurity, $i = N/2 + 1$ (N even, red solid line). (b) Interaction potentials as a function of the distance between nearest neighbors: Morse potential (blue dashed line) valid for all atoms except for $i = N/2 + 1$, N even, where the modified potential (red solid line) is used. The harmonic approximation of the Morse potential is also depicted (eq. (2.5), black dots, only used for fig. 5, below). Parameters: $D = 0.5$, $g = 1$, $\gamma = 45$, $d = 100$ and $b = 105$, used throughout the paper.

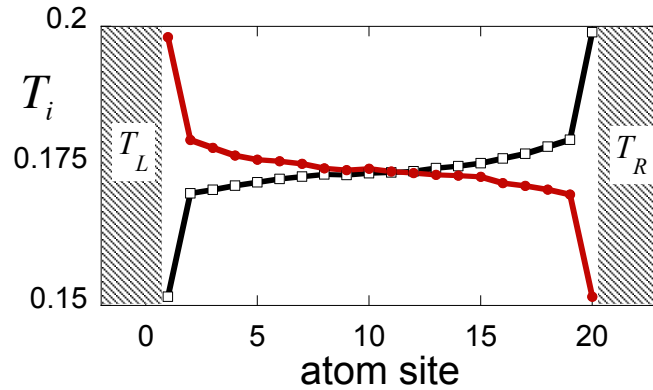


FIGURE 2.2: (Color online) Symmetric temperature profiles for a homogeneous chain, without impurity. For $T_h = T_L$, $T_c = T_R$ (red solid dots) the (absolute value of) the heat flux is $J_{L \rightarrow R}$, equal to $J_{R \rightarrow L}$ for the reverse configuration of the bath temperatures, $T_h = T_R$, $T_c = T_L$ (black empty squares). Parameters as in fig. 1.

low number of atoms, $N = 20$, with thermal baths at $T_h = 0.20$ and $T_c = 0.15$ at both ends of the chain with 16 thermostats each. The real temperature is related to the dimensionless one through $T_{real} = Tma^2\omega^2/k_B$ so, for typical values $m \approx 10^{-26}$ kg, $\omega \approx 10^{13}$ s $^{-1}$, $a \approx 10^{-10}$ m, and using $k_B = 1.38 \times 10^{-23}$ JK $^{-1}$, the dimensionless temperatures 0.15, 0.20, translate into 100, 150 K. It is advisable to use temperatures around these values so that we ensure that the displacements of the particles are realistic [51].

First we demonstrate the conductivity behavior of the model. To this end, we calculate the local heat flux J_i and temperature T_i , performing the numerical integration for long enough times to reach the stationary state. The local temperature is found as the time average $T_i = \langle p_i^2/m \rangle$, whereas J_i , from the continuity equation [52], is given by

$$J_i = -\dot{x}_i \frac{\partial V(x_{i-1}, x_i)}{\partial x_i}. \quad (2.6)$$

From now on we only consider the time average $\langle J_i(t) \rangle$, which converges to a constant value for all sites once the system is in the stationary nonequilibrium state. We depict the temperature profiles, for $N = 20$, first with $T_L = T_h$ and $T_R = T_c$ (L and R stand for left and right) and after switching the positions of the thermal baths in fig. 2.2. The profiles are symmetric, as expected, and the heat flux does not have a preferred direction [30, 52]. Denoting the absolute values of the fluxes from the left (when $T_L = T_h$) as $J_{L \rightarrow R}$, and from the right (when $T_R = T_h$) as $J_{R \rightarrow L}$, we find that $J_{L \rightarrow R} = J_{R \rightarrow L} = J = 1.6 \times 10^{-2}$, in the dimensionless units, consistent with the values found in other models [30, 52].

The profile of the temperature is linear with boundary nonlinearities at the edges, close to the thermal baths, due to the boundary conditions [53]. In fig. 2.3 we depict T_i vs i/N for $N = 100, 125$ and 150 with the same boundary conditions. For these larger atom numbers we have connected the first 3 and the last 3 atoms to the Nosé-Hoover baths. In the inset (a) of fig. 2.3 the product JN is plotted vs. N showing that in a low N limit there is a well defined conductivity per unit length whereas for longer chains, JN tends to be constant which indicates a normal thermal conductivity independent of the length. Fixing the number of atoms to 100, as in the inset (b) of fig. 2.3, we observe a linear dependence between the flux and ΔT .

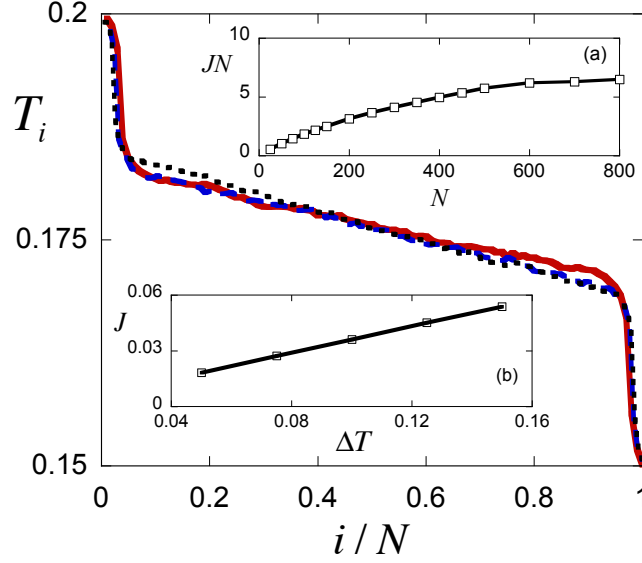


FIGURE 2.3: (Color online) Temperature profile along the homogeneous chain for different number of atoms: 100 (dotted black line), 125 (dashed blue line) and 150 (solid red line). The atom sites have been rescaled with the total number of atoms. The time averages have been carried over a time interval of $\approx 2 \times 10^6$ after a transient of $\approx 1 \times 10^5$. In the inset (a), the product JN vs. N demonstrates that for long chains JN is independent of N . In (b) the linear dependence of J with ΔT for a fixed number of atoms, $N = 100$, is shown. Parameters as in fig. 1.

2.3 Impurity-based thermal rectifier

To rectify the heat flux we modify the potentials for site $j = N/2 + 1$ with N even, as

$$U_j(x_j, t) = de^{-b[x_j(t)+a/3]}, \quad (2.7)$$

$$V_j(x_{j-1}, x_j, t) = ge^{-\gamma[x_j(t)-x_{j-1}(t)+a/2]}. \quad (2.8)$$

All the parameters involved, d, b , and g, γ are time independent. In fig. 2.1 the modifications introduced with respect to the ordinary sites are shown (solid lines). The different on-site and interaction terms introduce soft-wall potentials (instead of hard-walls to aid integrating the dynamical equations) that make it difficult for the impurity to transmit its excitation to the left whereas left-to-right transmission is still possible. This effect is facilitated by the relative size of the coefficients, $a/3 < a/2$, that determine the position of the walls. These positions imply that an impurity excited by a hot right bath cannot affect its left cold neighbour near its equilibrium position at the $j - 1$ site. However, if the left $j - 1$ atom is excited

from a hot bath on the left, it can get close enough to the impurity to kick it and transfer kinetic energy. The asymmetrical behavior relies on the asymmetry of the potentials and the temperatures of neighboring atoms; it does not require breaking time-reversal invariance. All collisions are elastic and time reversible.

After extensive numerical simulations, we have chosen the values of these parameters as in fig. 1, such that the conductivity in the forward direction, $J_{L \rightarrow R}$, and the rectification factor, defined as $R = (J_{L \rightarrow R} - J_{R \rightarrow L})/J_{R \rightarrow L} \times 100$, are both large for $T_h = 0.2$, $T_c = 0.15$. A large R without a large $J_{L \rightarrow R}$ could in fact be useless [31]. Note that the parameters are not necessarily the optimal combination, which in any case would depend on the exact definition of “optimal” (technically on how $J_{L \rightarrow R}/J$ and R are weighted and combined in a cost function and on the limits imposed on the parameter values). This definition is an interesting question but it goes beyond the focus of our paper, which is to demonstrate and discuss the effect of the localized impurity.

We have used again $N = 20$ connected to baths of 16 thermostats each, with the same temperatures as for the homogeneous chain, and numerically solved the dynamical equations to calculate the local temperature and the heat flux for both configurations of the baths. The interatomic potential for the regular atoms is the Morse potential (2.4). In fig. 2.4(a), the temperature profiles show a clear asymmetry between $L \rightarrow R$ and $R \rightarrow L$. Specifically, we find $J_{L \rightarrow R} = 7.6 \times 10^{-3}$ and $J_{R \rightarrow L} = 5.8 \times 10^{-3}$ which gives $R = 31\%$. The effect decays with longer chains, with, for example, $R = 19\%$ for $N = 100$, and $R = 17.8\%$ for $N = 150$.

These temperature profiles depend on the difference between the bath temperatures, see e.g. fig. 2.4(b). Increasing the temperature gap, but keeping T_h low enough so that the displacement of the atoms from their equilibrium positions is realistic, we find higher values of R . Figure 2.5 shows the strong dependence of R with ΔT (black circles). We have changed both T_h and T_c so that the mean temperature $(T_c + T_h)/2$ remains constant.

2.4 Discussion

We have presented a scheme for thermal rectification using a one-dimensional chain of atoms which is homogeneous except for the special interactions of one of them, the impurity, and the couplings with the baths at the boundaries. Our

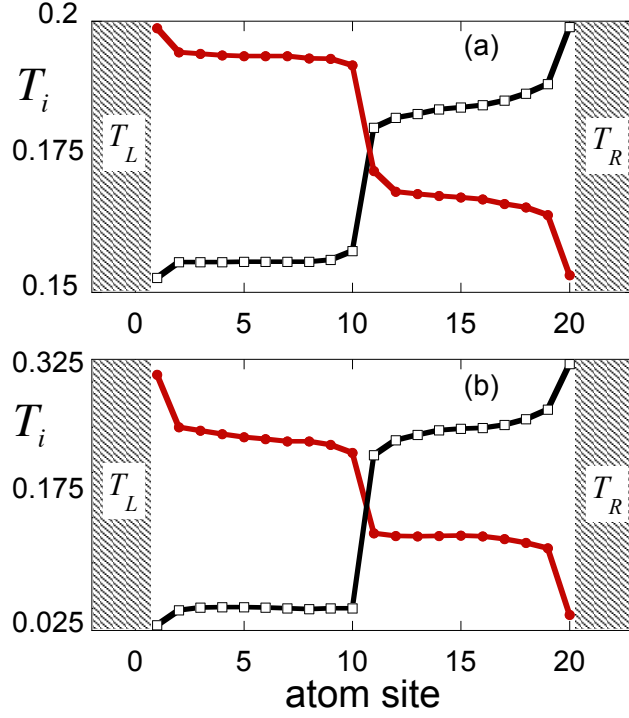


FIGURE 2.4: (Color online) Temperature profile for the chain of $N = 20$ atoms, with an impurity in the $N/2 + 1$ position, with $T_L = T_h$ and $T_R = T_c$ (circles) and with the thermostat baths switched (squares). Parameters as in fig. 1. (a) $T_c = 0.15$, $T_h = 0.2$. $J_{L \rightarrow R} = 0.00769$ vs $J_{R \rightarrow L} = 0.00581$, with gives a rectification $R = 31\%$; (b) $T_c = 0.025$, $T_h = 0.325$. $J_{L \rightarrow R} = 0.0499$ vs $J_{R \rightarrow L} = 0.0140$, with $R = 256\%$.

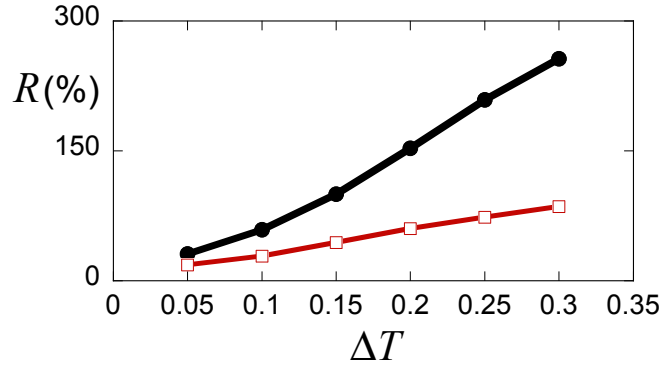


FIGURE 2.5: (Color online) Rectification factor R as a function of the temperature difference between ends of the chain of atoms, ΔT . We have changed both T_h and T_c according to $T_c = 0.15 - (\Delta T - 0.05)/2$ and $T_h = 0.2 + (\Delta T - 0.05)/2$, with $N = 20$, keeping the rest of parameters as in fig. 2.1. Interatomic potentials: Morse potential, eq. (2.4) (black line with circles, see the temperature profiles of extreme points in fig. 4); harmonic potential, eq. (2.5) (red line with squares).

proof-of-principle results for an impurity-based rectification mechanism encourage further exploration of the impurity-based rectification, in particular of the effect of different forms for the impurity on-site potential and its interactions with neighboring atoms. In contrast to the majority of chain models, the structural asymmetry in our model is only in the impurity. The idea of a localized effect was already implicit in early works on a two-segment Frenkel-Kontorova model [37, 38], where rectification depended crucially on the interaction constant coupling between the two segments. However, the coupling interaction was symmetrical and the asymmetry was provided by the different nature (parameters) of the segments put in contact. Also different from common chain models are the potentials chosen here. Instead of using the Morse potential as an on-site model, see e.g. [30], we have considered a natural setting where this potential characterizes the interatomic interactions, and the on-site potential is symmetrical with respect to the equilibrium position, and actually harmonic. The numerical results indicate that this model is consistent with normal conduction, and also helps to isolate and identify the local-impurity mechanism for rectification. In this regard it is useful to consider a further simplification, in the spirit of the minimalists models proposed by Pereira [34], so as to distill further the essence of the local rectification mechanism. If the Morse interatomic interaction is substituted by the corresponding harmonic interaction, see the black dotted line in fig. 1b, the rectification effect remains, albeit slightly reduced, see fig. 2.5. The chain is then perfectly linear with the only nonlinear exception localized at the impurity. The temperature dependent feature mentioned in [34] as the second necessary condition for rectification besides asymmetry, is here localized in the impurity too, and consists of a different capability to transfer kinetic energy depending on the temperatures on both sides of the impurity. Figure 6 shows temperature profiles for the purely harmonic chain to be compared with the Morse-interaction chain in fig. 4. Flatter profiles are found on both sides of the impurity, as corresponds to the abnormal transport expected for harmonic chains [54]. It would be interesting to combine the impurity effect with other rectification mechanisms (such as grading, long-range interactions, or use of different segments), or with more impurities in series to enhance further the rectification effect.

Even though our motivation was to mimic the effect of a localized atom diode that lets atoms pass only one way, unlike the atom diode [35], all interactions in the present model are elastic. The model may be extended by adding an irreversible, dissipative element so as to induce not only rectification but a truly Maxwell

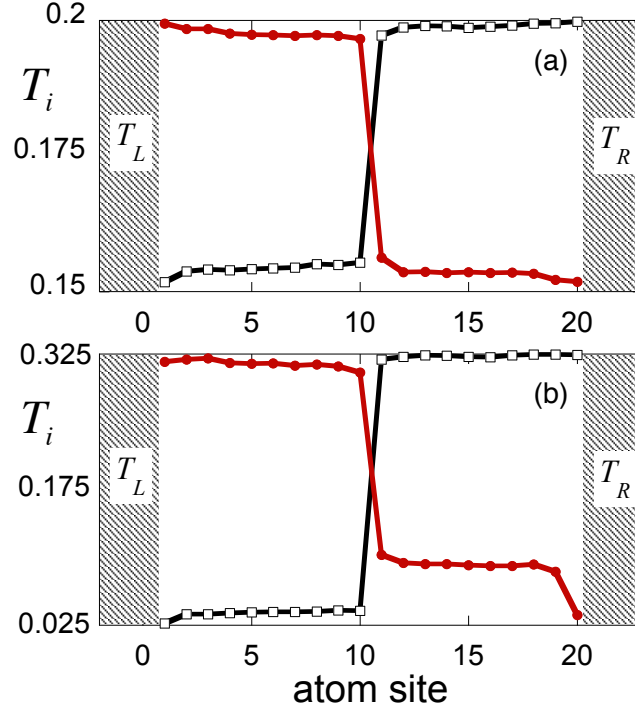


FIGURE 2.6: (Color online) Temperature profile for a harmonic interacting chain of $N = 20$ atoms, with an impurity in the $N/2 + 1$ position, with $T_L = T_h$ and $T_R = T_c$ (circles) and with the thermostat baths switched (squares), for (a) $\Delta T = 0.05$ and (b) $\Delta T = 0.3$. The corresponding rectification factors are (a) $R = 18\%$ and (b) $R = 85\%$. Parameters regarding the impurity are the same as in fig. 1.

demon for heat transfer [55, 56]. On the experimental side, one dimensional chains of neutral atoms in optical lattices can be implemented with cold atoms [57]. An impurity with different internal structure could be subjected to a different on-site potential imprinted by a holographic mask [58], and asymmetrical interatomic interactions could be implemented by trapping a controllable polar molecule or mediated by atoms in parallel lattices [59].

We are indebted to G. Casati for raising our attention to thermal rectification and for providing information on his work. We acknowledge financial support by the Basque Government (Grant No. IT986-16) and MINECO/FEDER,UE (Grant No. FIS2015-67161-P). Reid

Chapter 3

Chain of Ions

We numerically demonstrate heat rectification for linear chains of ions in trap lattices with graded trapping frequencies, in contact with thermal baths implemented by optical molasses. To calculate the local temperatures and heat currents we find the stationary state by solving a system of algebraic equations. This approach is much faster than the usual method that integrates the dynamical equations of the system and averages over noise realizations.

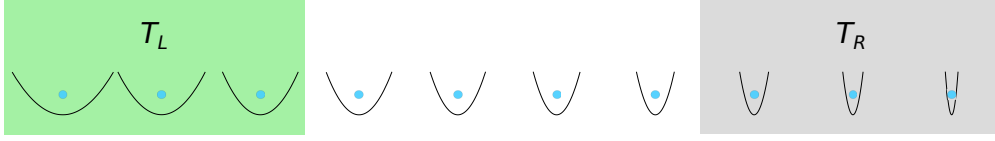


FIGURE 3.1: Schematic representation of the frequency-graded chain of trapped ions proposed as a thermal rectifier. The left and right ends of the chain are in contact with optical molasses at temperatures T_L and T_R (green and grey boxes respectively). Each ion is in an individual trap. The (angular) frequencies of the traps increase homogeneously from left to right, starting from ω_1 and ending at $\omega_1 + \Delta\omega$. The ions interact through the Coulomb force, which is long range, and therefore all the ions interact among them, even distant neighbors. By default we use 15 ions.

3.1 Introduction

The ideal thermal rectifier, also “thermal diode”, is a device that allows heat to propagate in one direction, from a hot to a cold bath, but not in the opposite one when the temperature bias of the baths is reversed. The name is set by analogy to the half-wave rectifiers or diodes for electric current. More generally thermal rectification simply denotes asymmetric heat flows (not necessarily all or nothing) when the bath temperatures are reversed. Thermal rectification was discovered by C. Starr in 1936 in a junction between copper and cuprous oxide [60]. Many years later, a work of Terraneo *et al.* demonstrated thermal rectification in a model consisting on a segmented chain of coupled nonlinear oscillators in contact with two thermal baths at temperatures T_H and T_C , with $T_H > T_C$ [30]. This paper sparked a substantial body of research that spans to this day [61] (see Fig. 1 in [31]).

Research on thermal rectification has gained a lot of attention in recent years as a key ingredient to build prospective devices to control heat flows similarly to electrical currents [31, 32]. There are proposals to engineer thermal logic circuits [62] in which information, stored in thermal memories [63], would be processed in thermal gates [64]. Such thermal gates, as their electronic counterparts, will require thermal diodes and thermal transistors to operate [47, 65]. Heat rectifying devices would also be quite useful in nano electronic circuits, letting delicate components dissipate heat while being protected from external heat sources [31].

Most work on thermal diodes has been theoretical with only a few experiments [43, 66–68]. A relevant attempt to build a thermal rectifier was based on a graded

structure made of carbon and boron nitride nanotubes that transports heat between a pair of heating/sensing circuits [43]. One of the ends of the nanotube is loaded with a deposition of another material, which makes the heat flow better from the loaded end to the unloaded end. However, rectifications were small, with rectification factors (relative heat-flow differentials) around 7%.

Much effort has been aimed at improving the rectification factors and the features of the rectifiers. Some works relied, as in [30], on a chain segmented into two or more regions with different properties, but using other lattice models such as the Frenkel-Kontorova (FK) model [38, 69]. The fundamental ingredient for having rectification was attributed to nonlinear forces in the chain [32, 38, 40, 42, 48, 69], which lead to a temperature dependence of the phonon bands or power spectral densities. The bands may match or mismatch at the interfaces depending on the sign of the temperature bias of the baths, allowing or obstructing heat flow [30, 37]. Later, alternative mechanisms have been proposed which do not necessarily rely on anharmonic potentials [34, 70]. Also, Peyrard provided a simple model to explain and build rectifiers based on assuming the Fourier law for heat conduction locally combined with a temperature and position-dependent conductivity [39].

It was soon realized that the performance of segmented rectifiers was very sensitive to the size of the device, i.e., rectification decreases with increasing the length of the rectifier [38]. To overcome this limitation two ideas were proposed. The first one consists in using graded rather than segmented chains, i.e., chains where some physical property varies continuously along the site position such as the mass of particles in the lattice [33, 71–78]. The second one uses particles with long-range interactions (LRI), such that all the particles in the lattice interact with each other [33, 44, 79]. The rationale behind was that in a graded system new asymmetric, rectifying channels are created, while the long-range interactions create also new transport channels, avoiding the usual decay of heat flow with size [33]. Besides a stronger rectification power, LRI graded chains are expected to have better heat conductivity than segmented ones. This is an important point for technological applications, because devices with high rectification factors are not useful if the currents that flow through them are very small.

In this article we propose to bridge the gap between mathematical models and actual systems exploring the implementation of a heat rectifier in a realistic, graded system with long-range interactions: a chain of ultracold ions in a segmented Paul trap with graded microtraps for each ion. Long-range interactions are due to the

Coulomb forces, and the baths at the ends of the chain may be implemented with optical molasses, see Fig. 3.1. The trapping frequencies of the microtraps are controlled individually in order to create a graded and asymmetric trap-frequency profile along the chain. This asymmetry will lead to a heat flow that depends on the sign of the temperature difference of the baths. Heat transport in trapped ion chains has been studied in several works [80–84] and interesting phenomena like phase transitions have been investigated [80–83]. The idea of using locally-controlled traps is already mentioned in [80] to implement disorder and study its effects. The device we present here may be challenging to implement, but at reach with the current technology, in particular that of microfabricated traps [85–87]. Thus the setting is thought for a small, realistic number of controllable ions.

The rest of the article is organized as follows. In Section 3.2 we describe the physical system of trapped ions with graded trap frequencies. We also set the stochastic dynamics due to the action of lasers at the chain edges. In Section 3.3 we implement an efficient method to find the steady state using Novikov’s theorem and solving an algebraic system of equations. In Section 3.4 we present simulations of this system exhibiting thermal rectification and discuss the dependence with ion number, different options for the ion-laser coupling, and the advantages/disadvantages of using a graded frequency profile instead of a segmented one. Finally, in Section 3.5 we summarize our conclusions, and discuss connections with other works.

3.2 Physical System

Consider a linear lattice of N individual harmonic traps of (angular) trapping frequencies ω_n evenly distributed along the x axis at a distance a from each other. Each trap contains a single ion that interacts with the rest via Coulomb potentials. All the ions are of the same species, with mass m and charge q . The Hamiltonian that describes the dynamics of the system is (we consider only linear, one dimensional motion along the chain axis)

$$H(\mathbf{x}, \mathbf{p}) = \sum_{n=1}^N \left[\frac{p_n^2}{2m} + \frac{m\omega_n^2}{2} (x_n - x_n^{(0)})^2 \right] + V_{int}(\mathbf{x}), \quad (3.1)$$

where $\{x_n, p_n\}$, position and momentum of each ion, are the components of the vectors \mathbf{x}, \mathbf{p} , $x_n^{(0)} = na$ are the centers of the harmonic traps, and V_{int} is the sum of the Coulomb interaction potential between all pairs of ions,

$$V_{int}(\mathbf{x}) = \frac{1}{2} \sum_n \sum_{l \neq n} V_C(|x_n - x_l|), \quad (3.2)$$

with $V_C(|x_n - x_l|) = \frac{q^2}{4\pi\epsilon_0} \frac{1}{|x_n - x_l|}$. The ends of the chain are in contact with two thermal reservoirs at temperatures T_L for the left bath and T_R for the right bath respectively. The action of the reservoirs on the dynamics of the chain is modeled via Langevin baths at temperatures T_L and T_R [54, 88]. The equations of motion of the chain, taking into account the baths and the Hamiltonian, are

$$\begin{aligned} \dot{x}_n &= \frac{1}{m} p_n, \\ \dot{p}_n &= -m\omega_n^2(x_n - x_n^{(0)}) - \frac{\partial V_{int}}{\partial x_n} - \frac{\gamma_n}{m} p_n + \xi_n(t), \end{aligned} \quad (3.3)$$

where γ_n and $\xi_n(t)$ are only non-zero for the ions in the end regions, in contact with the left and right baths in the sets $\mathcal{L} = \{1, 2, \dots, N_L\}$ and $\mathcal{R} = \{N - (N_R - 1), \dots, N - 1, N\}$, see Fig. 3.1. The γ_n are friction coefficients and $\xi_n(t)$ are uncorrelated Gaussian noise forces satisfying $\langle \xi_n(t) \rangle = 0$ and $\langle \xi_n(t) \xi_m(t') \rangle = 2D_n \delta_{nm} \delta(t - t')$, D_n being the diffusion coefficients. These Gaussian forces are formally the time derivatives of independent Wiener processes (Brownian motions) $\xi_n(t) = \sqrt{2D_n} \frac{dW_n}{dt}$ [81, 89] and Eq. (3.3) is a stochastic differential equation (SDE) in the Stratonovich sense [89].

The baths are physically implemented by optical molasses consisting of a pair of counterpropagating Doppler-cooling lasers [81]. The friction and diffusion coefficients for the ions in contact with the baths are given by [81, 90, 91]

$$\begin{aligned} \gamma_n &= -4\hbar k_{L,R}^2 \left(\frac{I_{L,R}}{I_0} \right) \frac{2\delta_{L,R}/\Gamma}{[1 + (2\delta_{L,R}/\Gamma)^2]^2}, \\ D_n &= \hbar^2 k_{L,R}^2 \left(\frac{I_{L,R}}{I_0} \right) \frac{\Gamma}{1 + (2\delta_{L,R}/\Gamma)^2}, \\ n &\in \mathcal{L}, \mathcal{R}, \end{aligned} \quad (3.4)$$

where k_L (k_R) and I_L (I_R) are the wave vector and intensity of the left (right) laser. δ_L (δ_R) is the detuning of the left (right) laser with respect to the angular frequency ω_0 of the atomic transition the laser is exciting, and Γ is the corresponding natural

line width of the excited state. The expressions in Eq. (3.4) are valid only if the intensities of the lasers are small compared to the saturation intensity I_0 , $I_{L,R}/I_0 \ll 1$. In this bath model, the friction term in Eq. (3.3) comes from the cooling action of the laser and the white noise force $\xi_n(t)$ corresponds to the random recoil of the ions due to spontaneous emission of photons [90, 91]. Using the diffusion-dissipation relation $D = \gamma k_B T$ [92], the temperatures of the optical molasses baths are given by

$$T_{L,R} = -\frac{\hbar\Gamma}{4k_B} \frac{1 + (2\delta_{L,R}/\Gamma)^2}{(2\delta_{L,R}/\Gamma)}, \quad (3.5)$$

with k_B being the Boltzmann constant. If the laser intensities are low enough, the temperatures of the baths are controlled by modifying the detunings. When $\delta = \delta_D = -\Gamma/2$ the optical molasses reach their minimum temperature possible, the Doppler limit $T_D = \hbar\Gamma/(2k_B)$. Note that away from the Doppler limit the same temperature may be achieved for two different values of detuning. These two possibilities imply different couplings (two different pairs of γ and D values) and thus different physical effects that will be studied in Sec. 3.4.3.

3.3 Calculation of the stationary heat currents

The local energy of each site is defined by

$$H_n = \frac{1}{2m}p_n^2 + \frac{1}{2}m\omega_n^2(x_n - x_n^{(0)})^2 + \frac{1}{2}\sum_{l \neq n} V_C(|x_n - x_l|). \quad (3.6)$$

Differentiating H_n with respect to time we find the continuity equation

$$\dot{H}_n = \frac{p_n}{m} \left[\xi_n(t) - \gamma_n \frac{p_n}{m} \right] - \frac{1}{2m} \sum_{l \neq n} \frac{\partial V_C(|x_n - x_l|)}{\partial x_n} (p_n + p_l). \quad (3.7)$$

Two different contributions can be distinguished: $j_n^B \equiv \frac{p_n}{m} [\xi_n(t) - \gamma_n \frac{p_n}{m}]$, which is the energy flow from the laser reservoir to the ions at the edges of the chain (only for $n \in \mathcal{L}, \mathcal{R}$), and $\dot{H}_n^{int} \equiv -\frac{1}{2m} \sum_{l \neq n} \frac{\partial V_C(|x_n - x_l|)}{\partial x_n} (p_n + p_l)$, which gives the “internal” energy flow due to the interactions with the rest of the ions. In the steady state $\langle \dot{H}_n \rangle = 0$, and therefore

$$\langle j_n^B \rangle + \langle \dot{H}_n^{int} \rangle = 0, \quad (3.8)$$

where $\langle \dots \rangle$ stands for the expectation value with respect to the ensemble of noise processes $\boldsymbol{\xi}(t)$ ($\boldsymbol{\xi}$ represents a vector with components ξ_n). Equation (3.8) implies that, in the steady state, the internal rates \dot{H}_n^{int} vanish for the inner ions of the chain because $j_n^B = 0$ for $n \notin \mathcal{L}, \mathcal{R}$. In chains with nearest-neighbor (NN) interactions, $\langle \dot{H}_n^{int} \rangle$ simplifies to two compensating and equal-in-magnitude contributions that define the homogeneous heat flux across the chain. For long-range interactions this is not so and defining the flux is not so straightforward. A formal possibility is to impose nearest-neighbor interatomic interactions for some atoms in the chain [33], but this approach is not realistic in the current system so we define instead the heat currents for the left and right baths as

$$\begin{aligned} J_L(t) &= \sum_{n \in \mathcal{L}} \langle j_n^B \rangle, \\ J_R(t) &= \sum_{n \in \mathcal{R}} \langle j_n^B \rangle, \end{aligned} \tag{3.9}$$

respectively. These expressions are in general time-dependent. In the steady state we must have $J_{L,\text{steady}} + J_{R,\text{steady}} = 0$, since the local energies stabilize and internal energy flows cancel. We use either $J_{L,\text{steady}}$ or $J_{R,\text{steady}}$ to calculate the total energy flow in the chain, always taking the absolute value, i.e., $J \equiv |J_{L,\text{steady}}| = |J_{R,\text{steady}}|$. J is defined as J_{\rightarrow} when the hot bath is on the left and J_{\leftarrow} when it is on the right.

To compute the average heat fluxes of the baths $\langle j_n^B \rangle$ in Eq. (3.9) we need the averages $\langle p_n(t) \xi_n(t) \rangle$. Instead of explicitly averaging $p_n(t) \xi_n(t)$ over different realizations of the white noise we use Novikov's theorem [89, 93, 94]. Novikov's theorem states that the ensemble average (over the realizations of the noise) of the product of some functional $\phi(t)$, which depends on a Gaussian noise $\xi(t)$ with zero mean value, $\langle \xi(t) \rangle = 0$, and the noise itself, is given by

$$\langle \xi(t) \phi(t) \rangle = \int_0^t dt' \langle \xi(t) \xi(t') \rangle \left\langle \frac{\delta \phi(t)}{\delta \xi(t')} \right\rangle, \tag{3.10}$$

where $\delta \phi(t) / \delta \xi(t')$ is the functional derivative of $\phi(t)$ with respect to the noise, with $t' < t$. When the noise is δ -correlated, $\langle \xi(t) \xi(t') \rangle = 2D\delta(t - t')$, and Eq. (3.10) reads $\langle \xi(t) \phi(t) \rangle = D \langle \delta \phi(t) / \delta \xi(t') \rangle|_{t' \rightarrow t-}$. To apply Novikov's theorem to our model we need the functional derivatives of the position $x_n(t)$ and momentum $p_n(t)$ coordinates with respect to the white noises. We integrate Eq. (3.3) to have

its formal solution as a functional depending on the white Gaussian noises $\xi_n(t)$,

$$\begin{aligned} x_n(t) &= x_n(0) + \frac{1}{m} \int_0^t ds p_n(s), \\ p_n(t) &= p_n(0) + \int_0^t ds \left[-\frac{\partial H}{\partial x_n}(s) - \frac{\gamma_n}{m} p_n(s) + \xi_n(s) \right]. \end{aligned} \quad (3.11)$$

Equation (3.11) implies that the functional derivatives are $\delta x_n(t)/\delta \xi_m(t')|_{t' \rightarrow t^-} = 0$ and $\delta p_n(t)/\delta \xi_m(t')|_{t' \rightarrow t^-} = \delta_{nm}$ (δ_{nm} is the usual Kronecker delta symbol). Thus we have $\langle x_n(t) \xi_n(t) \rangle = 0$ and $\langle p_n(t) \xi_m(t) \rangle = \delta_{nm} D_m$, which gives for the heat flow from the baths

$$\langle j_n^B \rangle = \frac{1}{m} \left[D_n - \gamma_n \frac{\langle p_n^2 \rangle}{m} \right]. \quad (3.12)$$

In all simulations we check that $|J_{L,\text{steady}}| = |J_{R,\text{steady}}|$ within the numerical tolerance of the computer. To measure the asymmetry of the heat currents we use the rectification factor R defined as

$$R = \frac{J_{\rightarrow} - J_{\leftarrow}}{\max(J_{\rightarrow}, J_{\leftarrow})}. \quad (3.13)$$

R values may go from -1 to 1 (In the figures we depict it in % between -100% and 100%). If there is no rectification $J_{\rightarrow} = J_{\leftarrow}$ and $R = 0$. For perfect rectification in the right (left) direction, $J_{\rightarrow} \gg J_{\leftarrow}$ ($J_{\rightarrow} \ll J_{\leftarrow}$), and $R = 1$ ($R = -1$). Take note that other definitions of rectification factors exist in many works on asymmetric heat transfer so comparisons should be done with care.

This model does not show the antithermodynamical behavior observed in other models [95, 96], and heat is found to flow in all cases from the hot to the cold bath.

3.3.1 Algebraic, small-oscillations approach to calculate the steady state

To find the temperature profiles and heat currents in the steady state the usual approach is to solve the SDE system in Eq. (3.3) up to long times and for many realizations of the white noises $\xi(t)$. In that way the ensemble averages $\langle p_n(t \rightarrow \infty)^2 \rangle$, necessary for both the temperature profiles and heat currents, are computed. This standard route implies a heavy computational effort, in particular when we want to study the heat transport for several bath configurations,

frequency increments and chain parameters. It is possible to circumvent this difficulty and find ensemble averages like $\langle x_n x_m \rangle$, $\langle x_n p_m \rangle$, $\langle p_n p_m \rangle$ (second order moments) without integrating any SDE [97]. The idea is to impose the condition $d\langle \dots \rangle/dt = 0$ for all the second order moments and linearize the dynamical equations of the system around equilibrium. A system of linear algebraic equations for the moments results, that can be easily solved without solving the SDE many times.

To linearize the SDE in Eq. (3.3) we approximate the potential energy of the Hamiltonian in Eq. (3.1), $V(\mathbf{x}) = V_{int}(\mathbf{x}) + m \sum_n \omega_n^2 (x_n - x_n^{(0)})^2/2$, by its harmonic approximation around the equilibrium positions \mathbf{x}^{eq} , defined by $\left. \frac{\partial V(\mathbf{x})}{\partial \mathbf{x}} \right|_{\mathbf{x}=\mathbf{x}^{eq}} = 0$. The approximate potential (ignoring the zero-point energy) is

$$V(\mathbf{x}) \approx \frac{1}{2} \sum_{n,m} K_{nm} (x_n - x_n^{eq})(x_m - x_m^{eq}), \quad (3.14)$$

with $K_{nm} = \left. \frac{\partial^2 V(\mathbf{x})}{\partial x_n \partial x_m} \right|_{\mathbf{x}=\mathbf{x}^{eq}}$ being the Hessian matrix entries of $V(\mathbf{x})$ around the equilibrium configuration [98]

$$K_{nm} = \begin{cases} m\omega_n^2 + 2 \left(\frac{q^2}{4\pi\epsilon_0} \right) \sum_{l \neq n} \frac{1}{|x_n^{eq} - x_l^{eq}|^3} & \text{if } n = m \\ -2 \left(\frac{q^2}{4\pi\epsilon_0} \right) \frac{1}{|x_n^{eq} - x_m^{eq}|^3} & \text{if } n \neq m \end{cases}. \quad (3.15)$$

Note that this approximation does not modify the two main features of the system, namely asymmetry and long-range interactions, which are manifest in the asymmetric distribution of ω_n and the non-zero off-diagonal elements of the K matrix, respectively. In the following we will use $y_n = x_n - x_n^{eq}$ to simplify the notation. The linearized dynamics around the equilibrium positions are given by

$$\begin{aligned} \dot{y}_n &= \frac{1}{m} p_n, \\ \dot{p}_n &= - \sum_l K_{nl} y_l - \frac{\gamma_n}{m} p_n + \xi_n(t). \end{aligned} \quad (3.16)$$

Now, we set $d\langle \dots \rangle/dt = 0$ for all the moments. Using Eq. (3.16) and applying Novikov's theorem we find

$$\begin{aligned} \langle p_n p_l \rangle - \gamma_l \langle y_n p_l \rangle - \sum_m K_{lm} \langle y_n y_m \rangle &= 0, \\ \sum_m [K_{nm} \langle y_m p_l \rangle + K_{lm} \langle y_m p_n \rangle] + \frac{1}{m} (\gamma_l + \gamma_n) \langle p_n p_l \rangle &= 2\delta_{nl} D_n. \end{aligned} \quad (3.17)$$

The system (3.17) is linear in the second order moments so it can be solved numerically to find the steady-state values of the moments. Besides Eq. (3.17) we have that $\langle y_n p_l \rangle = -\langle y_l p_n \rangle$, which follows from Eq. (3.16) and $d\langle y_n y_m \rangle / dt = 0$. Since there are $\frac{1}{2}N(N-1)$ independent $\langle y_n p_l \rangle$ moments, we choose the ones with $n < l$. Similarly, the moments $\langle y_n y_l \rangle$ and $\langle p_n p_l \rangle$ contribute with $\frac{1}{2}N(N+1)$ independent variables each and we choose the ones with $n \leq m$. Thus there are in total $\frac{1}{2}N(3N+1)$ independent moments that we arrange in the vector

$$\boldsymbol{\eta} = \begin{bmatrix} \langle y_1 y_1 \rangle, \langle y_1 y_2 \rangle, \dots, \langle y_N y_N \rangle, \\ \langle p_1 p_1 \rangle, \langle p_1 p_2 \rangle, \dots, \langle p_N p_N \rangle, \\ \langle y_1 p_2 \rangle, \langle y_1 p_3 \rangle, \dots, \langle y_{N-1} p_N \rangle \end{bmatrix}^T. \quad (3.18)$$

There are the same number of independent equations as independent moments: N^2 equations correspond to the first line in Eq. (3.17), and $\frac{1}{2}N(N+1)$ equations to the second line because of the symmetry with respect to n, l . The system of equations (3.17) may be compactly written as $\mathbf{A}\boldsymbol{\eta} = \mathbf{B}$, where \mathbf{A} and \mathbf{B} are a $\frac{1}{2}N(3N+1)$ square matrix and vector.

3.4 Numerical Results

We now display the results of our simulations. To find the temperature profiles and the currents in the steady state we use the algebraic method described in section 3.3.1. We also check that the results coincide with those by solving Eq. (3.3) for many different realizations of the noisy forces $\boldsymbol{\xi}(t)$ and averaging. The code for all the numerical simulations has been written in the language *Julia* [99, 100]. In particular, to solve the Langevin equation, we used *Julia*'s package *DifferentialEquations.jl* [101].

To model the baths and the chain we use atomic data taken from ion trap experiments [102, 103]. We consider 15 $^{24}\text{Mg}^+$ ions in all figures except in Fig. 3.6. The three leftmost and three rightmost ions are illuminated by Doppler cooling lasers. The Doppler cooling lasers excite the transition $3s^2S_{1/2} \rightarrow 3p^2P_{1/2}$, with angular frequency $\omega_0 = 2\pi \times 1069$ THz and excited state line width $\Gamma = 2\pi \times 41.3$ MHz [81]. For this ionic species and atomic transition the Doppler limit is $T_D = 1$ mK. The intensities of the laser beams are small compared to the saturation

intensity I_0 so that Eq. (3.4) holds. We take $I_n/I_0 = 0.08$ for the ions in the laser beams, whereas $I_n = 0$ for the rest.

The temperatures T_L, T_R of the left and right laser baths are controlled with their detunings δ_L, δ_R with respect to the atomic transition. We fix two values for the detunings, δ_H and δ_C , such that $T_H > T_C$ (hot and cold baths, also source and drain) and we define J_{\rightarrow} (J_{\leftarrow}) as the stationary heat current in the chain when $T_L = T_H$ and $T_R = T_C$ ($T_L = T_C$ and $T_R = T_H$).

Except in Sec. 3.4.5 we consider a graded frequency profile. If the frequency of the leftmost trap is ω_1 , the frequency of the n th trap will be $\omega_n = \omega_1 + \Delta\omega \frac{n-1}{N-1}$ up to $\omega_1 + \Delta\omega$ for the rightmost trap. In Sec. 3.4.5 we compare the graded chain to a segmented chain, where the left half of the chain has trapping frequencies ω_1 while the other half has $\omega_1 + \Delta\omega$.

3.4.1 Evolution to steady state

To compare the results by solving Eq. (3.3) and averaging and those from the algebraic method we simulated a frequency graded chain with a trapping frequency $\omega_1 = 2\pi \times 50$ kHz for the leftmost ion, see Fig. 3.2. The number of ions interacting with the laser beams (three on each bath) is consistent with the lattice constant and typical waists of Gaussian laser beams [102, 103]. To set the trap distance we fix first the characteristic length $l = \left(\frac{q^2}{4\pi\epsilon_0} \frac{1}{m\omega_1^2}\right)^{1/3}$ as the distance for which the Coulomb repulsion of two ions equals the trap potential energy for an ion at a distance l away from the center of its trap. If $a < l$, the Coulomb repulsion of the ions is stronger than the trap confinement which makes the ions jump from their traps. With the parameters used in this section we have $l = 38.7 \mu\text{m}$ and set $a = 1.29l = 50 \mu\text{m}$. The detunings of the *hot* and *cold* lasers are $\delta_H = -0.02\Gamma$, and $\delta_C = -0.1\Gamma$ which gives temperatures $T_H \approx 12$ mK and $T_C \approx 3$ mK. We fix the value $\Delta\omega = 0.5\omega_1$ for the frequency increment.

The results of the two methods are in very good agreement. In the scale of Fig. 3.2 (a) the calculated local temperatures are undistinguishable. In the calculation based on solving the dynamics we had to integrate Eq. (3.3) for $N_{\text{trials}} = 1000$ realizations of white noise $\xi(t)$. The method based on the system of moments shortened the calculation time with respect to the dynamical trajectories by a factor of 1/700. In fact, the time gain is even more important because the dynamical

method requires further processing, performing a time averaging to compute the stationary flux in addition to noise averaging, see Fig. 3.2 (b).

Additionally, the relaxation to the steady state slows down when the frequencies of the traps increase since the deterministic part of the Langevin equation dominates the dynamics over the stochastic part, entering an under-damped regime. In contrast, this increase does not affect the algebraic method.

3.4.2 Rectification in frequency graded chains

In this subsection we demonstrate rectification for the frequency graded chain. We used the method described in section 3.3.1 for $^{24}\text{Mg}^+$ ions with the same parameters for the baths used before. We fix the trapping frequency of the leftmost trap to $\omega_1 = 2\pi \times 1$ MHz, and a trap spacing $a = 4.76 l$ ($25 \mu\text{m}$) (the characteristic length is $l = 5.25 \mu\text{m}$). Figure 3.3 depicts the results with these parameters in a graded chain. Figure 3.3 (a) shows that both J_{\rightarrow} and J_{\leftarrow} decrease rapidly as the frequency increment is increased. The rectification reaches its maximum value for a frequency difference of $\Delta\omega \approx 0.1\omega_1$. The fluxes cross so there are some points where the rectification is exactly zero, besides the trivial one at $\Delta\omega = 0$, at $\Delta\omega = 0.05\omega_1$, $0.3\omega_1$, $1.3\omega_1$. At these points the direction of rectification reverses, presumably as a consequence of the changes in the match/mismatch of the temperature dependent local power spectra. The change of rectification direction occurs for all the choices of parameters, as displayed in Fig. 3.4. Figure 3.4 gives the rectification factor for different trap distances and frequency increments. 0-rectification curves separate regions with different rectification direction. The second region in Fig. 3.4 (starting from the left) would be the most interesting one to build a thermal diode, since rectification reaches its largest values there.

For small values of $\Delta\omega$ there is little asymmetry in the chain and therefore modest rectification is expected whereas a very large $\Delta\omega$ implies very high trapping frequencies on the right implying too strong a confinement and vanishing interactions. This bottleneck decreases the fluxes in both directions and the rectification. However, since $\Delta\omega$ is controllable, and the range of values of $\Delta\omega$ for which rectification is larger can be also controlled with the intertrap distance a , see Fig. 3.4, the existence of a rectification window does not imply a major limitation.

3.4.3 Same bath temperatures, different bath couplings

As already mentioned below Eq. (3.5), above and below the detuning $\delta_D = -\Gamma/2$ corresponding to the Doppler limit temperature, the optical molasses allow for two different couplings (two pairs of friction and diffusion coefficients in Eq. (3.4)) between the ions and the laser corresponding to the same bath temperature. This duality may be seen explicitly in Fig. 3.5. Specifically Fig. 3.5 (a) depicts the variation of the friction coefficient for values of δ around δ_R , and Fig. 3.5 (b) the corresponding temperatures. Interestingly, the different couplings imply different rectification factors. If we set $\delta_C = \delta_D = -\Gamma/2$, i.e., the cold bath is cooled to the Doppler limit, δ_H can be chosen to be below or above δ_D for the same temperature T_H . The corresponding rectification factors for the two choices are shown in Fig. 3.5 (c), which demonstrates that significant rectification can be achieved by choosing $\delta_H < \delta_D$ for temperature increments that are smaller than or of the order of $T_C = T_D$, for example $R \approx 20\%$ for $\Delta T = 0.1T_C$, or $R \approx 60\%$ for $\Delta T = T_C$. Finding good rectification at low (relative) temperature differences is considered to be one of the challenges in asymmetric heat transport research [104].

3.4.4 Dependence with ion number

Keeping in mind that scaling the frequency-graded ion chain to a large number of ions is not a realistic option in this setting, it is nevertheless important to study the dependence with ion number from small to moderate numbers. In Fig. 3.6 we observe an overall trend in which the rectification decreases with the number of ions in the chain (while it increases with temperature bias ΔT in the studied range). This effect is easy to understand, as increasing N while keeping the total variation of the trapping frequency $\Delta\omega$ constant, the frequency gradient decreases. This lowers the asymmetry in the chain and the rectification factor. Oscillations with N superimposed to the global trend are more visible at the smaller N values giving an optimal N value at $N = 19$.

3.4.5 Graded versus segmented

We have also compared the performance of the graded thermal diode and a segmented version in which the left half of the chain is trapped with frequency ω_1 and the right half (including the middle ion) with $\omega_1 + \Delta\omega$. Even though the optimal rectification in Fig. 3.7 (a) for the segmented chain is larger than for the graded chain, the fact that the fluxes are generally much larger for the graded chain, see Fig. 3.7 (b), makes the graded chain more interesting for applications.

3.5 Summary and discussion

In this article we have numerically demonstrated heat rectification in a chain of ions trapped in individual microtraps with graded frequencies, connected at both ends to thermal baths created by optical molasses. An alternative to implement a graded frequency profile in the lab could be combining a collective Paul trap for all the ions with on-site dipolar laser forces [80, 105–107].

A goal of this article is to connect two communities, ion trappers and researchers on heat-rectification models. The results found are encouraging and demonstrate the potential of a trapped-ion platform to experimentally investigate heat rectification schemes. Trapped ions are quite interesting to this end because they are highly controllable, and may easily adopt several features to enhance rectification, such as the ones explored here (long-range interactions and an asymmetrical gradation), or others such as time dependent forces [32, 108], or different nonlinearities in onsite forces. The limitations and application domain should also be clear, the proposed platform is circumscribed to cold temperatures of the order of hundreds of μK to mK achieved by Doppler cooling. In this sense it is not aimed at competing with (it is rather complementary to) proposals for which experiments [43, 66–68] or simulations [104, 109, 110] demonstrate thermal rectification at room temperature or for hundreds of K. Also, the number of ions should realistically be kept small so the proposed ion chain is not aimed at achieving a macroscopic diode length, but at playing a role in thermal diode research and in the context of ion-trapped based quantum technologies.

Methodologically, the calculation of the steady state has been performed with an algebraic approach much faster than the time-consuming integration and averaging over noise and time of the dynamical equations. The algebraic approach linearizes the forces around equilibrium positions which, in this system and for the realistic parameters considered is well justified and tested numerically. The results found provide additional evidence that simple linear models may rectify heat flow [34]. We underline that our linear model is, arguably, even simpler than some linear “minimalist, toy models” in [34] that showed rectification (our on-site forces are already linear from the start and the temperature dependence of explicit model parameters is only in the coefficients of the Langevin baths), with the important bonus of being also realistic.

To shed some more light on the mechanism behind the observed rectification we may analyze the local thermal conductivities $\lambda[x, T(x)]$ defined in a continuous model by [39]

$$J = \lambda[x, T(x)] \left| \frac{dT(x)}{dx} \right|, \quad (3.19)$$

where J is the stationary heat current and $T(x)$ the local temperature. (We use the modulus of the temperature derivative for consistency with our (positive) definition of J .) In our model we discretize the coordinate with the ion index and the temperature derivative is discretized as

$$\frac{dT_n}{dx} = \frac{T_{n+1} - T_{n-1}}{x_{n+1}^{eq} - x_{n-1}^{eq}}. \quad (3.20)$$

Through integration, it is clear that when λ depends on both temperature and position rectification is possible. In the continuous model the temperature increment between the baths is

$$|T_L - T_R| = \int_0^L \frac{J}{\lambda[x, T(x)]} dx \quad (3.21)$$

so that the key for rectification is a different integral of the inverse of the conductivities in the two scenarios ($T_L = T_H, T_R = T_C$ with conductivity $\lambda_{\rightarrow}[x, T_{\rightarrow}(x)]$ along a local temperature decreasing from the left or the reversed one, $T_R = T_H, T_L = T_C$ with conductivity $\lambda_{\leftarrow}[x, T_{\leftarrow}(x)]$ along an increasing local temperature. Particularly favorable for rectification is the scenario where one of the lambdas is above the other one for all x . Figure 3.8 shows that this is essentially the case in our model, at least along the most relevant part of the integral.

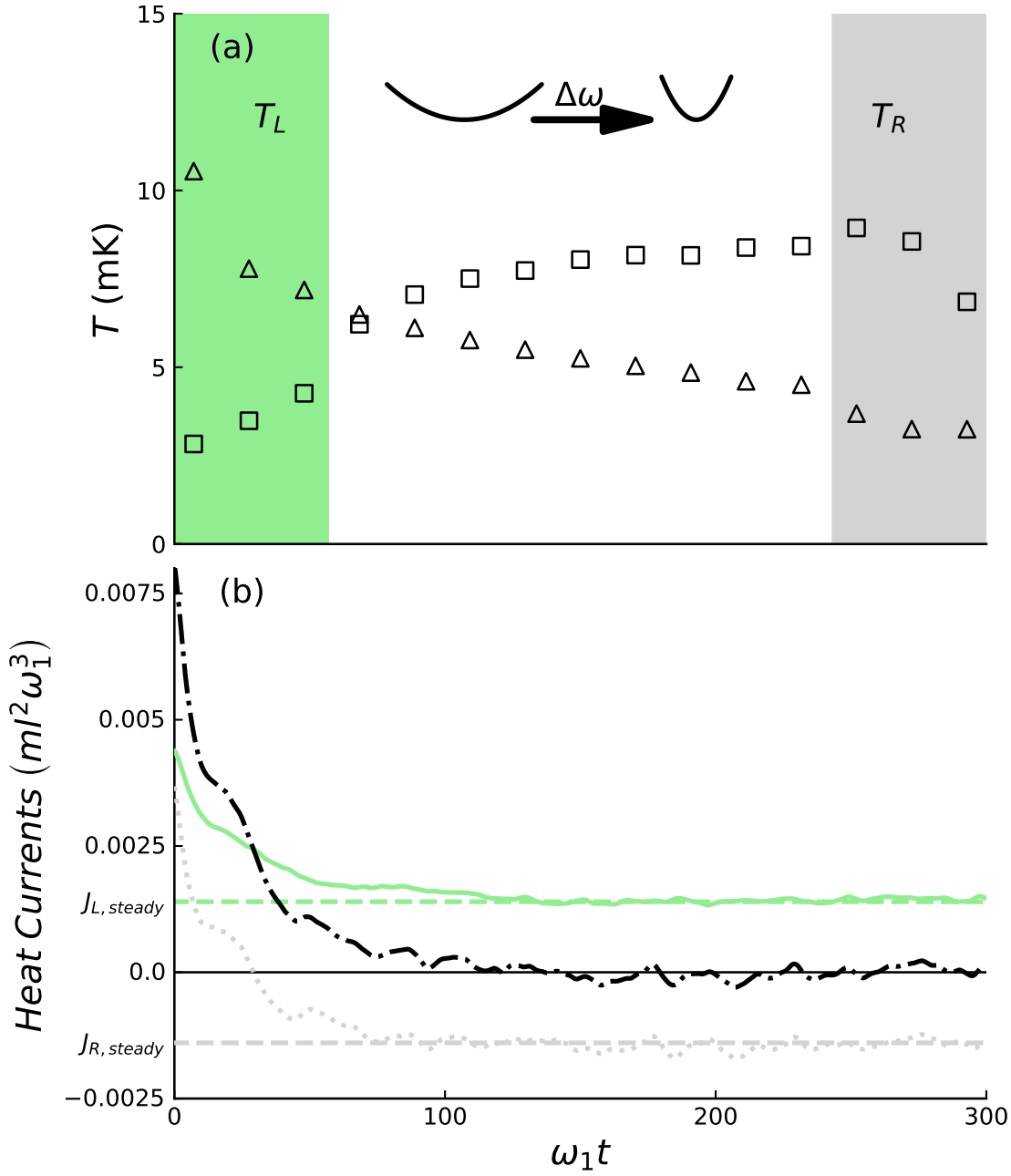


FIGURE 3.2: (a) Temperatures of the ions in the stationary state for a graded chain with the parameters described in section 3.4.1. The temperature profiles found with the algebraic method (Eq. (3.17)) are indistinguishable from the ones found solving the Langevin equation (Eq. (3.3)). Empty triangles (squares) correspond to $T_L = T_H$ ($T_L = T_C$) and $T_R = T_C$ ($T_R = T_H$). (b) Heat currents as a function of time for $T_L = T_H$ and $T_R = T_C$, see Eq. (3.9): $J_L(t)$ (solid green line) from the left reservoir into the chain; $J_R(t)$ (dotted grey line) from the right reservoir into the chain (negative except at very short times); $J_L(t) + J_R(t)$ (dotted-dashed black line), which must go to zero in the steady state. The three lines tend to stationary values marked by horizontal lines. Parameters: $\omega_1 = 2\pi \times 50$ kHz, $a = 50 \mu\text{m}$, $\delta_H = -0.02 \Gamma$, and $\delta_C = -0.1 \Gamma$, which gives temperatures $T_H \approx 12$ mK and $T_C \approx 3$ mK. $\Delta\omega = 0.5\omega_1$. In all figures $\Gamma = 2\pi \times 41.3$ MHz.

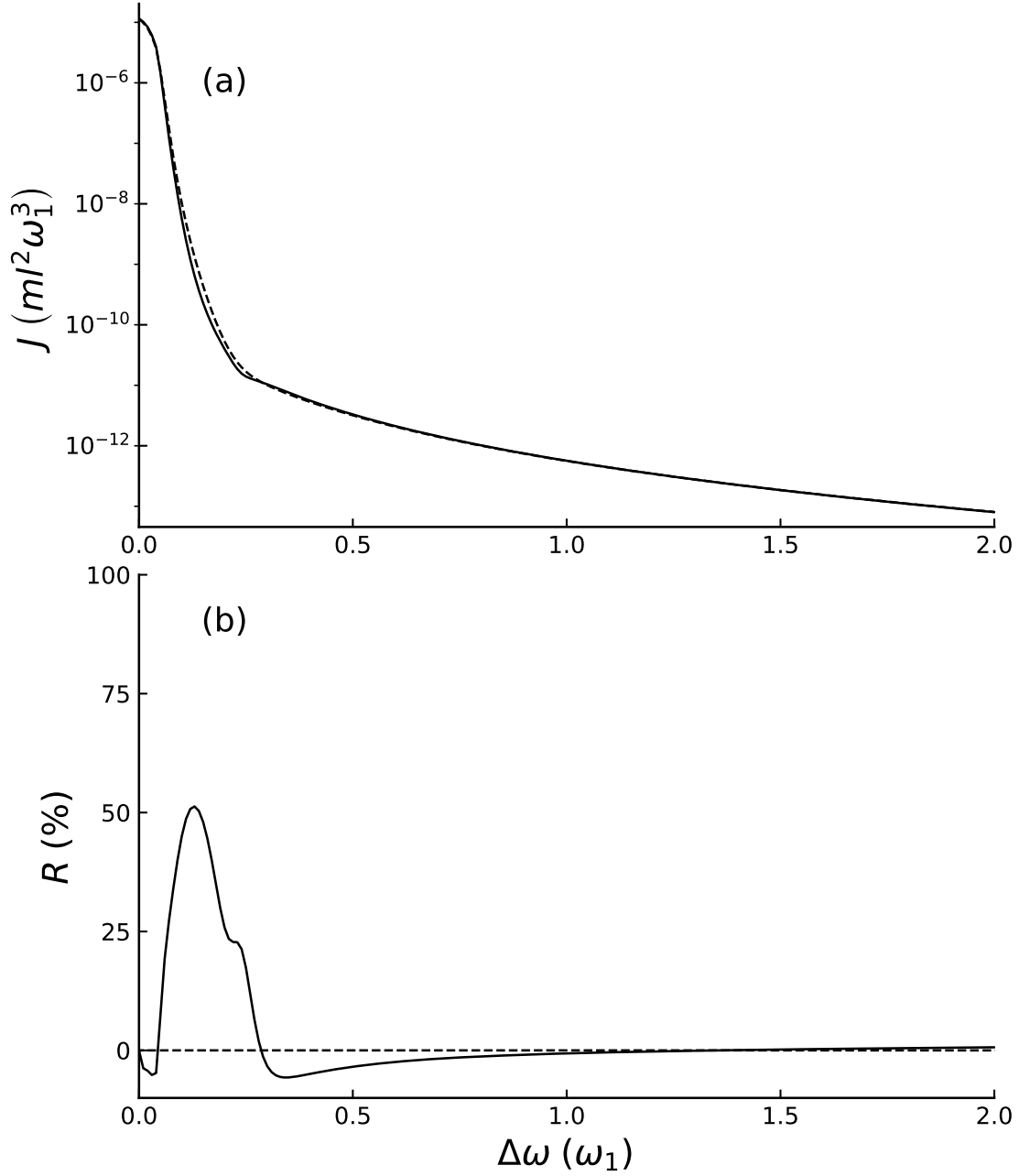


FIGURE 3.3: Graded chain of $N = 15$ $^{24}\text{Mg}^+$ ions. (a) Stationary fluxes for different frequency increments: J_{\rightarrow} (for $T_L = T_H$ and $T_R = T_C$, dashed line); J_{\leftarrow} (for $T_L = T_C$ and $T_R = T_H$, solid line) (b) Rectification factor. Parameters: $\omega_1 = 2\pi \times 1$ MHz, $l = 5.25 \mu\text{m}$, $a = 4.76 l$ ($25 \mu\text{m}$), $\delta_H = -0.02 \Gamma$, and $\delta_C = -0.1 \Gamma$.

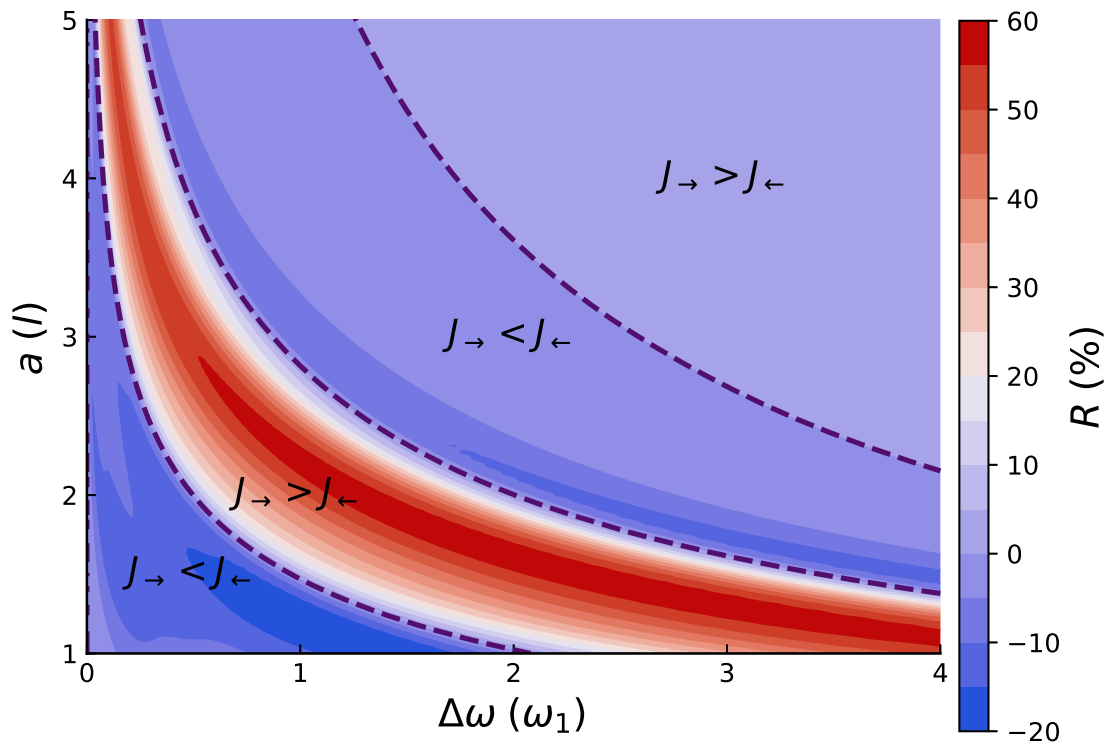


FIGURE 3.4: Rectification factor in a graded chain of $N = 15$ $^{24}\text{Mg}^+$ ions for different trap distances and frequency increment. The dashed lines are for $R = 0$ and delimit the regions $J_{\rightarrow} > J_{\leftarrow}$ and $J_{\rightarrow} < J_{\leftarrow}$. The parameters are $\omega_1 = 2\pi \times 1$ MHz, $l = 5.25 \mu\text{m}$, $\delta_H = -0.02 \Gamma$, and $\delta_C = -0.1 \Gamma$.

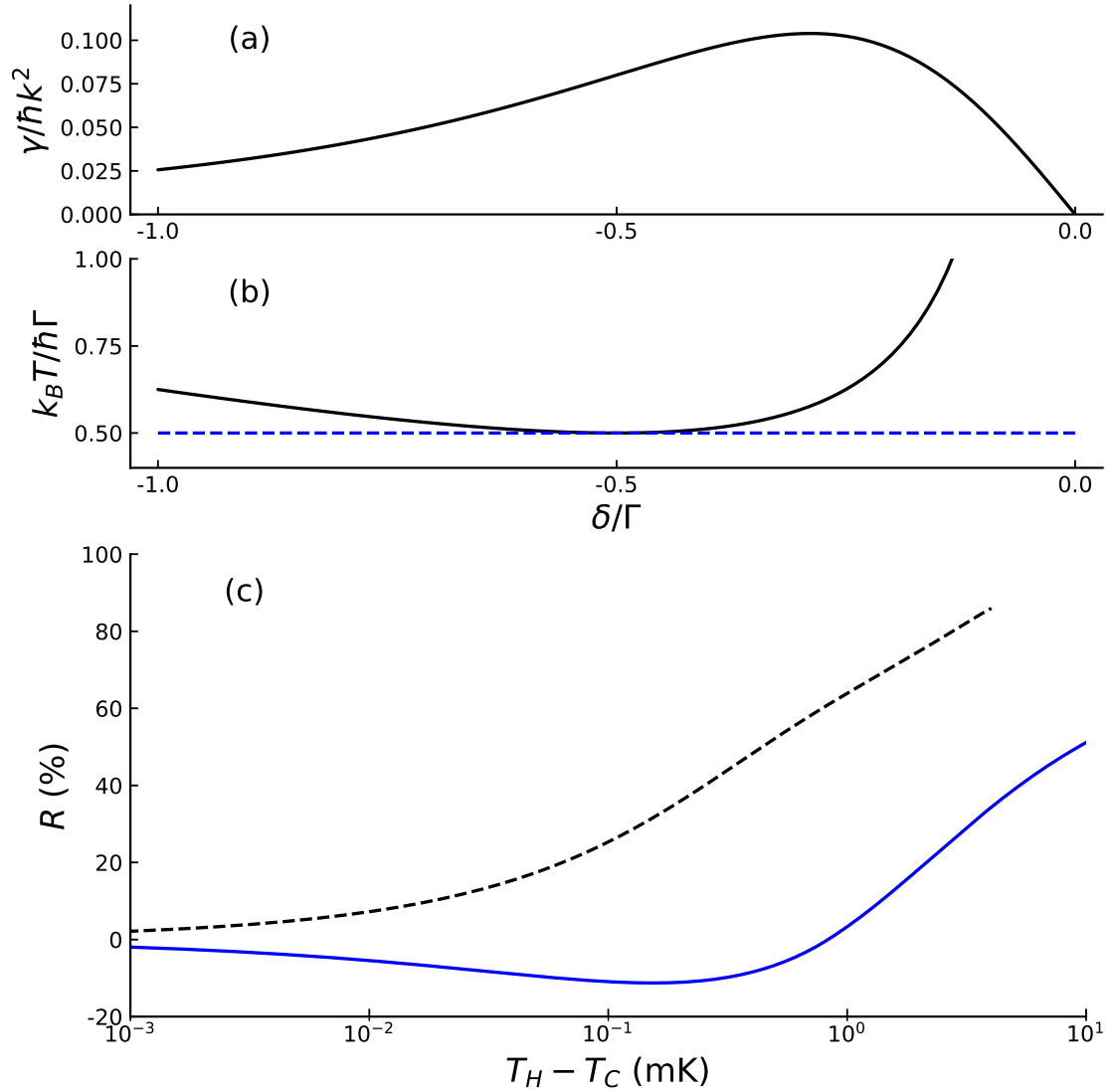


FIGURE 3.5: (a) Friction coefficient defined in Eq. (3.4). (b) Bath temperature defined in Eq. (3.5). (c) Rectification as a function of the temperature difference between the hot and cold baths $T_H - T_C$ for δ_H below (dashed black line) and above (solid blue line) the Doppler limit, and $\delta_C = \delta_D$ (Doppler limit).

Parameters: $\omega_1 = 2\pi \times 1$ MHz, $\Delta\omega = 0.15 \omega_1$, $l = 5.25 \mu\text{m}$, $a = 4.76 l$.

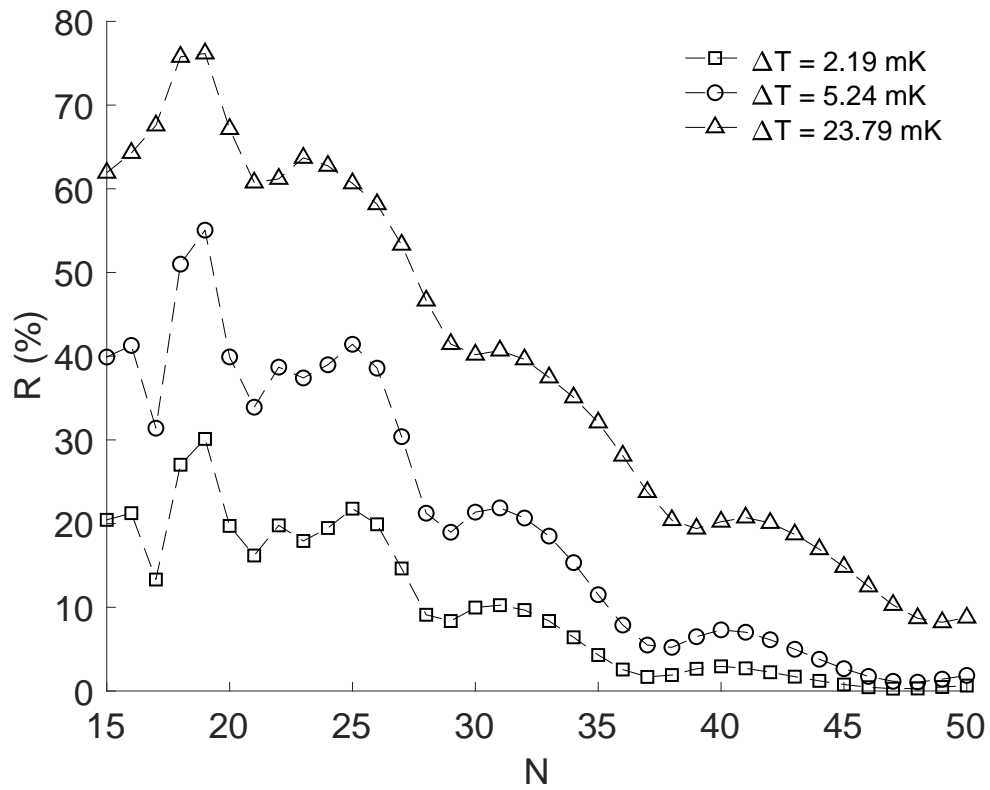


FIGURE 3.6: Rectification factor for different bath temperature differences ΔT as the number of ions is increased. The detuning of the cold bath laser is set to the Doppler limit $\delta_C = -\Gamma/2$. $\omega_1 = 2\pi \times 1$ MHz, $\Delta\omega = 0.15\omega_1$, $l = 5.25\ \mu\text{m}$, $a = 4.76\ l$.

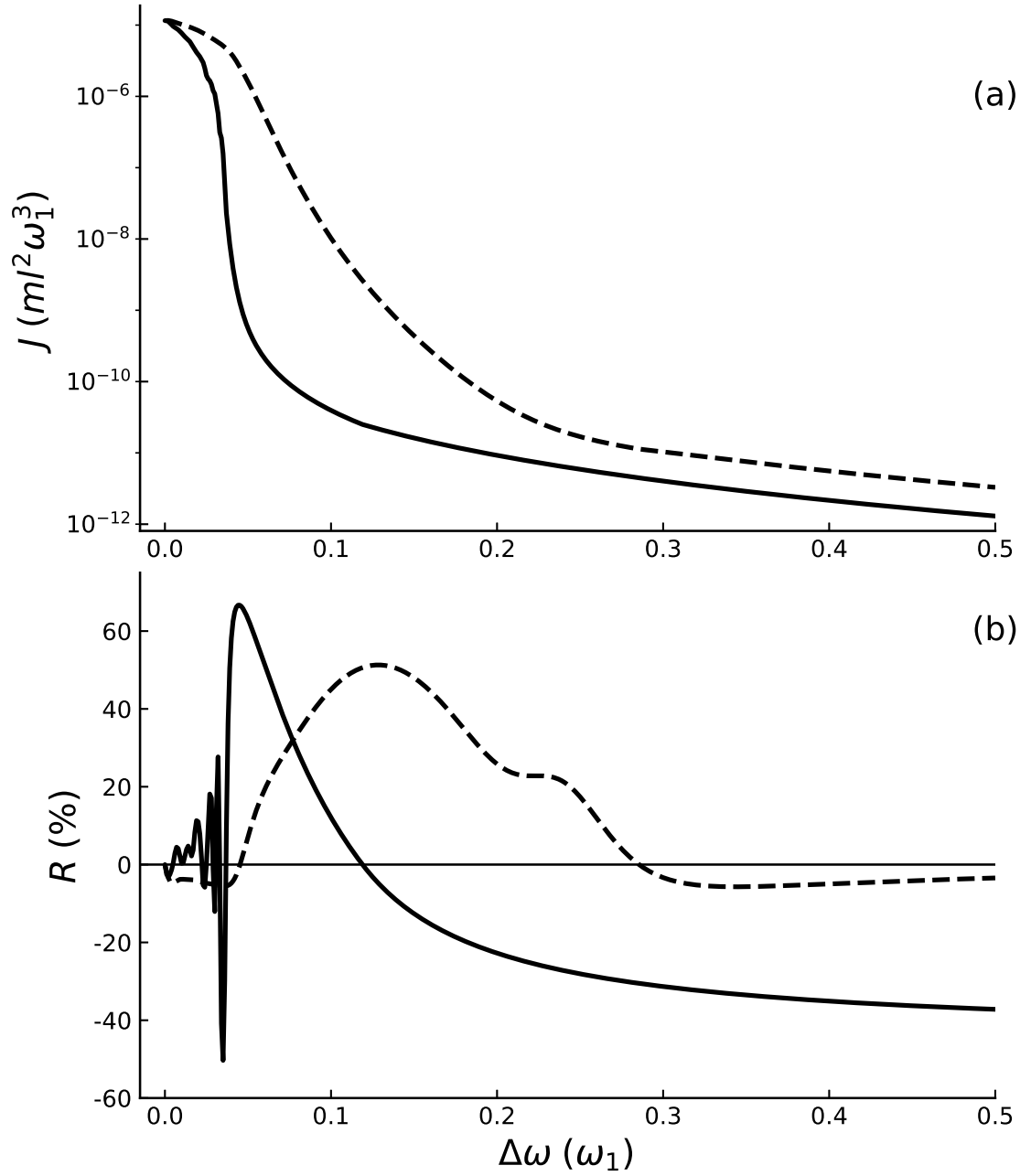


FIGURE 3.7: Comparison of graded and segmented chains with $N = 15$ $^{24}\text{Mg}^+$ ions. (a) Maximum of J_{\rightarrow} and J_{\leftarrow} for the graded and segmented chain for different frequency increments. (b) Rectification factor: graded chain (dashed lines); segmented chain (solid lines). Parameters: $\omega_1 = 2\pi \times 1$ MHz, $l = 5.25 \mu\text{m}$, $a = 4.76 l$, $\delta_H = -0.02 \Gamma$, and $\delta_C = -0.1 \Gamma$.

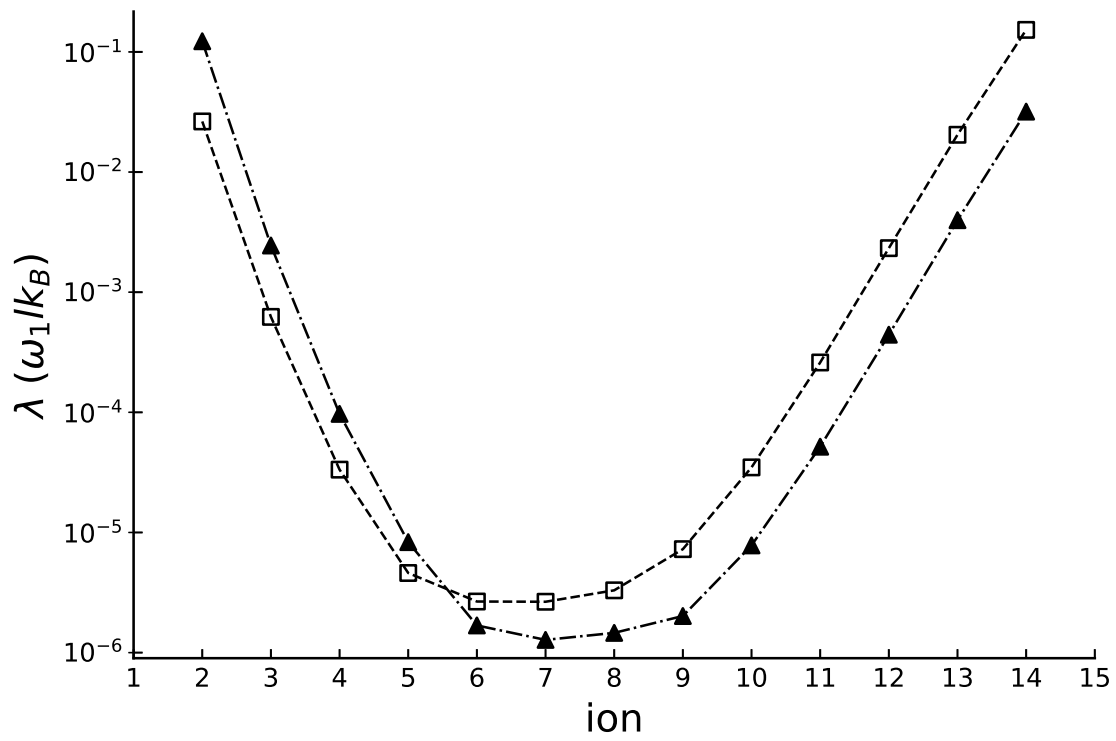


FIGURE 3.8: Thermal conductivity through the chain for $T_L > T_R$ (empty squares), and $T_L < T_R$ (filled triangles). $\omega_1 = 2\pi \times 1$ MHz, $\Delta\omega = 0.15\omega_1$, $l = 5.25 \mu\text{m}$, $a = 4.76l$, $\delta_H = -0.02\Gamma$ and $\delta_C = -0.1\Gamma$.

Chapter 4

Rectification in a toy model

We study heat rectification in a minimalistic model composed of two masses subjected to on-site and coupling linear forces in contact with effective Langevin baths induced by laser interactions. Analytic expressions of the heat currents in the steady state are spelled out. Asymmetric heat transport is found in this linear system if both the bath temperatures and the temperature dependent bath-system couplings are also exchanged.

4.1 Introduction

Heat rectification, firstly observed in 1936 by Starr [60], is the physical phenomenon, analogous to electrical current rectification in diodes, in which heat current through a device or medium is not symmetric with respect to the exchange of the baths at the boundaries. In the limiting case the device allows heat to propagate in one direction from the hot to the cold bath while it behaves as a thermal insulator in the opposite direction when the baths are exchanged. In 2002 a paper by Terraneo *et al.* [30] demonstrated heat rectification numerically for a chain of nonlinear oscillators in contact with two thermal baths at different temperatures. Since then, there has been a growing interest in heat rectification [31, 32, 43, 47, 61–68, 70, 111], and the field remains very active because of the potential applications in fundamental science and technology, and the fact that none of the proposals so far appears to be efficient and robust for practical purposes.

Much effort has been devoted to understand the underlying physical mechanism responsible for rectification [61]. In early times some kind of anharmonicity, i.e. non-linear forces, in the substrate potential or in the particle-particle interactions, was identified as a fundamental requisite for rectification [32, 38, 40, 42, 48, 69]. This non-harmonic behavior leads to a temperature dependence of the phonon bands. The match/mismatch of the phonon bands (power spectra) governs the heat transport in the chain, allowing it when the bands match or obstructing it if they mismatch [30, 37]. However, a work by Pereira *et al.* [34] showed that rectification can also be found in effective harmonic systems if two requirements are met: some kind of structural asymmetry, and features that depend on the temperature so they change as the baths are inverted. Indeed, in this article we demonstrate rectification in a minimalistic model of two harmonic oscillators where the coupling to the baths depends on the temperature. This will be justified with a particular physical set up with trapped ions and lasers.

The article is organized as follows. In Section 4.2 we describe the physical model and its dynamical equations. In Section 4.3 we describe the dynamics of the system in terms of a covariance matrix. We also derive a set of algebraic equations that gives as solution the covariance matrix in the steady state. In Section 4.4 we solve the covariance matrix equations and find analytical expressions for the steady-state temperatures of the masses and heat currents. In Section 4.5 we relate the parameters of our model to those in a physical set-up of Doppler cooled trapped

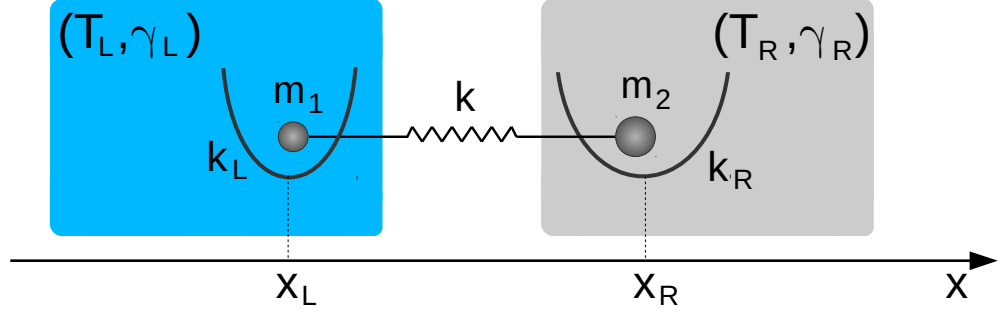


FIGURE 4.1: Diagram of the model described in Section 4.2. Two ions coupled to each other through a spring constant k . Each ion is harmonically trapped and connected to a bath characterized by its temperature T_i and its friction coefficient γ_i .

ions. In Section 4.6 we make a parameter sweep looking for configurations which yield high rectification. We also study the power spectra of the oscillators, which confirm the match/mismatch patterns in cases where there is rectification. In Section 4.7 we summarize our results and present our conclusions.

4.2 Physical Model

The physical model consists of two masses m_1 and m_2 coupled to each other by a harmonic interaction with spring constant k and natural length x_e . Each of the masses m_1 and m_2 are confined by a harmonic potential with spring constants k_L , k_R and equilibrium positions x_L , x_R respectively (see Fig. 4.1). The Hamiltonian describing this model is

$$H = \frac{p_1^2}{2m_1} + \frac{p_2^2}{2m_2} + V(x_1, x_2), \quad (4.1)$$

with $V(x_1, x_2) = \frac{k}{2}(x_1 - x_2 - x_e)^2 + \frac{k_L}{2}(x_1 - x_L)^2 + \frac{k_R}{2}(x_2 - x_R)^2$, where $\{x_i, p_i\}_{i=1,2}$ are the position and momentum of each mass. Switching from the original coordinates x_i to displacements with respect to the equilibrium positions of the system $q_i = x_i - x_i^{eq}$, where x_i^{eq} are the solutions to $\partial_{x_i} V(x_1, x_2) = 0$, the Hamiltonian can

be written as

$$H = \frac{p_1^2}{2m_1} + \frac{p_2^2}{2m_2} + \frac{k + k_L}{2} q_1^2 + \frac{k + k_R}{2} q_2^2 - k q_1 q_2 + V(x_1^{eq}, x_2^{eq}). \quad (4.2)$$

This has the form of the Hamiltonian of a system around a stable equilibrium point

$$H = \frac{1}{2} \vec{p}^\top \mathbb{M}^{-1} \vec{p} + \frac{1}{2} \vec{q}^\top \mathbb{K} \vec{q}, \quad (4.3)$$

where $\vec{q} = (q_1, q_2)^\top$, $\vec{p} = (p_1, p_2)^\top$, $\mathbb{M} = \text{diag}(m_1, m_2)$ is the mass matrix of the system and \mathbb{K} is the Hessian matrix of the potential at the equilibrium point, i.e., $\mathbb{K}_{ij} = \partial_{x_i, x_j}^2 V(\vec{x}) \Big|_{\vec{x}=\vec{x}^{eq}}$. In this model $\mathbb{K}_{11} = k + k_L$, $\mathbb{K}_{22} = k + k_R$ and $\mathbb{K}_{12} = \mathbb{K}_{21} = -k$. We shall see later that the generic form (4.3) can be adapted to different physical settings, in particular to two ions in individual traps, or to two ions in a common trap.

The masses are in contact with Langevin baths, which will be denoted as L (for left) and R (for right), at temperatures T_L and T_R for the mass m_1 and m_2 respectively (see Fig. 4.1). The equations of motion of the system, taking into account the Hamiltonian and the Langevin baths are

$$\begin{aligned} \dot{q}_1 &= \frac{p_1}{m_1}, \\ \dot{q}_2 &= \frac{p_2}{m_2}, \\ \dot{p}_1 &= -(k + k_L)q_1 + kq_2 - \frac{\gamma_L}{m_1} p_1 + \xi_L(t), \\ \dot{p}_2 &= -(k + k_R)q_2 + kq_1 - \frac{\gamma_R}{m_2} p_2 + \xi_R(t), \end{aligned} \quad (4.4)$$

where γ_L, γ_R are the friction coefficients of the baths and $\xi_L(t), \xi_R(t)$ are Gaussian white-noise-like forces. The Gaussian forces have zero mean ($\langle \xi_L(t) \rangle = \langle \xi_R(t) \rangle = 0$) and satisfy the correlations $\langle \xi_L(t) \xi_R(t') \rangle = 0$, $\langle \xi_L(t) \xi_L(t') \rangle = 2D_L \delta(t - t')$, $\langle \xi_R(t) \xi_R(t') \rangle = 2D_R \delta(t - t')$. D_L and D_R are the diffusion coefficients, which satisfy the fluctuation-dissipation theorem: $D_L = \gamma_L k_B T_L$, $D_R = \gamma_R k_B T_R$ (k_B is the Boltzmann constant).

It is useful to define the phase-space vector $\vec{r}(t) = (\vec{q}, \mathbb{M}^{-1} \vec{p})^\top$ (note that $\vec{v} = \mathbb{M}^{-1} \vec{p}$ is just the velocity vector) so the equations of motion for this vector

are

$$\dot{\vec{r}}(t) = \mathbb{A} \vec{r}(t) + \mathbb{L} \vec{\xi}(t), \quad (4.5)$$

with

$$\begin{aligned} \mathbb{A} &= \begin{pmatrix} \mathbb{K}_{2 \times 2} & \mathbb{K}_{2 \times 2} \\ -\mathbb{M}^{-1}\mathbb{K} & -\mathbb{M}^{-1}\Gamma \end{pmatrix}, \\ \mathbb{L} &= \begin{pmatrix} \mathbb{K}_{2 \times 2} \\ \mathbb{M}^{-1} \end{pmatrix}, \end{aligned} \quad (4.6)$$

and $\vec{\xi}(t) = (\xi_L(t), \xi_R(t))^\top$, $\Gamma = \text{diag}(\gamma_L, \gamma_R)$. $\mathbb{K}_{n \times n}$ and $\mathbb{I}_{n \times n}$ are the n -th dimensional squared 0 matrix and identity matrix respectively. With the vector notation the correlation of the white-noise forces can be written as

$$\langle \vec{\xi}(t) \vec{\xi}(t')^\top \rangle = 2\mathbb{D}\delta(t - t'), \quad (4.7)$$

with $\mathbb{D} = \text{diag}(D_L, D_R)$.

4.3 Covariance matrix in the steady state

We define the covariance matrix of the system as $\mathbb{C}(t) = \langle \vec{r}(t) \vec{r}(t)^\top \rangle$. This matrix is important because the heat transport properties can be extracted from it. In particular, the kinetic temperatures of the masses, $T_1(t)$ and $T_2(t)$, are

$$\begin{aligned} T_1(t) &= \frac{\langle p_1^2(t) \rangle}{m_1 k_B} = \frac{m_1 C_{3,3}(t)}{k_B}, \\ T_2(t) &= \frac{\langle p_2^2(t) \rangle}{m_2 k_B} = \frac{m_2 C_{4,4}(t)}{k_B}. \end{aligned} \quad (4.8)$$

One approach to find the covariance matrix is to solve Eq. (4.5). However, this requires solving the equations explicitly or simulate them numerically many times to find the covariance matrix for the ensemble of simulated stochastic trajectories. Instead, we proceed by looking for an ordinary differential equation that gives the evolution of the covariance matrix as described in [97, 112, 113]. Differentiating

$\mathbb{C}(t)$ with respect to time and using Eq. (4.5) we get

$$\begin{aligned} \frac{d}{dt}\mathbb{C}(t) &= \mathbb{A}\mathbb{C}(t) + \mathbb{C}(t)\mathbb{A}^\top \\ &\quad + \mathbb{L} \left\langle \vec{\xi}(t) \vec{r}(t)^\top \right\rangle \\ &\quad + \left\langle \vec{r}(t) \vec{\xi}(t)^\top \right\rangle \mathbb{L}^\top. \end{aligned} \quad (4.9)$$

The solution of Eq. (4.9) allows us to find the local temperatures of the masses as a function of the bath temperatures (Eq. (4.8)) at all times. In particular, we are interested in the covariance matrix in the steady state, i.e., for $t \rightarrow \infty$. According to the Novikov Theorem [93] we can write down the covariance matrix in the steady state without having to integrate the differential equation. We now show how to get the steady-state covariance matrix.

In the steady state, the covariance matrix is constant ($\frac{d}{dt}\mathbb{C}(t) = 0$), therefore it satisfies

$$\begin{aligned} \mathbb{A}\mathbb{C}^{s.s.} + \mathbb{C}^{s.s.}\mathbb{A}^\top &= \\ -\mathbb{L} \left\langle \vec{\xi} \vec{r}^\top \right\rangle^{s.s.} - \left\langle \vec{r} \vec{\xi}^\top \right\rangle^{s.s.} \mathbb{L}^\top, \end{aligned} \quad (4.10)$$

with $\{\cdot\}^{s.s.} \equiv \lim_{t \rightarrow \infty} \{\cdot\}(t)$. Equation (4.10) is an algebraic equation whose solution is the steady-state covariance matrix $\mathbb{C}^{s.s.}$. However, the two terms $\left\langle \vec{\xi} \vec{r}^\top \right\rangle^{s.s.}$ and $\left\langle \vec{r} \vec{\xi}^\top \right\rangle^{s.s.}$ need to be calculated before working out the solution. One approach to calculate $\left\langle \vec{\xi} \vec{r}^\top \right\rangle^{s.s.}$ would be to solve Eq. (4.5), but this is exactly what we are trying to avoid. It is here when the Novikov theorem comes useful, since it lets us compute $\left\langle \vec{\xi} \vec{r}^\top \right\rangle^{s.s.}$ without having to integrate the equations of motion. Using this theorem and the δ -correlation of the noises, we find the ij -th component of $\left\langle \vec{\xi}(t) \vec{r}(t)^\top \right\rangle$,

$$\begin{aligned} \langle \xi_i(t) r_j(t) \rangle &= \sum_{k=1}^2 \int_0^t d\tau \langle \xi_i(t) \xi_k(\tau) \rangle \left\langle \frac{\delta r_j(t)}{\delta \xi_k(\tau)} \right\rangle \\ &= \sum_{k=1}^2 \mathbb{D}_{ik} \lim_{\tau \rightarrow t^-} \left\langle \frac{\delta r_j(t)}{\delta \xi_k(\tau)} \right\rangle, \end{aligned} \quad (4.11)$$

where $\lim_{\tau \rightarrow t^-}$ is the limit when τ goes to t from below. Evaluation of the functional derivative $\delta r_j(t)/\delta \xi_k(\tau)$ for the $\tau \rightarrow t^-$ limit gives

$$\left\langle \vec{\xi}(t) \vec{r}(t)^\top \right\rangle = \mathbb{D}\mathbb{L}^\top. \quad (4.12)$$

Now, the algebraic equation that gives the steady-state covariance matrix becomes

$$\mathbb{A}\mathbb{C}^{s.s.} + \mathbb{C}^{s.s.}\mathbb{A}^\top = -\mathbb{B}, \quad (4.13)$$

with $\mathbb{B} = 2\mathbb{L}\mathbb{D}\mathbb{L}^\top$. By definition, the covariance matrix is symmetric, but there are also additional restrictions imposed by the equations of motion and the steady-state condition, which reduce the dimensionality of the problem of solving Eq. (4.13) [114]. Since $d\langle q_i q_j \rangle / dt = 0$ in the steady state, we have

$$\begin{aligned} \langle p_1 q_1 \rangle^{s.s.} &= \langle p_2 q_2 \rangle^{s.s.} = 0, \\ \frac{\langle p_1 q_2 \rangle^{s.s.}}{m_1} &= -\frac{\langle q_1 p_2 \rangle^{s.s.}}{m_2}. \end{aligned} \quad (4.14)$$

Taking (4.14) into account, the steady-state covariance matrix takes the form

$$\mathbb{C}^{s.s.} = \begin{pmatrix} \langle q_1^2 \rangle^{s.s.} & \langle q_1 q_2 \rangle^{s.s.} & 0 & \frac{\langle p_2 q_1 \rangle^{s.s.}}{m_2} \\ \langle q_1 q_2 \rangle^{s.s.} & \langle q_2^2 \rangle^{s.s.} & -\frac{\langle p_2 q_1 \rangle^{s.s.}}{m_2} & 0 \\ 0 & -\frac{\langle p_2 q_1 \rangle^{s.s.}}{m_2} & \frac{\langle p_1^2 \rangle^{s.s.}}{m_1^2} & \frac{\langle p_1 p_2 \rangle^{s.s.}}{m_1 m_2} \\ \frac{\langle p_2 q_1 \rangle^{s.s.}}{m_2} & 0 & \frac{\langle p_1 p_2 \rangle^{s.s.}}{m_1 m_2} & \frac{\langle p_2^2 \rangle^{s.s.}}{m_2^2} \end{pmatrix}. \quad (4.15)$$

The explicit set of equations for the components of $\mathbb{C}^{s.s.}$ can be found in Appendix 1.

4.4 Solutions

In this section we use the solution to Eq. (4.13) to write down the temperatures and currents in the steady state. We use Mathematica to obtain analytic expressions for the temperatures,

$$\begin{aligned} T_1 &= \frac{T_L \mathcal{P}_{1,L}(k) + T_R \mathcal{P}_{1,R}(k)}{\mathcal{D}(k)}, \\ T_2 &= \frac{T_L \mathcal{P}_{2,L}(k) + T_R \mathcal{P}_{2,R}(k)}{\mathcal{D}(k)}, \end{aligned} \quad (4.16)$$

where $\mathcal{D}(k) = \sum_{n=0}^2 \mathcal{D}_n k^n$ and $\mathcal{P}_{i,(L/R)}(k) = \sum_{n=0}^2 a_{i,n,(L/R)} k^n$ are polynomials in the coupling constant k with coefficients

$$\begin{aligned}
\mathcal{D}_0 &= a_{1,0,L} = a_{2,0,R} = \gamma_L \gamma_R \left[h^{(1)} (\gamma_L k_R + \gamma_R k_L) + (m_1 k_R - m_2 k_L)^2 \right], \\
\mathcal{D}_1 &= a_{1,1,L} = a_{2,1,R} = \gamma_L \gamma_R \left[h^{(0)} h^{(1)} + 2(m_1 - m_2)(m_1 k_R - m_2 k_L) \right], \\
\mathcal{D}_2 &= h^{(0)} h^{(2)}, \\
a_{1,2,L} &= \gamma_L (m_2 h^{(1)} + \gamma_R (m_1 - m_2)^2), \\
a_{1,2,R} &= h^{(1)} m_1 \gamma_R, \\
a_{2,2,L} &= h^{(1)} m_2 \gamma_L, \\
a_{2,2,R} &= \gamma_R (m_1 h^{(1)} + \gamma_L (m_1 - m_2)^2), \\
a_{1,0,R} &= a_{1,1,R} = a_{2,0,L} = a_{2,1,L} = 0,
\end{aligned} \tag{4.17}$$

where $h^{(n)} \equiv \gamma_R m_1^n + \gamma_L m_2^n$. The currents from the baths to the masses [114] are

$$\begin{aligned}
J_L &= k_B \frac{\gamma_L}{m_1} (T_L - T_1), \\
J_R &= k_B \frac{\gamma_R}{m_2} (T_R - T_2),
\end{aligned} \tag{4.18}$$

with T_i given by Eq. (4.16). Since, in the steady state, $J_L = -J_R$ we will use the shorthand notation $J \equiv J_L$. Substituting Eq. (4.16) into Eq. (4.18) we get for the heat current

$$J = \kappa (T_L - T_R), \tag{4.19}$$

where $\kappa = k_B k^2 \gamma_L \gamma_R h^{(1)} / \mathcal{D}(k)$ acts as an effective thermal conductance, which depends on the parameters of the system, i.e., the masses and spring constants, and also on the friction coefficients of the baths. From Eq. (4.19) it could be thought that inverting the temperatures of the baths would only lead to an exchange of heat currents. However, since the thermal conductance κ depends on the friction coefficients, the exchange of the baths implies a change in its value. Moreover, it is possible to have temperature-dependent friction coefficients, as it happens in the physical set-up of laser-cooled trapped ions described in Section 4.5.

4.5 Relation of the Model to a trapped ion set-up

As we mentioned, the parameters k , k_L and k_R can be related to the elements of the Hessian matrix of a system in a stable equilibrium position. In this section we will identify these parameters with the Hessian matrix of a pair of trapped ions. Here we consider two different set-ups: two ions in a collective trap, and two ions in individual traps. In Section 4.6 we focus on two ions in individual traps to illustrate the analysis of rectification.

In both set-ups we assume strong confinement in the radial direction, making the effective dynamics one-dimensional. We will also assume that the confinement in the axial direction is purely electrostatic, which makes the effective spring constant independent of the mass of the ions [115]. Additionally, we will relate the temperatures and friction coefficients of the Langevin baths to those corresponding to Doppler cooling.

4.5.1 Collective trap

Consider two ions of unit charge with masses m_1 and m_2 trapped in a collective trap. Assuming strong radial confinement and purely electrostatic axial confinement, both ions feel the same harmonic oscillator potential with trapping constant k_{trap} [115]. The potential describing the system is

$$V_{collective} = \frac{1}{2}k_{trap}(x_1^2 + x_2^2) + \frac{\mathcal{C}}{x_2 - x_1}, \quad (4.20)$$

with $\mathcal{C} = \frac{Q^2}{4\pi\epsilon_0}$. The equilibrium positions for this potential are

$$x_2^{eq} = -x_1^{eq} = \left(\frac{1}{2}\right)^{2/3} \left(\frac{Q^2}{4\pi\epsilon_0 k_{trap}}\right)^{1/3}. \quad (4.21)$$

Assuming small oscillations of the ions around the equilibrium positions, the Hessian matrix of the system is

$$\begin{aligned}\mathbb{K}_{1,2} &= -\frac{Q^2}{2\pi\epsilon_0} \frac{1}{(x_2^{eq} - x_1^{eq})^3} = -k_{trap}, \\ \mathbb{K}_{1,1} &= k_{trap} + \frac{Q^2}{2\pi\epsilon_0} \frac{1}{(x_2^{eq} - x_1^{eq})^3} = 2k_{trap}, \\ \mathbb{K}_{2,2} &= k_{trap} + \frac{Q^2}{2\pi\epsilon_0} \frac{1}{(x_2^{eq} - x_1^{eq})^3} = 2k_{trap}.\end{aligned}\tag{4.22}$$

Using Eq. (4.22) we can relate the parameters of this physical set-up to those of the model described in Section 4.2 to find

$$k_L = k_R = k = k_{trap}.\tag{4.23}$$

4.5.2 Individual on-site traps

We can make the same assumptions for the axial confinement as in the previous subsection but now each of the ions is in an individual trap with spring constants $k_{trap,L}$ and $k_{trap,R}$ respectively. The potential of the system is

$$\begin{aligned}V_{individual} &= \frac{1}{2}k_{trap,L} (x_1 - x_L)^2 + \frac{1}{2}k_{trap,R} (x_2 - x_R)^2 \\ &\quad + \frac{\mathcal{C}}{x_2 - x_1},\end{aligned}\tag{4.24}$$

where x_L and x_R are the center positions of the on-site traps. The elements of the Hessian matrix in the equilibrium position are

$$\begin{aligned}\mathbb{K}_{1,2} &= -\frac{Q^2}{2\pi\epsilon_0} \frac{1}{(x_2^{eq} - x_1^{eq})^3}, \\ \mathbb{K}_{1,1} &= k_{trap,L} + \frac{Q^2}{2\pi\epsilon_0} \frac{1}{(x_2^{eq} - x_1^{eq})^3}, \\ \mathbb{K}_{2,2} &= k_{trap,R} + \frac{Q^2}{2\pi\epsilon_0} \frac{1}{(x_2^{eq} - x_1^{eq})^3}.\end{aligned}\tag{4.25}$$

Comparing the parameters in Eq. (4.25) with those in the model described in Section 4.2 we identify

$$\begin{aligned} k_L &= k_{\text{trap},L}, \\ k_R &= k_{\text{trap},R}, \\ k &= \frac{Q^2}{2\pi\epsilon_0} \frac{1}{(x_2^{\text{eq}} - x_1^{\text{eq}})^3}. \end{aligned} \quad (4.26)$$

In this case, the analytic expressions for the equilibrium positions are more complicated. We get for the distance between the equilibrium positions of the ions

$$\begin{aligned} (x_2 - x_1)^{(\text{eq})} &= \frac{1}{3} \Delta x_{LR} \\ &- \frac{1}{6} \left[\frac{2^{2/3} \zeta}{k_{\text{trap},L} k_{\text{trap},R} (k_{\text{trap},L} + k_{\text{trap},R})} \right. \\ &\left. + \frac{2^{4/3} k_{\text{trap},L} k_{\text{trap},R} (k_{\text{trap},L} + k_{\text{trap},R}) (x_R - x_L)^2}{\zeta} \right], \end{aligned} \quad (4.27)$$

where $\Delta x_{LR} = (x_R - x_L)$ and $\zeta = (Y - \eta)^{(1/3)}$, with

$$\begin{aligned} Y &= 3\sqrt{3} \left\{ \mathcal{C} k_{\text{trap},L}^4 k_{\text{trap},R}^4 (k_{\text{trap},L} + k_{\text{trap},R})^7 \times \right. \\ &\quad \left. [4k_{\text{trap},L} k_{\text{trap},R} \Delta x_{LR}^3 + 27\mathcal{C} (k_{\text{trap},L} + k_{\text{trap},R})] \right\}^{(1/2)}, \\ \eta &= k_{\text{trap},L}^2 k_{\text{trap},R}^2 (k_{\text{trap},L} + k_{\text{trap},R})^3 \times \\ &\quad [2k_{\text{trap},L} k_{\text{trap},R} \Delta x_{LR}^3 + 27\mathcal{C} (k_{\text{trap},L} + k_{\text{trap},R})]. \end{aligned} \quad (4.28)$$

In this set-up, the coupling between the ions k can be controlled by changing the distance between the on-site traps.

4.5.3 Optical molasses and Langevin baths

Trapped ions may be cooled down by a pair of counterpropagating lasers which are red-detuned with respect to an internal atomic transition of the ions. This technique is known as Doppler cooling or optical molasses [90, 91, 116, 117]. The off-resonant absorption of laser photons by the ions exerts a damping-like force that slows them down. The spontaneous emission of the ions produces heating due to the random recoil generated by the emitted photons. Both, the friction and recoil force are in balance, and eventually the ion thermalizes to a finite temperature.

Thus the effect of the lasers on the ion is equivalent to a Langevin bath with temperature T_{molass} and friction coefficient γ_{molass} . The temperature and friction coefficients are controlled with the laser intensity I and frequency detuning δ with respect to the selected internal transition by the expressions [81, 90, 91],

$$\begin{aligned}\gamma_{molass}(I, \delta) &= -4\hbar \left(\frac{\delta + \omega_0}{c} \right)^2 \left(\frac{I}{I_0} \right) \frac{2\delta/\Gamma}{[1 + (2\delta/\Gamma)^2]^2}, \\ T_{molass}(\delta) &= -\frac{\hbar\Gamma}{4k_B} \frac{1 + (2\delta/\Gamma)^2}{(2\delta/\Gamma)},\end{aligned}\tag{4.29}$$

where ω_0 is the frequency of the selected internal atomic transition, Γ is the natural width of the excited state, and I_0 is the saturation intensity.

4.6 Looking for rectification

We will say that we observe rectification whenever the heat current J for a configuration of the baths changes when we exchange the baths to \tilde{J} . The important point here is to define what is meant by *exchanging the baths*. We consider that a bath is characterized, not only by its temperature T but also by its coupling to the system by means of the friction coefficient γ , so, exchanging the baths is achieved by exchanging both the temperatures and the friction coefficients, as summarized in Table 4.1.

When implementing temperatures and friction coefficients by lasers, this exchange operation is performed by changing the values of the intensities and detunings acting on each ion (Eq. (4.29)). The exchange operation is straightforward when the two ions are either of the same species or isotopes of each other, since the only required action is to exchange the values of the detunings of the lasers without modifying the intensities. However, if we deal with two different species, i.e., with two different atomic transitions, the laser wavelengths and the decay rates depend on the species. Then, exchanging the temperatures by modifying the detunings, keeping the laser intensities constant, does not necessarily imply an exchange of the friction coefficients. Nevertheless it is possible to adjust the laser intensities so that the friction coefficients get exchanged and that is the assumption hereafter. The idea of implementing a bath exchange like this follows the same line of thought as [34], since we are adding a temperature dependent feature to the system -the friction coefficients- that changes as the baths are inverted.

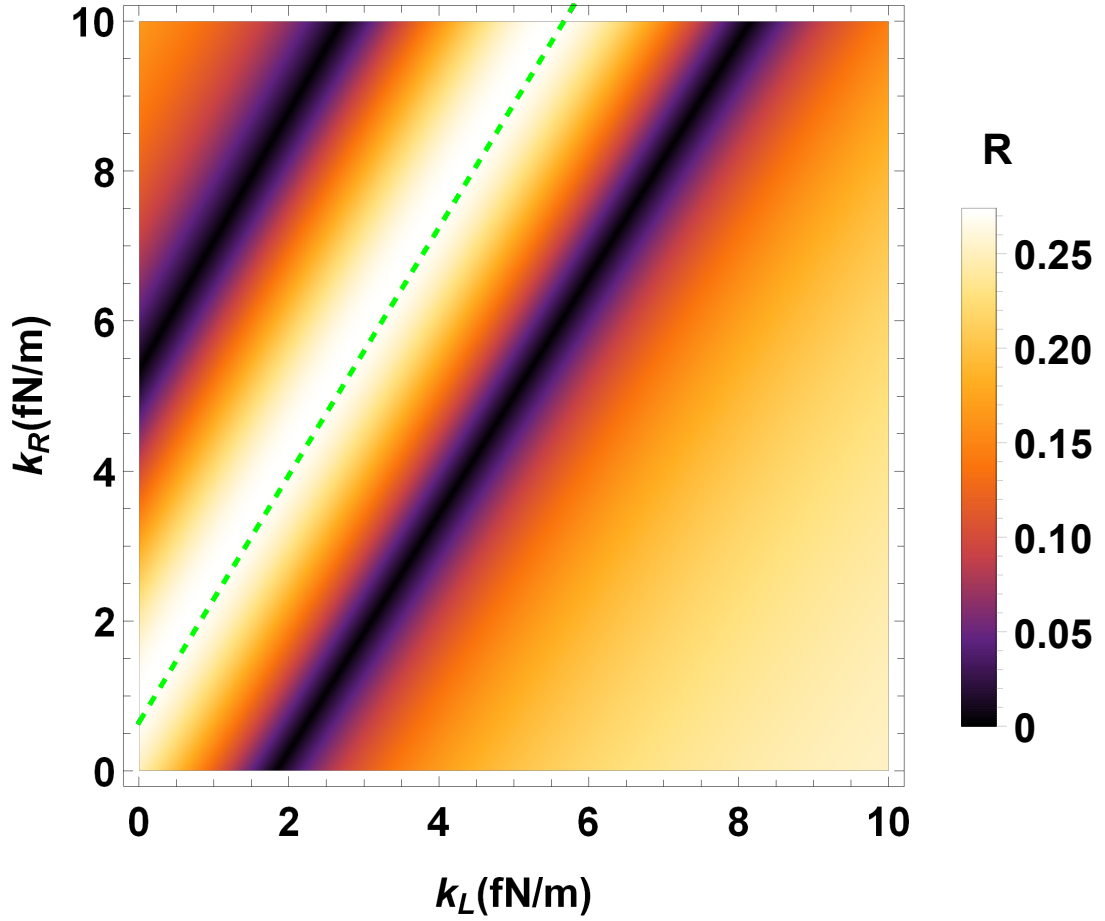


FIGURE 4.2: Rectification, R , in the $k_L k_R$ plane for $k = 1.17 \times \text{fN/m}$, $\gamma_L = 6.75 \times 10^{-22} \text{ kg/s}$, and $\gamma_R = 4.64\gamma_L$.

TABLE 4.1: Definition of forward and reversed (exchanged) bath configurations.

	forward	reversed
Bath Friction	γ_L, γ_R	$\tilde{\gamma}_L = \gamma_R, \tilde{\gamma}_R = \gamma_L$
Bath Temperature	T_L, T_R	$\tilde{T}_L = T_R, \tilde{T}_R = T_L$

To measure rectification, we will use the rectification coefficient R defined as

$$R = \frac{|J - \tilde{J}|}{\max(J, \tilde{J})}, \quad (4.30)$$

that is, the ratio between the difference of heat currents and the largest one. As defined, $R = 0$ for no asymmetry of the heat currents and $R = 1$ when they are maximally asymmetric.

4.6.1 Parametric exploration

We have explored thoroughly the space formed by the parameters of the model to find asymmetric heat transport, namely, $m_1, m_2, k, k_L, k_R, \gamma_L, \gamma_R$. We have fixed the values of some of the parameters to realistic ones while we have varied the rest. We have set the masses to $m_1 = 24.305$ a.u. and $m_2 = 40.078$ a.u., which correspond to Mg and Ca, whose ions are broadly used in trapped-ion physics. The temperatures are also fixed and, as Eq. (4.19) shows, rectification does not formally depend on the temperature in this model, unless we set the friction coefficients as a function of temperature using Eq. (4.29) explicitly.

Figure 4.2 depicts the values of the rectification after sweeping the $k_L k_R$ plane for fixed values of k , γ_L , and γ_R . A remarkable result from this figure is that parallel lines appear alternating minima and maxima of R . With a numerical fitting, we find that the line corresponding to the highest maximum value of R is determined by

$$\frac{k + k_L}{m_1} = \frac{k + k_R}{m_2}. \quad (4.31)$$

In a trapped-ion context the condition (4.31) may be imposed by adjusting the distance of the traps for fixed k_L and k_R . It is also remarkable that when Eq. (4.31) is satisfied, the rectification no longer depends on the spring constants of the model. This last result can be found assuming Eq. (4.31) when calculating the currents with Eq. (4.19) and R with Eq. (4.30),

$$R = \begin{cases} 1 - \frac{a+g}{1+ag} & \text{if } (a+g) < (1+ag) \\ 1 - \frac{1+ag}{a+g} & \text{if } (a+g) > (1+ag) \\ 0 & \text{if } (a+g) = (1+ag), \end{cases} \quad (4.32)$$

where a and g are the mass and friction coefficients ratios

$$\begin{aligned} a &= m_2/m_1, \\ g &= \gamma_R/\gamma_L. \end{aligned} \quad (4.33)$$

The maximal rectification found does not scale with the magnitude of the masses or the friction coefficients, just with their ratios. Besides a high R , it is important to have non-vanishing heat currents [114]. Using again Eq. (4.31) in the expression

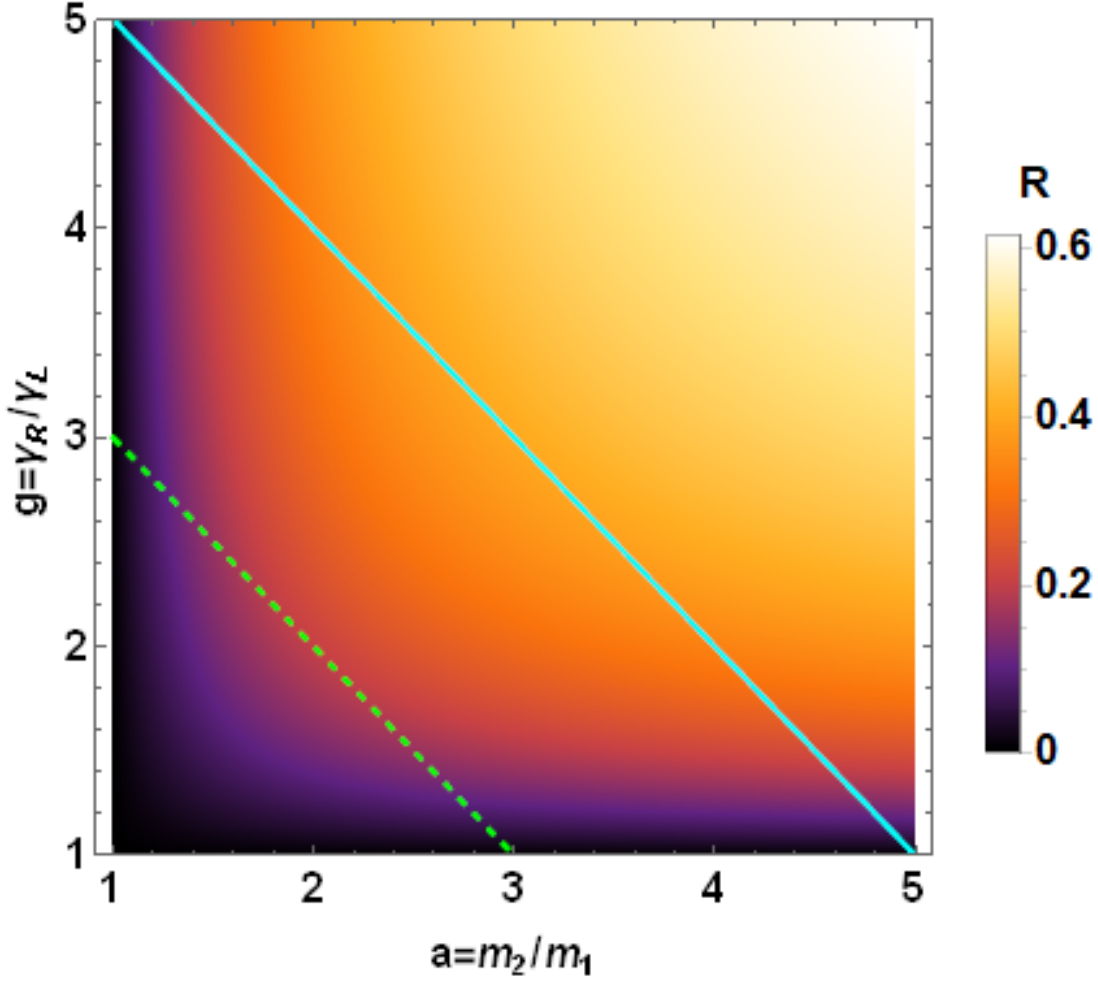
for the currents (4.19), the maximum current $J_{\max} = \max(|J|, |\tilde{J}|)$ is

$$J_{\max} = \begin{cases} \frac{k_B g \gamma_L k^2 |T_L - T_R|}{(a+g)(g\gamma_L^2(k_L+k)+k^2 m_1)} & \text{if } (a+g) < (1+ag) \\ \frac{k_B g \gamma_L k^2 |T_L - T_R|}{(1+ag)(g\gamma_L^2(k_L+k)+k^2 m_1)} & \text{if } (a+g) > (1+ag). \end{cases} \quad (4.34)$$

Now we analyze how the parameters a and g affect the maximum current J_{\max} in (4.34). To do this, we can divide the ag plane in four quadrants by the axes $a = 1$ and $g = 1$ (in those axes $R = 0$). In Eq. (4.34) the parameter a appears only in the denominator, thus for a higher a , a smaller current is found. The quadrants with $a < 1$ will be better for achieving large currents. However, g appears both in the numerator and denominator so there is no obvious advantageous quadrant for this parameter.

Equation (4.32) is symmetric upon the transformations $a \leftrightarrow 1/a$ and $g \leftrightarrow 1/g$. Using a logarithmic scale for a and g , the resulting R map will be symmetric with respect to the $a = 1$ and $g = 1$ axes. We can limit ourselves to analyze the quadrant $a > 1$, $g > 1$, as the results in other quadrants will be equivalent upon transformations $a \leftrightarrow 1/a$ and $g \leftrightarrow 1/g$.

Fig. 4.3 shows the rectification given by Eq. (4.32) in terms of a and g . Along any diagonal line (parallel to the solid cyan or the dashed green lines), the maximum value is at the center, that is, when $a = g$. However, if we fix a , increasing g always increases R . Although we could increase g arbitrarily to get more rectification this is not a realistic option in a trapped-ion set-up. Since g is defined as the ratio between the friction coefficients, increasing it means making either γ_L go to 0 or γ_R to infinity. Making γ_L go to 0 decouples one of the ions from the bath, so the heat current tends to vanish in any direction. Also, increasing γ_R arbitrarily is impossible since the Doppler cooling friction coefficient as a function of the laser detuning (Eq. (4.29)) is bounded. Although Eq. (4.29) suggests that boosting the laser intensity can also increase the friction coefficient, this is not an option since Eq. (4.29) is just an approximation for low laser intensities. When going to higher intensities, the emission/absorption of photons by the ion is saturated and the friction coefficient reaches a finite value proportional to the width Γ of the excited state [91]. As a compromise between feasibility and high R , we set the ratio between the friction coefficients g to be equal to the mass ratio a . As shown in Fig. 4.3, along the solid-cyan and dashed-green diagonal lines the maximum R is achieved for $a = g$. Fig. 4.4 shows the rectification in Eq. (4.32)

FIGURE 4.3: Rectification factor, R , given by Eq. (4.32).

for the line $a = g$. When both parameters are large enough, the rectification goes to 1.

4.6.2 Spectral match/mismatch approach to rectification

The match/mismatch between the power spectra of the particles controls the heat currents in the system [30, 37]. A good match between the power spectra of the two ions in a large range of frequencies yields a higher heat current through the system while the mismatch reduces the heat current. If there is a good match between the spectra of the ions (i.e., their peaks overlap in a broad range of frequencies) for a certain baths configuration, and mismatch when the baths exchange, the system will present heat rectification.

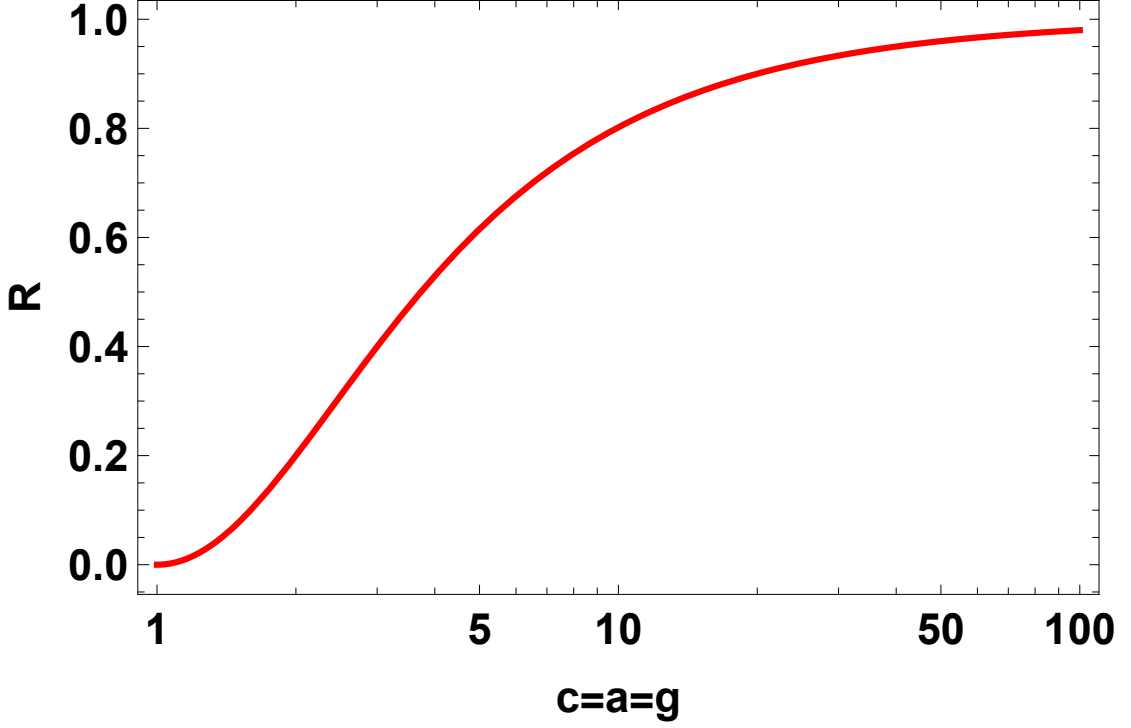


FIGURE 4.4: Rectification for different values of $c = m_2/m_1 = \gamma_R/\gamma_L$ when the maximum condition in the $k_L k_R$ plane is satisfied (Eq. (4.31)).

We have studied the phonon spectra of our model for several sets of parameters exhibiting no rectification or strong rectification. The phonon spectra of the ions is calculated through the spectral density matrix. For a real-valued stochastic process $\vec{x}(t)$, its spectral density matrix is defined as [97]

$$\mathbb{S}_{\vec{x}}(\omega) \equiv \left\langle \vec{X}(\omega) \vec{X}^\top(-\omega) \right\rangle, \quad (4.35)$$

with $\vec{X}(\omega)$ being the Fourier transform of $\vec{x}(t)$ (we are using the convention of multiplying by a factor of 1 and $\frac{1}{2\pi}$ for the transform and its inverse operation). A justification of the use of the spectral density matrix to understand heat transport arises from the Wiener-Khinchin theorem [97], which says that the correlation matrix of a stationary stochastic process in the steady state is the inverse Fourier transform of its spectral density matrix $\langle \vec{r}(t) \vec{r}^\top(t + \tau) \rangle = \mathcal{F}^{-1}[\mathbb{S}_{\vec{r}}(\omega)](\tau)$. This result allows us to write down the covariance matrix in the steady state through the spectral density as

$$\mathbb{C}^{s.s.} = \frac{1}{2\pi} \int_{-\infty}^{\infty} d\omega \mathbb{S}_{\vec{r}}(\omega). \quad (4.36)$$

Eq. (4.36) directly connects the spectral density matrix to the steady-state temperature and, therefore, to the heat currents (in Section 4.3 we saw that $T_1^{s.s.} =$

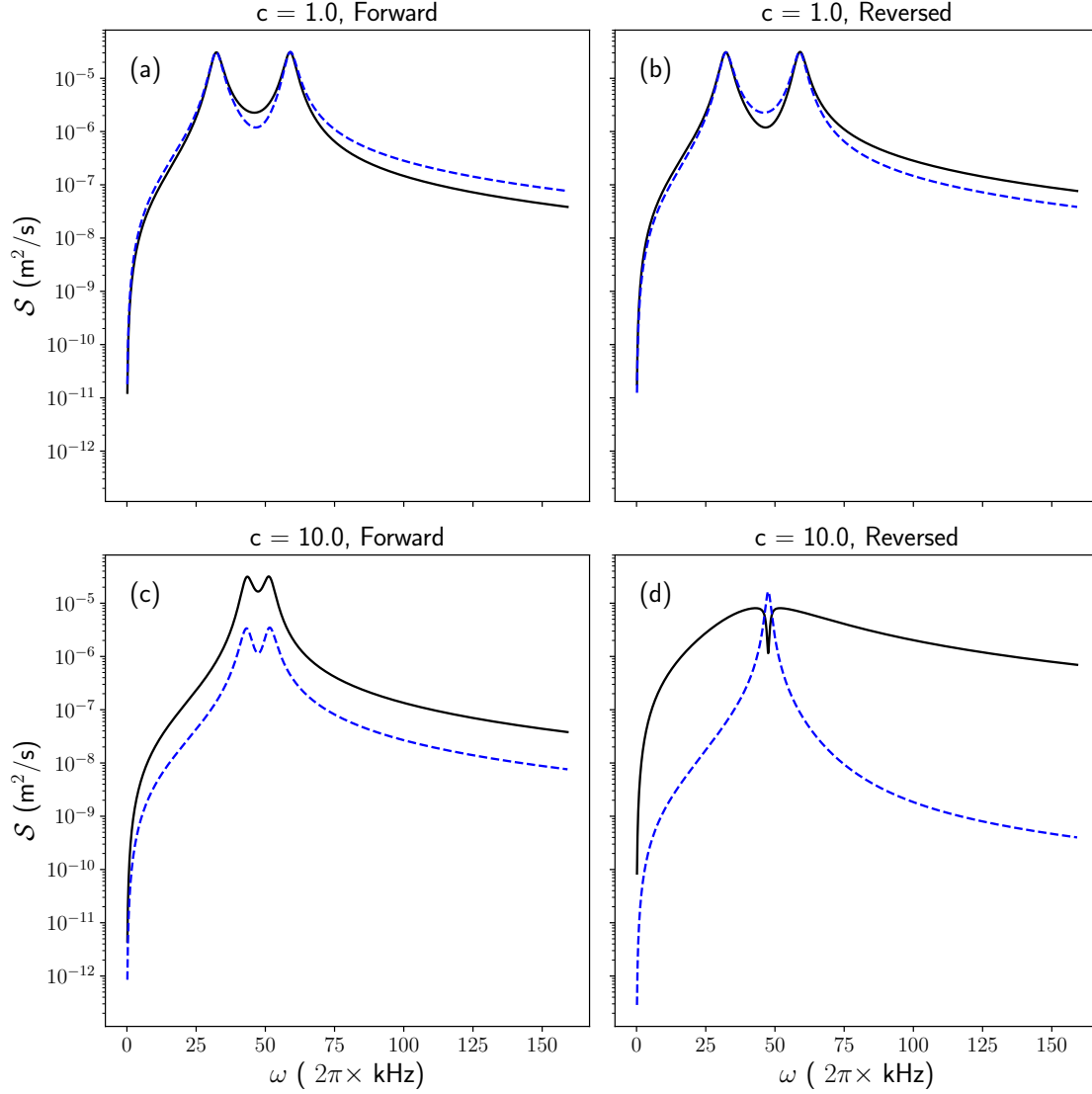


FIGURE 4.5: Spectral densities of the velocities of the ions (r_3 and r_4) corresponding to different values of c in Fig. 4.4: (a), (b) for $c = 1$ and (c), (d) for $c = 10$. Solid, black lines correspond to the left ion velocity spectral density $S_{3,3}(\omega)$ and dashed, blue lines correspond to the right ion velocity spectral density $S_{4,4}(\omega)$. (a) and (b) correspond to $R = 0$: the overlap between the phonon bands is the same in the forward and reversed configurations. (c) and (d) correspond to $R \approx 0.8$: in the forward configuration (c) the phonons match better than in the reversed configuration (d).

$$m_1 C_{3,3}^{s.s.}/k_B \text{ and } T_2^{s.s.} = m_2 C_{4,4}^{s.s.}/k_B).$$

For the vector process $\vec{r}(t)$ describing the evolution of our system we have $\vec{R}(\omega) = (i\omega - \mathbb{A})^{-1} \mathbb{L} \vec{\Xi}(\omega)$ with $\vec{\Xi}(\omega)$ being the Fourier transform of the white noise $\vec{\xi}(t)$. Note that $\vec{\Xi}(\omega)$ does not strictly exist, because it is not square-integrable, however its spectral density is $S_{\vec{\xi}}(\omega) = 2\mathbb{D}$ [97], which is flat as expected for a white noise. Therefore, the spectral density matrix of the system

is

$$\mathbb{S}_{\vec{r}} = 2 (\mathbb{A} - i\omega)^{-1} \mathbb{L} \mathbb{D} \mathbb{L}^T (\mathbb{A} + i\omega)^{-T}. \quad (4.37)$$

As we can see in Eq. (4.37), the imaginary part of the eigenvalues of the dynamical matrix \mathbb{A} correspond to the peaks in the spectrum whereas the real part dictates their width. The spectral density matrix of our model is

$$\mathbb{S}_{\vec{r}}(\omega) = 2k_B \frac{\gamma_L T_L \mathbb{S}_L(i\omega) + \gamma_L T_R \mathbb{S}_R(i\omega)}{(m_1 m_2)^2 P_{\mathbb{A}}(i\omega) P_{\mathbb{A}}(-i\omega)}, \quad (4.38)$$

where $P_{\mathbb{A}}(\lambda)$ is the characteristic polynomial of the dynamical matrix \mathbb{A} and $\mathbb{S}_L(\omega)$, $\mathbb{S}_R(\omega)$ are the matrix polynomials in the angular frequency ω whose coefficients are defined in Appendix .2. Equation (4.39) gives the full expressions of the spectral densities for the velocities, $\mathbb{S}_{3,3}(\omega) = \langle R_3(\omega) R_3(-\omega) \rangle$ for the left ion, and $\mathbb{S}_{4,4}(\omega) = \langle R_4(\omega) R_4(-\omega) \rangle$ for the right ion, since they are the elements related to the calculation of the heat current using Eq. (4.36),

$$\begin{aligned} \mathbb{S}_{3,3}(\omega) &= 2k_B \frac{\gamma_R k^2 T_R \omega^2 + \gamma_L T_L [\omega^4 (\gamma_R^2 - 2km_2 - 2k_R m_2) + \omega^2 (k + k_R)^2 + m_2^2 \omega^6]}{(m_1 m_2)^2 P_{\mathbb{A}}(i\omega) P_{\mathbb{A}}(-i\omega)}, \\ \mathbb{S}_{4,4}(\omega) &= 2k_B \frac{\gamma_L k^2 T_L \omega^2 + \gamma_R T_R [\omega^4 (\gamma_L^2 - 2km_1 - 2k_L m_1) + \omega^2 (k + k_L)^2 + m_1^2 \omega^6]}{(m_1 m_2)^2 P_{\mathbb{A}}(i\omega) P_{\mathbb{A}}(-i\omega)}. \end{aligned} \quad (4.39)$$

Figure 4.5 depicts a series of plots of the spectra given by Eq. (4.39) that correspond to two points in Fig. 4.4. For $c = 1$ (Fig. 4.5(a) and (b)) there is no rectification, since the spectra match in the forward (a) and reversed (b) configurations. However, for $c = 10$ ((Fig. 4.5(c) and (d))) the picture is very different: there is a good match between the spectra in the forward configuration whereas in the reversed configuration the spectra are less correlated, giving as a result higher rectification ($R \approx 0.8$). Figure 4.5 only shows the elements (3,3) and (4,4) in the diagonal of \mathbb{S} but the remaining elements, including off-diagonal ones, exhibit a similar behavior.

4.7 Conclusions

We have studied heat rectification in a model composed of two coupled harmonic oscillators connected to baths. This simple model allows analytical treatment but

still has enough complexity to examine different ingredients that can produce rectification. Our results demonstrate in a simple but realistic system that harmonic systems can rectify heat current if they have features which depend on the temperature [34]. We implement this notion of temperature-dependent features by defining the baths exchange operation as an exchange of both temperatures and coupling parameters of the baths to the system. This kind of temperature-dependent features happens naturally in laser-cooled trapped ion set-ups.

We have also studied the phonon spectra of the system, comparing the match/mismatch of the phonon bands, to reach the conclusion that the band match/mismatch description for heat rectification is also valid for systems which are harmonic, as long as there are temperature-dependent features. We hope this article sheds more light into the topic of heat rectification and that encourages more research regarding its physical implementation on chains of trapped ions.

4.8 acknowledgements

We thank Daniel Alonso for fruitful discussions and comments. This work was supported by the Basque Country Government (Grant No. IT986-16), by Grants PGC2018-101355-B-I00 (MCIU/AEI/FEDER,UE) and FIS2016-80681P, and by the Spanish MICINN and European Union (FEDER) (Grant No. FIS2017-82855-P). M.A.S. acknowledges support by the Basque Government predoctoral program (Grant No. PRE-2019-2-0234).

.1 Full set of steady-state equations for the components of $\mathbb{C}^{s.s}$

Here we present the full set of equations for the covariance matrix elements in the steady state,

$$\begin{aligned}
& \frac{2k \langle p_2 q_1 \rangle^{s.s.}}{m_1 m_2} + \frac{2\gamma_L \langle p_1^2 \rangle^{s.s.}}{m_1^3} = \frac{2D_L}{m_1^2}, \\
& -\frac{2k \langle p_2 q_1 \rangle^{s.s.}}{m_2^2} + \frac{2\gamma_R \langle p_2^2 \rangle^{s.s.}}{m_2^3} = \frac{2D_R}{m_2^2}, \\
& -\frac{(k_L + k) \langle q_1 q_2 \rangle^{s.s.}}{m_1} + \frac{k \langle q_2^2 \rangle^{s.s.}}{m_1} + \frac{\gamma_L \langle p_2 q_1 \rangle^{s.s.}}{m_1 m_2} + \frac{\langle p_1 p_2 \rangle^{s.s.}}{m_1 m_2} = 0, \\
& \frac{(k_L + k) \langle p_2 q_1 \rangle^{s.s.}}{m_1 m_2} - \frac{(k_R + k) \langle p_2 q_1 \rangle^{s.s.}}{m_2^2} + \frac{\gamma_L \langle p_1 p_2 \rangle^{s.s.}}{m_1^2 m_2} + \frac{\gamma_R \langle p_1 p_2 \rangle^{s.s.}}{m_1 m_2^2} = 0, \\
& -\frac{(k_L + k) \langle q_1^2 \rangle^{s.s.}}{m_1} + \frac{k \langle q_1 q_2 \rangle^{s.s.}}{m_1} + \frac{\langle p_1^2 \rangle^{s.s.}}{m_1^2} = 0, \\
& -\frac{(k_R + k) \langle q_2^2 \rangle^{s.s.}}{m_2} + \frac{k \langle q_1 q_2 \rangle^{s.s.}}{m_2} + \frac{\langle p_2^2 \rangle^{s.s.}}{m_2^2} = 0, \\
& -\frac{(k_R + k) \langle q_1 q_2 \rangle^{s.s.}}{m_2} + \frac{k \langle q_1^2 \rangle^{s.s.}}{m_2} - \frac{\gamma_R \langle p_2 q_1 \rangle^{s.s.}}{m_2^2} + \frac{\langle p_1 p_2 \rangle^{s.s.}}{m_1 m_2} = 0
\end{aligned} \tag{40}$$

.2 Complete expressions for the Spectral Density Matrix

In Section 4.6 we used the characteristic polynomial $P_{\mathbb{A}}(\lambda)$ of the dynamical matrix \mathbb{A} for the calculation of the spectral density matrix. $P_{\mathbb{A}}(\lambda)$ is defined as

$$\begin{aligned}
\det(\mathbb{A} - \lambda) &= \lambda^4 \\
&+ \lambda^3 \left(\frac{\gamma_L}{m_1} + \frac{\gamma_R}{m_2} \right) \\
&+ \lambda^2 \frac{(\gamma_L \gamma_R + m_2(k + k_L) + m_1(k + k_R))}{m_1 m_2} \\
&+ \lambda \frac{(\gamma_R(k + k_L) + \gamma_L(k + k_R))}{m_1 m_2} \\
&+ \frac{k(k_L + k_R) + k_L k_R}{m_1 m_2}.
\end{aligned} \tag{41}$$

We also used the polynomials $\mathbb{S}_L(\lambda)$ and $\mathbb{S}_R(\lambda)$, which are defined as $\mathbb{S}_L(\lambda) = \sum_{n=0}^6 \lambda^n \sim_{L,n}$ and $\mathbb{S}_R(\lambda) = \sum_{n=0}^6 \lambda^n \sim_{R,n}$. There are 14 different polynomial coefficients, which are 4×4 matrices, which makes very cumbersome to include them in the main text. This is the full list of coefficients,

$$\begin{aligned}
\sim_{L,0} &= \begin{pmatrix} (k+k_R)^2 & k(k+k_R) & 0 & 0 \\ k(k+k_R) & k^2 & 0 & 0 \\ 0 & 0 & 0 & 0 \\ 0 & 0 & 0 & 0 \end{pmatrix}, & \sim_{R,0} &= \begin{pmatrix} k^2 & k(k+k_L) & 0 & 0 \\ k(k+k_L) & (k+k_L)^2 & 0 & 0 \\ 0 & 0 & 0 & 0 \\ 0 & 0 & 0 & 0 \end{pmatrix}, \\
\sim_{L,1} &= \begin{pmatrix} 0 & k\gamma_R & -(k+k_R)^2 & -k(k+k_R) \\ -k\gamma_R & 0 & -k(k+k_R) & -k^2 \\ (k+k_R)^2 & k(k+k_R) & 0 & 0 \\ k(k+k_R) & k^2 & 0 & 0 \end{pmatrix}, & \sim_{R,1} &= \begin{pmatrix} 0 & -k\gamma_L & 0 & 0 \\ k\gamma_L & 0 & 0 & 0 \\ k^2 & k(k+k_L) & 0 & 0 \\ k(k+k_L) & (k+k_L)^2 & 0 & 0 \end{pmatrix}, \\
\sim_{L,2} &= \begin{pmatrix} 2(k+k_R)m_2 - \gamma_R^2 & km_2 & 0 & -k\gamma_R \\ km_2 & 0 & k\gamma_R & 0 \\ 0 & k\gamma_R & -(k+k_R)^2 & -k(k+k_R) \\ -k\gamma_R & 0 & -k(k+k_R) & -k^2 \end{pmatrix}, & \sim_{R,2} &= \begin{pmatrix} 0 & km_1 & 0 & 0 \\ km_1 & 2(k+k_L)m_1 - \gamma_L^2 & 0 & 0 \\ 0 & -k\gamma_L & 0 & 0 \\ k\gamma_L & 0 & 0 & 0 \end{pmatrix}, \\
\sim_{L,3} &= \begin{pmatrix} 0 & 0 & \gamma_R^2 - 2(k+k_R)m_2 & -km_2 \\ 0 & 0 & -km_2 & 0 \\ 2(k+k_R)m_2 - \gamma_R^2 & km_2 & 0 & -k\gamma_R \\ km_2 & 0 & k\gamma_R & 0 \end{pmatrix}, & \sim_{R,3} &= \begin{pmatrix} 0 & 0 & 0 & 0 \\ 0 & 0 & 0 & 0 \\ 0 & km_1 & 0 & 0 \\ km_1 & 2(k+k_L)m_1 - \gamma_L^2 & 0 & 0 \end{pmatrix}, \\
\sim_{L,4} &= \begin{pmatrix} m_2^2 & 0 & 0 & 0 \\ 0 & 0 & 0 & 0 \\ 0 & 0 & \gamma_R^2 - 2(k+k_R)m_2 & -km_2 \\ 0 & 0 & -km_2 & 0 \end{pmatrix}, & \sim_{R,4} &= \begin{pmatrix} 0 & 0 & 0 & 0 \\ 0 & m_1^2 & 0 & 0 \\ 0 & 0 & 0 & 0 \\ 0 & 0 & -km_1 & \gamma_L^2 - 2(k+k_L)m_1 \end{pmatrix}, \\
\sim_{L,5} &= \begin{pmatrix} 0 & 0 & -m_2^2 & 0 \\ 0 & 0 & 0 & 0 \\ m_2^2 & 0 & 0 & 0 \\ 0 & 0 & 0 & 0 \end{pmatrix}, & \sim_{R,5} &= \begin{pmatrix} 0 & 0 & 0 & 0 \\ 0 & 0 & 0 & -m_1^2 \\ 0 & 0 & 0 & 0 \\ 0 & m_1^2 & 0 & 0 \end{pmatrix}, \\
\sim_{L,6} &= \begin{pmatrix} 0 & 0 & 0 & 0 \\ 0 & 0 & 0 & 0 \\ 0 & 0 & -m_2^2 & 0 \\ 0 & 0 & 0 & 0 \end{pmatrix}, & \sim_{R,6} &= \begin{pmatrix} 0 & 0 & 0 & 0 \\ 0 & 0 & 0 & 0 \\ 0 & 0 & 0 & 0 \\ 0 & 0 & 0 & -m_1^2 \end{pmatrix}.
\end{aligned}$$

(42)

Conclusions

My pleasure.

Appendix

Appendix A

Interaction versus asymmetry for adiabatic following

Extra information to add to your thesis.

Bibliography

- [1] J. Muga, J. Palao, B. Navarro, and I. Egusquiza, “*Complex absorbing potentials*”, [Physics Reports](#) **395**, 357 - 426 (2004).
- [2] A. Ruschhaupt, F. Delgado, and J. G. Muga, “*Physical realization of -symmetric potential scattering in a planar slab waveguide*”, [Journal of Physics A: Mathematical and General](#) **38**, L171–L176 (2005).
- [3] J. Taylor, *Scattering Theory: Quantum Theory on Nonrelativistic Collisions*. Wiley, 1972.
- [4] A. Mostafazadeh, “*Pseudo-Hermitian Representation of Quantum Mechanics*”, [International Journal of Geometric Methods in Modern Physics](#) **07**, 1191 (2010).
- [5] M. Znojil, *Non-self-adjoint operators in quantum physics: ideas, people, and trends*, [ch. 1](#), pp. 7–58. Wiley, 2015.
- [6] S. Nixon and J. Yang, “*All-real spectra in optical systems with arbitrary gain-and-loss distributions*”, [Phys. Rev. A](#) **93**, 031802 (2016).
- [7] S. Nixon and J. Yang, “*Nonlinear light behaviors near phase transition in non-parity-time-symmetric complex waveguides*”, [Opt. Lett.](#) **41**, 2747–2750 (2016).
- [8] Y. Xu, L. Feng, M. Lu, and Y. Chen, “*Unidirectional Transmission Based on a Passive PT Symmetric Grating With a Nonlinear Silicon Distributed Bragg Reflector Cavity*”, [IEEE Photonics Journal](#) **6**, 1-7 (2014).
- [9] Y. Huang, C. Min, and G. Veronis, “*Broadband near total light absorption in non-PT-symmetric waveguide-cavity systems*”, [Opt. Express](#) **24**, 22219–22231 (2016).

- [10] Z. Lin, H. Ramezani, T. Eichelkraut, T. Kottos, H. Cao, and D. N. Christodoulides, “*Unidirectional Invisibility Induced by \mathcal{PT} -Symmetric Periodic Structures*”, [Phys. Rev. Lett. **106**, 213901 \(2011\)](#).
- [11] X. Yin and X. Zhang, “*Unidirectional light propagation at exceptional points*”, [Nature Materials **12**, 175–177 \(2013\)](#).
- [12] J. P. Palao, J. G. Muga, and R. Sala, “*Composite Absorbing Potentials*”, [Phys. Rev. Lett. **80**, 5469–5472 \(1998\)](#).
- [13] S. Brouard, D. Macias, and J. G. Muga, “*Perfect absorbers for stationary and wavepacket scattering*”, [Journal of Physics A: Mathematical and General **27**, L439–L445 \(1994\)](#).
- [14] J. Palao and J. Muga, “*A simple construction procedure of absorbing potentials*”, [Chemical Physics Letters **292**, 1 - 6 \(1998\)](#).
- [15] R. Snieder, “*The role of the Born approximation in nonlinear inversion*”, [Inverse Problems **6**, 247–266 \(1990\)](#).
- [16] A. Mostafazadeh, “*Transfer matrices as nonunitary S matrices, multimode unidirectional invisibility, and perturbative inverse scattering*”, [Phys. Rev. A **89**, 012709 \(2014\)](#).
- [17] S. A. R. Horsley, M. Artoni, and G. C. La Rocca, “*Spatial Kramers–Kronig relations and the reflection of waves*”, [Nature Photonics **9**, 436–439 \(2015\)](#).
- [18] S. Longhi, “*A unidirectionally invisible \mathcal{PT} -symmetric complex crystal with arbitrary thickness*”, [Journal of Physics A: Mathematical and Theoretical **47**, 485302 \(2014\)](#).
- [19] V. V. Konotop, J. Yang, and D. A. Zezyulin, “*Nonlinear waves in \mathcal{PT} -symmetric systems*”, [Rev. Mod. Phys. **88**, 035002 \(2016\)](#).
- [20] Z. Yu and S. Fan, “*Complete optical isolation created by indirect interband photonic transitions*”, [Nature Photonics **3**, 91–94 \(2009\)](#).
- [21] S. Longhi, “*Rapidly oscillating scatteringless non-Hermitian potentials and the absence of Kapitza stabilization*”, [EPL \(Europhysics Letters\) **118**, 20004 \(2017\)](#).

- [22] V. V. Konotop and D. A. Zezyulin, “*Phase transition through the splitting of self-dual spectral singularity in optical potentials*”, [Opt. Lett. **42**, 5206–5209 \(2017\)](#).
- [23] Y. V. Kartashov, V. V. Konotop, and D. A. Zezyulin, “*CPT-symmetric spin-orbit-coupled condensate*”,.
- [24] D. A. Zezyulin, Y. V. Kartashov, and V. V. Konotop, “*CPT-symmetric coupler with intermodal dispersion*”, [Opt. Lett. **42**, 1273–1276 \(2017\)](#).
- [25] A. Ruschhaupt, J. A. Damborenea, B. Navarro, J. G. Muga, and G. C. Hegerfeldt, “*Exact and approximate complex potentials for modelling time observables*”, [Europhysics Letters \(EPL\) **67**, 1–7 \(2004\)](#).
- [26] H. Feshbach, “*Unified theory of nuclear reactions*”, [Annals of Physics **5**, 357 - 390 \(1958\)](#).
- [27] H. Feshbach, “*A unified theory of nuclear reactions. II*”, [Annals of Physics **19**, 287 - 313 \(1962\)](#).
- [28] C. M. Bender and S. Boettcher, “*Real Spectra in Non-Hermitian Hamiltonians Having PT Symmetry*”, [Phys. Rev. Lett. **80**, 5243–5246 \(1998\)](#).
- [29] A. Guo, G. J. Salamo, D. Duchesne, R. Morandotti, M. Volatier-Ravat, V. Aimez, G. A. Siviloglou, and D. N. Christodoulides, “*Observation of PT-Symmetry Breaking in Complex Optical Potentials*”, [Phys. Rev. Lett. **103**, 093902 \(2009\)](#).
- [30] M. Terraneo, M. Peyrard, and G. Casati, “*Controlling the Energy Flow in Nonlinear Lattices: A Model for a Thermal Rectifier*”, [Phys. Rev. Lett. **88**, 094302 \(2002\)](#).
- [31] N. Roberts and D. Walker, “*A review of thermal rectification observations and models in solid materials*”, [International Journal of Thermal Sciences **50**, 648 - 662 \(2011\)](#).
- [32] N. Li, J. Ren, L. Wang, G. Zhang, P. Hänggi, and B. Li, “*Colloquium: Phononics: Manipulating heat flow with electronic analogs and beyond*”, [Rev. Mod. Phys. **84**, 1045–1066 \(2012\)](#).

- [33] S. Chen, E. Pereira, and G. Casati, “*Ingredients for an efficient thermal diode*”, *EPL (Europhysics Letters)* **111**, 30004 (2015).
- [34] E. Pereira, “*Requisite ingredients for thermal rectification*”, *Phys. Rev. E* **96**, 012114 (2017).
- [35] A. Ruschhaupt and J. G. Muga, “*Atom diode: A laser device for a unidirectional transmission of ground-state atoms*”, *Phys. Rev. A* **70**, 061604 (2004).
- [36] M. G. Raizen, A. M. Dudarev, Q. Niu, and N. J. Fisch, “*Compression of Atomic Phase Space Using an Asymmetric One-Way Barrier*”, *Phys. Rev. Lett.* **94**, 053003 (2005).
- [37] B. Li, L. Wang, and G. Casati, “*Thermal Diode: Rectification of Heat Flux*”, *Phys. Rev. Lett.* **93**, 184301 (2004).
- [38] B. Hu, L. Yang, and Y. Zhang, “*Asymmetric Heat Conduction in Nonlinear Lattices*”, *Phys. Rev. Lett.* **97**, 124302 (2006).
- [39] M. Peyrard, “*The design of a thermal rectifier*”, *Europhysics Letters (EPL)* **76**, 49–55 (2006).
- [40] G. Benenti, G. Casati, C. Mejía-Monasterio, and M. Peyrard, *From Thermal Rectifiers to Thermoelectric Devices*, pp. 365–407. Springer International Publishing, Cham, 2016.
https://doi.org/10.1007/978-3-319-29261-8_10.
- [41] B. Hu, D. He, L. Yang, and Y. Zhang, “*Thermal rectifying effect in macroscopic size*”, *Phys. Rev. E* **74**, 060201 (2006).
- [42] N. Zeng and J.-S. Wang, “*Mechanisms causing thermal rectification: The influence of phonon frequency, asymmetry, and nonlinear interactions*”, *Phys. Rev. B* **78**, 024305 (2008).
- [43] C. W. Chang, D. Okawa, A. Majumdar, and A. Zettl, “*Solid-State Thermal Rectifier*”, *Science* **314**, 1121–1124 (2006).
- [44] E. Pereira and R. R. Ávila, “*Increasing thermal rectification: Effects of long-range interactions*”, *Phys. Rev. E* **88**, 032139 (2013).

- [45] Y. Wang, A. Vallabhaneni, J. Hu, B. Qiu, Y. P. Chen, and X. Ruan, “*Phonon Lateral Confinement Enables Thermal Rectification in Asymmetric Single-Material Nanostructures*”, *Nano Letters* **14**, 592-596 (2014), <http://dx.doi.org/10.1021/nl403773f>.
- [46] H. Wang, S. Hu, K. Takahashi, X. Zhang, H. Takamatsu, and J. Chen, “*Suspended Monolayer Graphene*”, *Nature Comm.* **8**, 15483 (2016).
- [47] K. Joulain, J. Drevillon, Y. Ezzahri, and J. Ordóñez-Miranda, “*Quantum Thermal Transistor*”, *Phys. Rev. Lett.* **116**, 200601 (2016).
- [48] G. Katz and R. Kosloff, “*Quantum Thermodynamics in Strong Coupling: Heat Transport and Refrigeration*”, *Entropy* **18**, (2016).
- [49] L. Wang, Z. Wu, and L. Xu, “*Super heat diffusion in one-dimensional momentum-conserving nonlinear lattices*”, *Phys. Rev. E* **91**, 062130 (2015).
- [50] G. J. Martyna, M. L. Klein, and M. Tuckerman, “*Nosé–Hoover chains: The canonical ensemble via continuous dynamics*”, *The Journal of Chemical Physics* **97**, 2635-2643 (1992), <http://dx.doi.org/10.1063/1.463940>.
- [51] G. Casati, J. Ford, F. Vivaldi, and W. M. Visscher, “*One-Dimensional Classical Many-Body System Having a Normal Thermal Conductivity*”, *Phys. Rev. Lett.* **52**, 1861–1864 (1984).
- [52] B. Hu, B. Li, and H. Zhao, “*Heat conduction in one-dimensional chains*”, *Phys. Rev. E* **57**, 2992–2995 (1998).
- [53] S. Lepri, R. Livi, and A. Politi, “*Heat Conduction in Chains of Nonlinear Oscillators*”, *Phys. Rev. Lett.* **78**, 1896–1899 (1997).
- [54] S. Lepri, R. Livi, and A. Politi, “*Thermal conduction in classical low-dimensional lattices*”, *Physics Reports* **377**, 1 - 80 (2003).
- [55] P. A. Skordos and W. H. Zurek, “*Maxwell’s demon, rectifiers, and the second law: Computer simulation of Smoluchowski’s trapdoor*”, *American Journal of Physics* **60**, 876-882 (1992), <http://dx.doi.org/10.1119/1.17007>.
- [56] A. Ruschhaupt, J. G. Muga, and M. G. Raizen, “*Improvement by laser quenching of an ‘atom diode’: a one-way barrier for ultra-cold atoms*”,

Journal of Physics B: Atomic, Molecular and Optical Physics **39**, L133 (2006).

- [57] I. Bloch, “*Ultracold Quantum Gases in Optical Lattices*”, Nature Physics **1**, 23 (2005).
- [58] W. S. Bakr, J. I. Gillen, A. Peng, S. Fölling, and M. Greiner, “*A quantum gas microscope for detecting single atoms in a Hubbard-regime optical lattice*”, Nature **462**, 74 (2009).
- [59] C. Gollub, P. V. D. Hoff, M. Kowalewski, U. Troppmann, and R. D. Vivie-Riedle, *Vibrational Energy Transfer Through Molecular Chains: An Approach Toward Scalable Information Processing*, ch. 13, pp. 371–402. John Wiley & Sons, Inc., 2014.
- [60] C. Starr, “*The Copper Oxide Rectifier*”, Physics **7**, 15-19 (1936), <https://doi.org/10.1063/1.1745338>.
- [61] E. Pereira, “*Thermal rectification in classical and quantum systems: Searching for efficient thermal diodes*”, EPL (Europhysics Letters) **126**, 14001 (2019).
- [62] Z.-Q. Ye and B.-Y. Cao, “*Thermal rectification at the bimaterial nanocontact interface*”, Nanoscale **9**, 11480-11487 (2017).
- [63] L. Wang and B. Li, “*Thermal Memory: A Storage of Phononic Information*”, Phys. Rev. Lett. **101**, 267203 (2008).
- [64] L. Wang and B. Li, “*Thermal Logic Gates: Computation with Phonons*”, Phys. Rev. Lett. **99**, 177208 (2007).
- [65] B. Li, L. Wang, and G. Casati, “*Negative differential thermal resistance and thermal transistor*”, Applied Physics Letters **88**, 143501 (2006).
- [66] W. Kobayashi, Y. Teraoka, and I. Terasaki, “*An oxide thermal rectifier*”, Applied Physics Letters **95**, 171905 (2009).
- [67] D. M. Leitner, “*Thermal Boundary Conductance and Thermal Rectification in Molecules*”, The Journal of Physical Chemistry B **117**, 12820-12828 (2013).
- [68] M. Elzouka and S. Ndao, “*High Temperature Near-Field NanoThermoMechanical Rectification*”, Scientific Reports **7**, 44901 (2017).

- [69] N. Li, P. Hänggi, and B. Li, “*Ratcheting heat flux against a thermal bias*”, [EPL \(Europhysics Letters\) **84**, 40009 \(2008\)](#).
- [70] M. Pons, Y. Y. Cui, A. Ruschhaupt, M. A. Simón, and J. G. Muga, “*Local rectification of heat flux*”, [EPL \(Europhysics Letters\) **119**, 64001 \(2017\)](#).
- [71] J. Wang, E. Pereira, and G. Casati, “*Thermal rectification in graded materials*”, [Phys. Rev. E **86**, 010101 \(2012\)](#).
- [72] M. Romero-Bastida, J. O. Miranda-Peña, and J. M. López, “*Thermal rectification in mass-graded next-nearest-neighbor Fermi-Pasta-Ulam lattices*”, [Phys. Rev. E **95**, 032146 \(2017\)](#).
- [73] N. Yang, N. Li, L. Wang, and B. Li, “*Thermal rectification and negative differential thermal resistance in lattices with mass gradient*”, [Phys. Rev. B **76**, 020301 \(2007\)](#).
- [74] M. Romero-Bastida and J. M. Arizmendi-Carvajal, “*Structural influences on thermal rectification of one-dimensional mass-graded lattices*”, [Journal of Physics A: Mathematical and Theoretical **46**, 115006 \(2013\)](#).
- [75] R. Dettori, C. Melis, R. Rurali, and L. Colombo, “*Thermal rectification in silicon by a graded distribution of defects*”, [Journal of Applied Physics **119**, 215102 \(2016\)](#).
- [76] E. Pereira, “*Graded anharmonic crystals as genuine thermal diodes: Analytical description of rectification and negative differential thermal resistance*”, [Phys. Rev. E **82**, 040101 \(2010\)](#).
- [77] E. Pereira, “*Sufficient conditions for thermal rectification in general graded materials*”, [Phys. Rev. E **83**, 031106 \(2011\)](#).
- [78] R. R. Ávila and E. Pereira, “*Thermal rectification features: a study starting from local assumptions*”, [Journal of Physics A: Mathematical and Theoretical **46**, 055002 \(2013\)](#).
- [79] D. Bagchi, “*Thermal transport in the Fermi-Pasta-Ulam model with long-range interactions*”, [Phys. Rev. E **95**, 032102 \(2017\)](#).
- [80] N. Freitas, E. A. Martinez, and J. P. Paz, “*Heat transport through ion crystals*”, [Physica Scripta **91**, 013007 \(2015\)](#).

- [81] A. Ruiz, D. Alonso, M. B. Plenio, and A. del Campo, “*Tuning heat transport in trapped-ion chains across a structural phase transition*”, [Phys. Rev. B **89**, 214305 \(2014\)](#).
- [82] A. Ruiz-García, J. J. Fernández, and D. Alonso, “*Delocalization and heat transport in multidimensional trapped ion systems*”, [Phys. Rev. E **99**, 062105 \(2019\)](#).
- [83] T. Pruttivarasin, M. Ramm, I. Talukdar, A. Kreuter, and H. Häffner, “*Trapped ions in optical lattices for probing oscillator chain models*”, [New Journal of Physics **13**, 075012 \(2011\)](#).
- [84] M. Ramm, T. Pruttivarasin, and H. Häffner, “*Energy transport in trapped ion chains*”, [New Journal of Physics **16**, 063062 \(2014\)](#).
- [85] J. I. Cirac and P. Zoller, “*A scalable quantum computer with ions in an array of microtraps*”, [Nature **404**, 579–581 \(2000\)](#).
- [86] F. N. Krauth, J. Alonso, and J. P. Home, “*Optimal electrode geometries for 2-dimensional ion arrays with bi-layer ion traps*”, [Journal of Physics B: Atomic, Molecular and Optical Physics **48**, 015001 \(2014\)](#).
- [87] R. Schmied, J. H. Wesenberg, and D. Leibfried, “*Optimal Surface-Electrode Trap Lattices for Quantum Simulation with Trapped Ions*”, [Phys. Rev. Lett. **102**, 233002 \(2009\)](#).
- [88] A. Dhar, “*Heat transport in low-dimensional systems*”, [Advances in Physics **57**, 457-537 \(2008\)](#).
- [89] R. Toral and P. Colet, *Stochastic numerical methods: an introduction for students and scientists*. John Wiley & Sons, 2014. <https://onlinelibrary.wiley.com/doi/abs/10.1002/9783527683147.ch6>.
- [90] C. Cohen-Tannoudji, “*Atomic motion in laser light*”, in *Fundamental systems in quantum optics*, J. Dalibard, J. M. Raimond, and J. Zinn-Justin, eds. Elsevier, 1992.
- [91] H. J. Metcalf and P. van der Straten, “*Laser cooling and trapping of atoms*”, [J. Opt. Soc. Am. B **20**, 887–908 \(2003\)](#).
- [92] L. Chee Kong, “*Study of Classical and Quantum Open Systems*”, [arXiv:1008.0491](#).

- [93] E. A. Novikov, “*Functionals and the random-force method in turbulence theory*”, Soviet Journal of Experimental and Theoretical Physics **20**, 1290-1294 (1965).
- [94] P.-W. Ma and S. L. Dudarev, “*Langevin spin dynamics*”, Phys. Rev. B **83**, 134418 (2011).
- [95] G. D. Chiara, G. Landi, A. Hewgill, B. Reid, A. Ferraro, A. J. Roncaglia, and M. Antezza, “*Reconciliation of quantum local master equations with thermodynamics*”, New Journal of Physics **20**, 113024 (2018).
- [96] A. Levy and R. Kosloff, “*The local approach to quantum transport may violate the second law of thermodynamics*”, EPL (Europhysics Letters) **107**, 20004 (2014).
- [97] S. Särkkä and A. Solin, *Applied Stochastic Differential Equations*. Institute of Mathematical Statistics Textbooks. Cambridge University Press, 2019.
- [98] D. F. V. James, “*Quantum dynamics of cold trapped ions with application to quantum computation*”, Applied Physics B **66**, 181–190 (1998).
- [99] J. Bezanson, S. Karpinski, V. B. Shah, and A. Edelman, “*Julia: A Fast Dynamic Language for Technical Computing*”, arXiv:1209.5145.
- [100] J. Bezanson, A. Edelman, S. Karpinski, and V. Shah, “*Julia: A Fresh Approach to Numerical Computing*”, SIAM Review **59**, 65-98 (2017).
- [101] C. Rackauckas and Q. Nie, “*Adaptive methods for stochastic differential equations via natural embeddings and rejection sampling with memory*”, Discrete and Continuous Dynamical Systems Series B **22**, 2731-2761 (2017).
- [102] F. M. Leupold, *Bang-bang Control of a Trapped-Ion Oscillator*. PhD thesis, ETH Zurich, 2015. <https://doi.org/10.3929/ethz-a-010616440>.
- [103] H.-Y. Lo, *Creation of Squeezed Schrödinger’s Cat States in a Mixed-Species Ion Trap*. PhD thesis, ETH Zurich, 2015. <https://doi.org/10.3929/ethz-a-010592649>.
- [104] T. Zhang and T. Luo, “*Giant Thermal Rectification from Polyethylene Nanofiber Thermal Diodes*”, Small **11**, 4657-4665 (2015).

- [105] M. Enderlein, T. Huber, C. Schneider, and T. Schaetz, “*Single Ions Trapped in a One-Dimensional Optical Lattice*”, [Phys. Rev. Lett. **109**, 233004 \(2012\)](#).
- [106] A. Bermudez, M. Bruderer, and M. B. Plenio, “*Controlling and Measuring Quantum Transport of Heat in Trapped-Ion Crystals*”, [Phys. Rev. Lett. **111**, 040601 \(2013\)](#).
- [107] C. Schneider, M. Enderlein, T. Huber, and T. Schaetz, “*Optical trapping of an ion*”, [Nature Photonics **4**, 772–775 \(2010\)](#).
- [108] A. Riera-Campenya, M. Mehboudi, M. Pons, and A. Sanpera, “*Dynamically induced heat rectification in quantum systems*”, [Phys. Rev. E **99**, 032126 \(2019\)](#).
- [109] H. Ma and Z. Tian, “*Significantly High Thermal Rectification in an Asymmetric Polymer Molecule Driven by Diffusive versus Ballistic Transport*”, [Nano Letters **18**, 43–48 \(2018\)](#).
- [110] K. M. Reid, H. D. Pandey, and D. M. Leitner, “*Elastic and Inelastic Contributions to Thermal Transport between Chemical Groups and Thermal Rectification in Molecules*”, [The Journal of Physical Chemistry C **123**, 6256-6264 \(2019\)](#).
- [111] T. J. Alexander, “*High-heat-flux rectification due to a localized thermal diode*”, [Phys. Rev. E **101**, 062122 \(2020\)](#).
- [112] Z. Rieder, J. L. Lebowitz, and E. Lieb, “*Properties of a Harmonic Crystal in a Stationary Nonequilibrium State*”, [Journal of Mathematical Physics **8**, 1073-1078 \(1967\)](#).
- [113] A. Casher and J. L. Lebowitz, “*Heat Flow in Regular and Disordered Harmonic Chains*”, [Journal of Mathematical Physics **12**, 1701-1711 \(1971\)](#), <https://doi.org/10.1063/1.1665794>.
- [114] M. A. Simón, S. Martínez-Garaot, M. Pons, and J. G. Muga, “*Asymmetric heat transport in ion crystals*”, [Phys. Rev. E **100**, 032109 \(2019\)](#).
- [115] D. Leibfried, R. Blatt, C. Monroe, and D. Wineland, “*Quantum dynamics of single trapped ions*”, [Rev. Mod. Phys. **75**, 281–324 \(2003\)](#).

- [116] S. Chu, L. Hollberg, J. E. Bjorkholm, A. Cable, and A. Ashkin,
“*Three-dimensional viscous confinement and cooling of atoms by resonance radiation pressure*”, [Phys. Rev. Lett. **55**, 48–51 \(1985\)](#).
- [117] H. Metcalf and P. Van der Straten, *Laser Cooling and Trapping*. Graduate texts in contemporary physics. Springer-Verlag, New York, 1999.